UNIVERSITÀ DI PADOVA

Facoltà di Scienze Matematiche Fisiche e Naturali
Dipartimento di Fisica *Galileo Galilei*

Scuola di Dottorato di Ricerca in Fisica
Ciclo XXII

Underground study of ^{15}N(p,γ)^{16}O at stellar energies

Direttore della scuola: Ch.mo Prof. Attilio Stella

Supervisore: Dott. Carlo Broggini

Co-supervisore: Ch.mo Prof. Antonio Masiero

Dottorando:
Antonio Caciolli

Ai miei nonni

Contents

Introduzione i

Introduction iii

1 Hydrogen burning in stars 1

- 1.1 The life of the stars . . . 1
- 1.2 Qualitative features of the nuclear reaction mechanisms . . . 4
  - 1.2.1 Charged-particle-induced non resonant reactions . . . 6
  - 1.2.2 Direct capture reactions . . . 9
  - 1.2.3 Reaction through isolated resonances . . . 10
- 1.3 The ^{15}N(p,γ)^{16}O reaction . . . 13

2 The LUNA facility 15

- 2.1 Underground measurements . . . 15
- 2.2 The LUNA2 accelerator . . . 17
- 2.3 The beam lines . . . 19
  - 2.3.1 The gas target channel . . . 20
  - 2.3.2 The solid target channel . . . 22
- 2.4 The 4π BGO detector and the electronics . . . 24

3 ^{15}N(p,γ)^{16}O cross section from the gas target experiment 29

- 3.1 Isotopic composition of ^{15}N in various materials . . . 29
- 3.2 Target density and beam heating . . . 31
- 3.3 Localization of contaminants . . . 32
- 3.4 Detector efficiency . . . 34
  - 3.4.1 Detector description . . . 34
  - 3.4.2 Validation using radioactive sources, without target chamber . . . 34
  - 3.4.3 Validation using radioactive sources, with gas target chamber . . . 35
  - 3.4.4 Comparison with previous GEANT3 simulations . . . 37
  - 3.4.5 Angular distribution and cascade transitions . . . 38
- 3.5 Spectra analysis . . . 39
  - 3.5.1 Spectra analysis and ^{11}B background subtraction . . . 42
- 3.6 Experimental upper limits on possible cascade transitions . . . 45

3.6.1 Runs with an HPGe detector and the present gas target setup 46
3.6.2 Runs using a Clover germanium detector and solid targets 47
3.7 Localization of the ^{11}B contaminant and the GEANT4 simulation code 48
3.8 Data Analysis 52
3.9 Astrophysical S-factors 53

4 ^{15}N(p,γ)^{16}O cross section from the solid target experiment **57**
4.1 Data taking 57
4.2 Target production and analysis 62
4.2.1 Sputtering process for solid target production 64
4.2.2 LUNA target monitor measurements 66
4.2.3 Dresden measurements 70
4.3 High Z Elastic Recoil Detection 75
4.4 Target Analysis 77
4.5 The 4π-BGO detector efficiency 80
4.5.1 Radioactive sources measurements and efficiency stability 80
4.5.2 High energy efficiency 84
4.6 Analysis and S-factor evaluation 88

5 Conclusions **93**

A Background characterization of the ultra-sensitive in-beam γ-ray spectroscopy facility at LUNA **97**
A.1 Experimental setup 98
A.2 Laboratory γ-ray background studies for E_γ <3 MeV 100
A.3 γ-ray background induced by the α-beam 103
A.4 Feasibility of cross-section measurements at LUNA 104

B Target measurements excluded from the target analysis **109**
B.1 Nuclear reaction induced by deuteron on nitrogen 109
B.2 Secondary Neutral Mass Spectrometry 112

C Laboratory background measurements at different sites **115**
C.1 Detector 115
C.2 The Monte Soratte Bunker 116
C.3 The Felsenkeller Laboratory 117
C.4 Comparison 117

List of figures **124**

List of tables **131**

Ringraziamenti **135**

Introduzione

Sin dall'antichità, l'uomo si è chiesto quale fosse il ruolo delle stelle nell'universo e nella sua vita. Adesso sappiamo che le stelle sono le fucine dove vengono prodotti gli elementi che costituiscono l'universo e, di conseguenza, anche il nostro corpo. Per questa ragione ci possiamo considerare polvere di stelle.

Da quando Eddington formulò la sua ipotesi, secondo la quale l'energia che alimenta il sole e le altre stelle viene fornita dalle reazioni termonucleari che trasformano gli elementi leggeri in quelli via via più pesanti, gli scienziati si sono prodigati a lungo per comprendere i dettagli delle reazioni nucleari all'interno dei corpi celesti. Tutti gli elementi della tavola periodica (con l'eccezione di idrogeno, elio e litio che sono prodotti durante la Nucleosintesi del Big Bang) sono generati all'interno delle stelle. Fino ad ora sono state formulate molte teorie supportate dai risultati sperimentali, ma rimangono ancora diversi quesiti irrisolti.

Vari modelli sono stati sviluppati per descrivere i sistemi stellari. In particolare, negli ultimi anni, grazie alla potenza di calcolo dei computer di nuova generazione, i modelli riescono a descrivere la struttura e lo sviluppo delle stelle anche in tre dimensioni. In questo modo si riesce a studiare in maniera sempre più approfondita la struttura interna dei corpi celesti. Un input fondamentale per questi modelli è la sezione d'urto delle reazioni nucleari. La conoscenza della sezione d'urto all'energia propria delle stelle rappresenta il cuore dell'astrofisica nucleare. A queste energie le reazioni nucleari sono fortemente soppresse dalla repulsione Coulombiana dei nuclei interagenti e la sezione d'urto è molto piccola. È possibile misurare queste reazioni nucleari in laboratorio, ma solo ad energie più elevate di quelle di interesse astrofisico. Infatti la sezione d'urto estremamente piccola si traduce in un rateo di eventi molto basso e non separabile dal fondo ambiente. Le sezioni d'urto così ottenute devono essere estrapolate alle energie proprie delle stelle introducendo una notevole incertezza.

Negli ultimi anni sono stati fatti considerevoli sforzi in modo da misurare la sezione d'urto ad energie sempre più vicine a quelle di interesse astrofisico. In particolare, LUNA (Laboratory for Underground Nuclear Astrophysics), grazie alla sua posizione privilegiata all'interno dei Laboratori Nazionali del Gran Sasso (LNGS), sfrutta la soppressione dei raggi cosmici e può quindi studiare le reazioni nucleari alle basse energie non esplorabili negli esperimenti di superficie. La schermatura naturale di 1.4 km di roccia fornita dal Gran Sasso ha reso possibile, ad esempio, lo studio della reazione ^{3}He(^{3}He,2p)^{4}He, una delle più importanti reazioni della catena protone-protone, alle energie alle quali avviene nel sole. ^{14}N(p,γ)^{15}O, la reazione chiave del ciclo carbonio azoto ossigeno (CNO), è stata anch'essa studiata da LUNA ottenendo una sezione d'urto minore di un fattore due rispetto alle precedenti estrapolazioni. L'altra importante reazione del ciclo è ^{15}N(p,γ)^{16}O che collega il primo con il secondo ciclo CNO.

In questo lavoro di tesi presenterò lo studio di questa reazione, svolto utilizzando due differenti tipologie di setup: con bersaglio gassoso e con bersaglio solido, rispettivamente. Il primo capitolo è una breve descrizione delle principali caratteristiche delle reazioni termonucleari nelle stelle. Nel secondo capitolo verrà presentato l'acceleratore LUNA2 insieme ai due canali di misura utilizzati e verranno descritte le caratteristiche del rivelatore BGO. Infine, il terzo e il quarto capitolo vertono sulla misura della reazione ^{15}N(p,γ)^{16}O. Nello specifico il capitolo tre è dedicato all'analisi delle misure eseguite con il bersaglio gassoso ed ai risultati sperimentali ottenuti con questo setup. Nel capitolo quattro, invece, vengono presentati i risultati delle misure eseguite con bersaglio solido soffermandosi in particolare sulle metodologie di analisi dei bersagli utilizzati.

In sintesi, la sezione d'urto della reazione ^{15}N(p,γ)^{16}O è stata misurata per la prima volta sino all'energia di 70 keV nel centro di massa. Il risultato ottenuto riduce di un fattore due la precedente estrapolazione delle misure dirette riportata nel database NACRE (Nuclear Astrophysics Compilation of REaction Rates). Alla fine, verranno discusse le implicazioni di questi nuovi risultati per la sintesi degli elementi nelle esplosioni di novae.

Introduction

Since the ancient times, mankind has been wondering about the role of stars, both in the sky at night and in his life. Actually we know that stars are the forges of the elements which constitute our universe and of course ourselves. As a matter of fact, we are made of stardust. Since the Eddington hypothesis that the energy which powers the sun and other stars comes from thermonuclear reactions, the scientists have done a lot of work to understand the mechanisms of nuclear reactions inside stars. All the elements of the periodic table (except hydrogen, helium and lithium which are synthesized during the Big Bang Nucleosynthesis) are produced inside the stars. Many theories were formulated and supported by experimental measurements, however there are still many questions to be answered.

Many models have been developed in order to describe stellar systems. In recent years, due to the resources provided by the new high performance computers, the models can describe the stellar behavior also in three dimensions extending our knowledge of the stellar interior. One critical input of these models is the cross section of the nuclear reactions. The knowledge of the cross section at the stellar energies lies at the heart of nuclear astrophysics. At these energies nuclear reactions are strongly suppressed by the Coulomb repulsion of the colliding nuclei and the cross section is extremely small. As a matter of fact, the reaction rates are too low to be measured due to the overwhelming experimental background. In overground laboratories the nuclear reactions can be measured at higher energies than those inside the stars, and then extrapolated to stellar energies. To reduce the uncertainties on the extrapolation procedure considerable efforts have been spent in recent years to push the cross section measurements to lower and lower energies.

LUNA (Laboratory of Underground Nuclear Astrophysics), thanks to its unique position in the Laboratori Nazionali del Gran Sasso (LNGS), can study nuclear reactions at energies much lower than ever reached before. Thanks to the natural shielding of the 1.4 km of rock offered by Gran Sasso, it has been possible, in particular, to directly determine the rate of ^{3}He(^{3}He,2p)^{4}He, one of the most important reaction of the p-p chain, at the energies of the center of the sun. ^{14}N(p,γ)^{15}O, the key reaction of the CNO cycle, has also been studied in great details obtaining a cross section smaller by a factor two as compared to previous extrapolations. The other important reaction of the cycle is ^{15}N(p,γ)^{16}O which links the first to second CNO cycle. In this thesis I will discuss the study of ^{15}N(p,γ)^{16}O performed with a gas target and a solid target setup in two different experiments. The first chapter is a brief description of the general characteristics of thermonuclear reactions in the stars. In the second chapter the LUNA2 accelerator will be reviewed and the two beam channels, dedicated to the gas target and solid target experiments, will be described. Finally, the third and the fourth chapters are devoted to the ^{15}N(p,γ)^{16}O measurements. Specifically in the third chapter the analysis of the gas target data will be discussed and the results presented. The fourth chapter is dedicated to the analysis of the solid target data, in particular to the different measurements performed to characterize the targets. We measured the cross section of ^{15}N(p,γ)^{16}O for the first time down to 70 keV obtaining values smaller by about a factor two as compared to the extrapolation in the NACRE (Nuclear Astrophysics Compilation of REaction Rates) database. Finally, the influence of our results on isotope production in nova explosions will be discussed.

Chapter 1

Hydrogen burning in stars

Nuclear reactions are the energy source that makes stars shine. The goal of nuclear astrophysics is to understand the energy generation in stars during stellar evolution and to explain the abundances of the elements and their isotopes as we observe in nature. Since all elements are produced by nuclear reactions during both the Big Bang Nucleosynthesis (BBN) and during the stellar evolution it is not surprising that these studies require as input the reaction rates for the nuclear processes.

In this chapter I will discuss thermonuclear reactions and in particular the definition of stellar reaction rate and the most significant quantities in nuclear astrophysics together with the different reaction mechanisms.

1.1 The life of the stars

When stars form starting from gas clouds in the interstellar medium, they are composed predominantly of hydrogen. They contract until the central temperature becomes sufficient to trigger hydrogen thermonuclear reactions. At this time the radiated power is equal to the one due to the nuclear reactions in the star interiors. The conversion of hydrogen to helium changes the central composition continuously to finally have a hydrogen-exhausted core. During this time, the stellar luminosity and radius both increase. The stars in this phase constitute the main sequence of the Herzsprung-Russel diagram, that represent the star's luminosity ($L = \frac{dE}{dt}$) in unity $L_\odot$ (Sun luminosity), as function of the surface temperature (Fig. 1.1). In stars the luminosity is correlated to the mass. Generally it is found that most massive stars of the main sequence are also the most luminous ($L \approx M^{3-4}$). The mass of the star is thus one of the basic characteristics determining its evolution. For example a star with $M/M_\odot = 10$ initially has a much larger reservoir of nuclear fuel than the Sun, but it burns this fuel more than 1000 time faster, resulting in a much shorter life and a much quicker run trough the evolutionary stages.

The hydrogen burning is for sure the main processes for energy production in stars and it could be summarized as the production of an helium from four protons:

$$4\text{p} \longrightarrow^4 \text{He} + 2\text{e}^+ + 2\nu + 26.73\text{MeV} \tag{1.1}$$

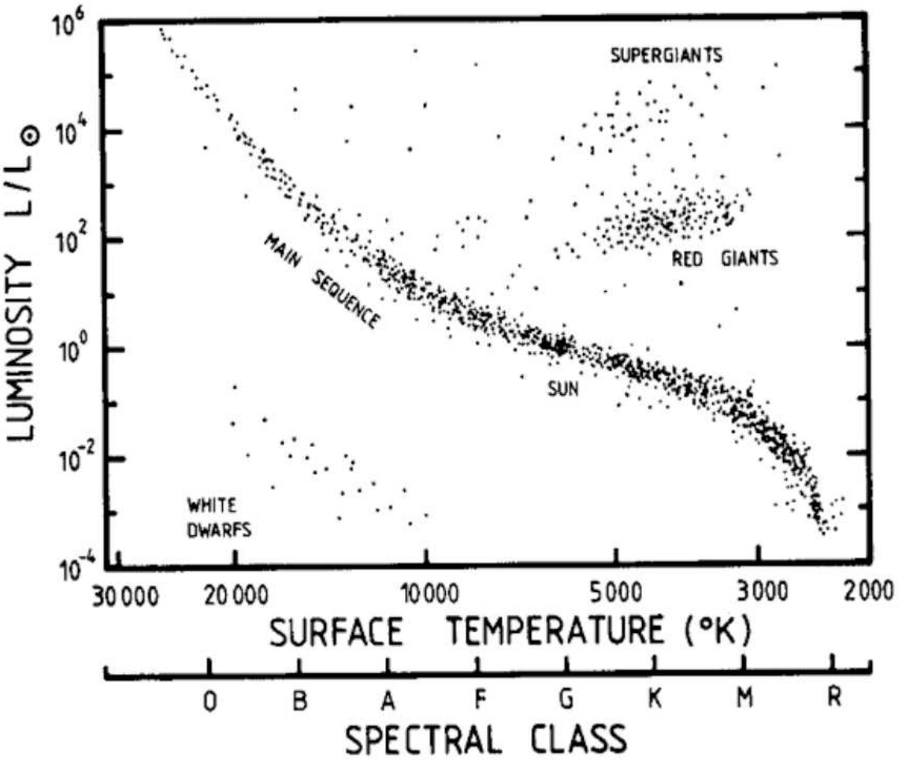

Figure 1.1: *Hertzsprung-Russel diagram. Most of the stars, including the Sun, are aligned along the main sequence.* $L_\odot$ *is the luminosity of the Sun.*

Fig.1.2 and Fig.1.3 show the two main processes of hydrogen burning: the p-p chain and the CNO cycle, respectively. The sequence of reaction for the p-p chain starts mainly with the proton-proton reaction: $p(p, e^+\nu)d$. It is the slowest reaction, and therefore represents the bottleneck of the rate of the whole chain. The cross section for this reaction is too small to be measured in a laboratory today, so it is calculated from standard weak-interaction theory to be of the order of 10^{-33} barn at keV energies and 10^{-23} barn at MeV energies (1barn = 10^{-24} cm^2). When the center of the star reaches a temperature of $T \approx 6 \cdot 10^6$ K hydrogen burning switched on, the reaction ^{3}He + ^{3}He finally produces a ^{4}He nucleus and two protons (chain I):

$$^3\text{He} + {}^3\text{He} \longrightarrow {}^4\text{He} + \text{p} + \text{p} \tag{1.2}$$

An alternative is to encounter an α particle

$$^3\text{He} + {}^4\text{He} \longrightarrow {}^7\text{Be} + \gamma \tag{1.3}$$

The ^{7}Be is unstable and decays via electron capture to ^{7}Li with the emission of a 0.86 MeV neutrino or, with a 10% branching ratio, to the excited state of ^{7}Li with the emission of a 0.38 MeV neutrino. The ^{7}Li captures a proton producing ^{8}Be, which decays immediately ($\tau \approx 10^{-16}$ s) into two helium nuclei (chain II). The ^{7}Be electron capture competes with proton

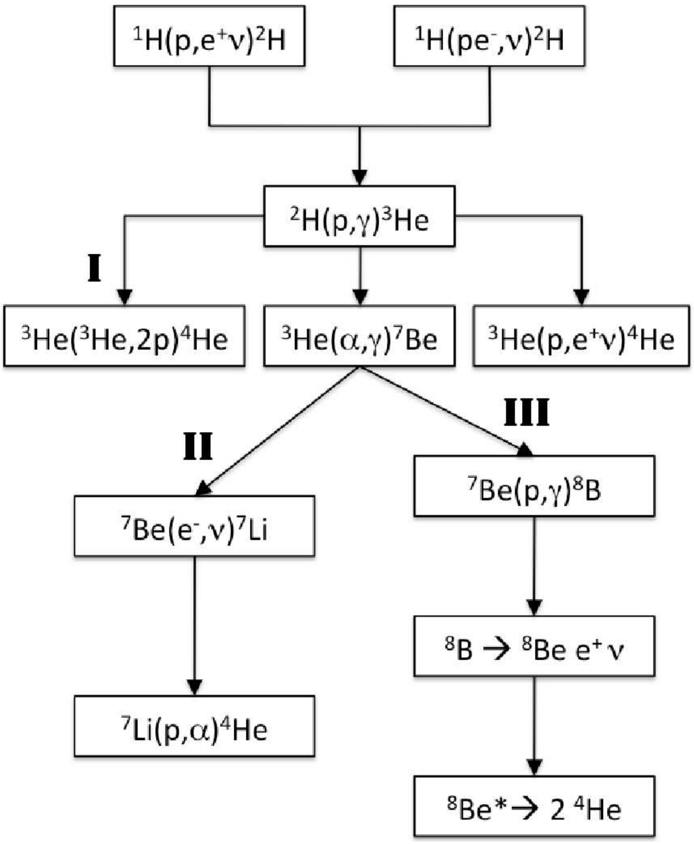

Figure 1.2: *The proton-proton chain for hydrogen burning in the Sun.*

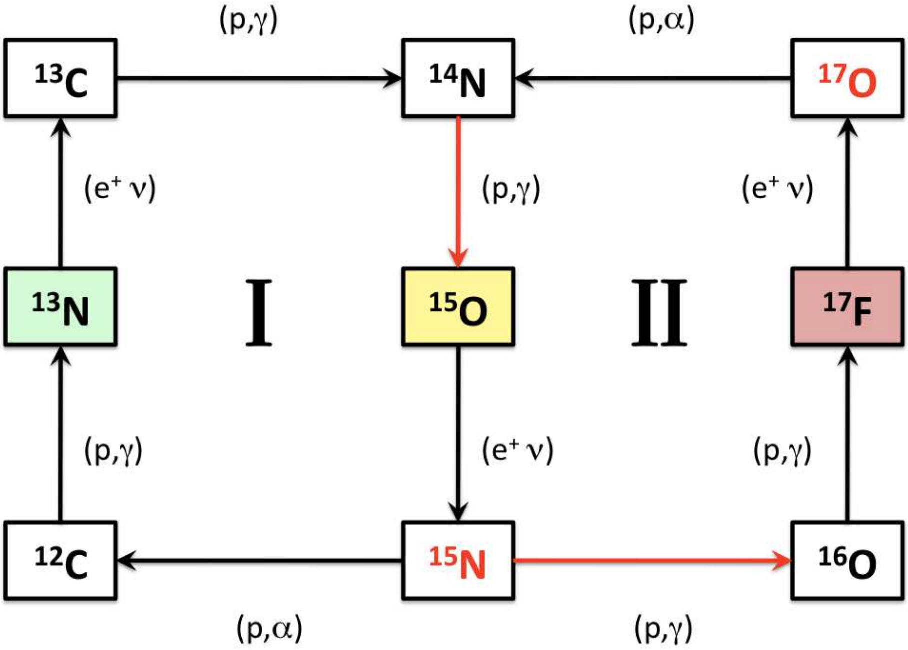

Figure 1.3: *The first and second CNO cycles.*

capture to ^{8}B, which decays to ^{8}Be ($\tau \approx 1$ s) producing a positron, a high energy neutrino (0 MeV $\leq E_\nu \leq 15$ MeV) and again two helium nuclei. The complete processes are indicated schematically in Fig.1.2. Since, however, the energy lost via neutrino emission depends on the specific chain, we must consider three different effective Q-values , corresponding to the 3 chains:

- p-p-I → Q_{eff} = 26.2 MeV
- p-p-II → Q_{eff} = 25.66 MeV
- p-p-III → Q_{eff} = 19.17 MeV

In 1938 and 1939 von Weizsäcker and Bethe investigated for the first time a new mechanisms of hydrogen burning in stars containing small amounts of heavier elements: the CNO cycle (Fig. 1.3). The nuclei C, N and O participate in hydrogen burning as catalysts. Each CN and NO chain is formed by four reaction and two β^+ decay. The resulting cycle through which hydrogen can be converted to helium are referred to as the CNO cycles and are shown in Fig. 1.3. The final result of the cycle is the same as for the p-p chain. In each cycle, C, N, O nuclei act only as catalysts, in the sense that the total abundance of the heavy nuclei is not changed at the equilibrium, while only hydrogen is consumed. Therefore, a substantial amount of nuclear energy can be generated even if the total abundance of the heavy nuclei is relatively low. The various CNO cycles exist because of the proton induced reactions on the nuclei ^{15}N, ^{17}O, ^{18}O and ^{19}F.

The CNO cycle has been studied by the LUNA collaboration. In particularly the ^{14}N(p,γ)^{15}O reaction has been studied in great details [1, 2, 3, 4, 5]. This reaction is the slowest of the entire cycle and as a consequence it controls the speed of the cycle itself. The ^{14}N(p,γ)^{15}O reaction is directly related to the neutrinos production by the β^+ decay of ^{13}N and ^{15}O nuclei. LUNA has studied with three different experiments this reaction down to 70 keV center of mass energy obtaining a cross section value lower by a factor two as compared to the previous extrapolation. As a consequence, the CNO neutrino flux from the Sun has been decreased by a factor two.

1.2 Qualitative features of the nuclear reaction mechanisms

Nuclear reactions in the early universe as well as nuclear reactions in stars are among the most important driving forces for the evolution of our universe. In a reaction between two nuclides, which is the predominantly type of reactions in astrophysical processes, 1 + 2 → 3 + 4, the Q-value of the reaction is given by the energy conservation:

$$Q = (M_1 + M_2 - M_3 - M_4)c^2 \tag{1.4}$$

where M_i represent the mass of the particle i. If the Q-value is positive then the reaction is exothermic and there is a net production of energy in the reaction. Differently, if the Q-value is negative the reaction needs energy to proceed and it is called endothermic. Exothermic reactions are the most important fusion processes in stars.

The stellar reaction rate is proportional to the cross section of the specific reaction we are studying (1.5):

$$r_{12} = N_1 N_2 v \sigma(v) \tag{1.5}$$

Where $N_1 \equiv \mathcal{N}_t/V$ and $N_2 \equiv \mathcal{N}_b/V$ are the number densities of the interacting particles (in units of particles per volume). In stellar plasma the relative velocity of the interacting nuclei 1 and 2 is not constant, but there exists a distribution of relative velocities, described by the probability function $P(v)$. The reaction rate could be generalized for a distribution of relative velocities by writing:

$$r_{12} = N_1 N_2 \int_0^\infty v P(v) \sigma(v) dv \equiv N_1 N_2 \langle \sigma v \rangle_{12} \tag{1.6}$$

where $\langle \sigma v \rangle_{12}$ is the reaction rate per particle pair and $N_1 N_2$ is the total number density of pairs of nonidentical nuclei 1 and 2. In general, considering also the case of identical particles, the eq. (1.6) can be written as:

$$r_{12} = \frac{N_1 N_2 \langle \sigma v \rangle_{12}}{1 + \delta_{12}} \tag{1.7}$$

where δ_{12} is the Kronecker symbol.

In stellar matter the distribution of particles' velocities can be described by the Maxwell-Boltzmann distribution:

$$\Phi(v) = 4\pi v^2 \left(\frac{\mu}{2\pi kT}\right)^{\frac{3}{2}} e^{-\mu v^2/2kT} \tag{1.8}$$

where μ is the reduced mass of the interacting particles, k is the Boltzmann constant and T is the local temperature. Substituting the expression (1.8) in $\langle \sigma v \rangle_{12}$ we obtain the reaction rate per particle pair:

$$\langle \sigma v \rangle_{12} = 4\pi \left(\frac{\mu}{2\pi kT}\right)^{\frac{3}{2}} \int_0^\infty v^3 \sigma(v) e^{-\mu v^2/2kT} dv \tag{1.9}$$

Using the center of mass energy $E = \frac{1}{2}\mu v^2$, the equation (1.10) finally can be written in the form:

$$\langle \sigma v \rangle_{12} = \left(\frac{8}{\pi\mu}\right)^{\frac{1}{2}} \frac{1}{(kT)^{3/2}} \int_0^\infty \sigma(E) E e^{-\frac{E}{kT}} dE \tag{1.10}$$

It is important to underline that most of the critical stellar features, such as time scales, energy production and nucleosynthesis of the elements, are directly connected to the magnitude of the reaction rate per particle pair given by eq. (1.10). The reaction rate changes as a consequence of the stellar evolution and in particularly of the temperature changing into the stars. The cross section $\sigma(E)$ turns out to be a critical parameter to understand stellar evolution processes. The stellar evolution spreads over an extended range of temperature, from the Main Sequence stars ($T \approx 10^7$) to supernovae ($T \approx 10^9$). As a consequence it is necessary to know the cross section, $\sigma(E)$, over a corresponding wide range of energies from keV to MeV.

1.2.1 Charged-particle-induced non resonant reactions

The nuclei into the stellar plasma are totally ionized and they repel each other with a force proportional to the nuclear electric charge. The repulsive potential can be written in this form:

$$V_c = \frac{Z_1 Z_2 e^2}{r} = 1.44 \frac{Z_1 Z_2}{r\ [\mathrm{fm}]}\ \mathrm{MeV} \tag{1.11}$$

where Z_1 and Z_2 are the electric charges of the interacting nuclei and r is their distance. The nuclear potential starts to play a role at distances comparable with the nuclear radius $R_n = R_1 + R_2$ (sum of the nuclear radii of the two interacting nuclei). The combination of the two potential leads to an effective potential shown in Fig. 1.4. The fusion can thus occur only if the Coulomb barrier is overcome. In quantum mechanics there is a small probability for the particles with an energy $E < E_c$ to penetrate the Coulomb barrier. This phenomenon is called tunnel effect and it is of key importance in stellar burning.

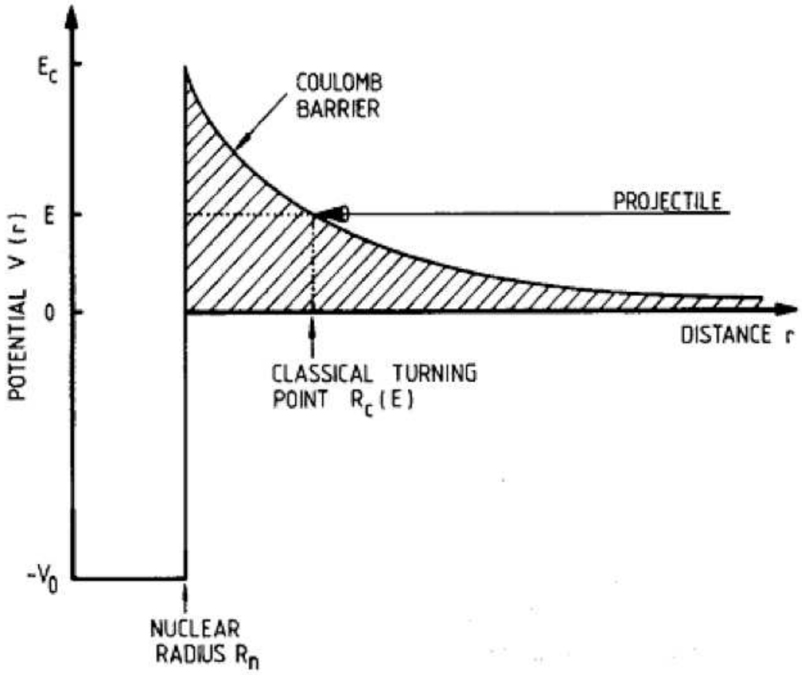

Figure 1.4: *Schematic representation of the combined nuclear and Coulomb potentials.*

The square of the wave function, $|\psi(r)|^2$, in quantum mechanics gives the probability of finding the particles at the position r. The probability to find the particle at the turning point of the Coulomb barrier is $|\psi(R_c)|^2$ and the one at the nuclear radius is $|\psi(R_n)|^2$. Then we can calculate the probability that incoming particles penetrate the barrier as:

$$P = \frac{|\psi(R_n)|^2}{|\psi(R_c)|^2} \tag{1.12}$$

The analytical expression of the (1.12) is obtained solving the Schrödinger equation for the Coulomb potential. Decreasing the energies in a region where $E \ll E_c$ the equation can be approximated by the following expression [6]:

$$P = e^{-2\pi\eta} \tag{1.13}$$

where η is the Sommerfield parameter defined as

$$\eta = \frac{Z_1 Z_2 e^2}{\hbar v} \tag{1.14}$$

where Z_1 and Z_2 are the atomic number of the two nuclei involved into the reaction, $\hbar$ the Planck's constant divided by 2π and e the electron charge. In numerical units the exponent is:

$$2\pi\eta = 31.29 Z_1 Z_2 \left(\frac{\mu}{E}\right)^{1/2} \tag{1.15}$$

where the center of mass energy E is given in units of keV and the μ is in amu. The expression $e^{-2\pi\eta}$ is commonly referred to as Gamow factor and it is referred to the penetration probability. The cross section is directly proportional to this:

$$\sigma(E) \propto e^{-2\pi\eta} \tag{1.16}$$

Classically, the cross section is equal to the combined geometrical area of the projectile and the target nucleus and it can be written as $\sigma = \pi(R_1 + R_2)^2$. In quantum mechanics the geometrical cross section must be replaced by the energy-dependent quantity $\sigma = \pi\lambda^2$, where λ[1] represents the de Broglie wavelength reflecting the wave aspect of quantum mechanical processes:

$$\sigma(E) \propto \pi\lambda^2 \propto \frac{1}{E} \tag{1.17}$$

Combining both expressions for the cross section one can write:

$$\sigma(E) = \frac{1}{E}\exp(-2\pi\eta(E))S(E) \tag{1.18}$$

The term $S(E)$ in eq. (1.18) is called S-factor and contains all the strictly nuclear effects. The following approximations have been done to find the (1.18):

1. a square-well potential inside the nuclear radius and a Coulomb potential of a point source outside
2. the height of the Coulomb barrier is much larger than the projectile energy
3. no centrifugal barrier in the entrance channel: only s-wave projectiles.

---

[1] The simbol λ used for the definition of the de Broglie wavelength is not correct: usually it is defined by the symbol "λ slash = $\frac{\lambda}{2\pi}$" that is not supported by LaTeXpackage. The reader should take into account this notation variation in the whole thesis.

Then, from (1.19) we can write:

$$\eta(E) = \frac{Z_1 Z_2 e^2}{\hbar} (\mu/2E)^{1/2} \tag{1.19}$$

Substituting the cross section from eq. (1.18) in eq. (1.10) we have:

$$\langle \sigma v \rangle_{12} = \left(\frac{8}{\pi \mu} \right)^{\frac{1}{2}} \frac{1}{(kT)^{3/2}} \int_0^\infty S(E) \exp\left(-\frac{E}{kT} - \frac{b}{E^{1/2}} \right) dE \tag{1.20}$$

where b is given by:

$$b = (2\mu)^{1/2} \pi e^2 Z_1 Z_2 / \hbar = 0.989 Z_1 Z_2 \mu^{1/2} \tag{1.21}$$

For non-resonant reactions $S(E)$ varies smoothly with energy, so the energy dependence of the integrand of eq. (1.20) is governed primarily by the exponential term. This term shows a maximum at an energy

$$E_0 = \left(\frac{bkT}{2} \right)^{\frac{2}{3}} = 1.22 (Z_1^2 Z_2^2 \mu T)^{\frac{1}{3}} \tag{1.22}$$

For a given stellar temperature T, nuclear reactions take place in a relatively narrow window around the effective burning energy of E_0 (Fig. 1.5). Increasing nuclear charge of the reactive particles, E_0 moves toward higher energies: the rate of nuclear reactions depends with the increasing of the barrier The exponential term in the eq. (1.20) can be approximated by a Gaussian function:

$$\exp\left(-\frac{E}{kT} - \frac{\sqrt{E}_G}{E^{\frac{1}{2}}} \right) = \exp\left(-\frac{3E_0}{kT} \right) \exp\left[-\left(\frac{E - E_0}{\Delta/2} \right)^2 \right] \tag{1.23}$$

with Δ = $0.749 (Z_1^2 Z_2^2 \mu T^5)^{1/6}$ keV. Nuclear burning reactions take places predominantly in the energy window $E = E_0 \pm \Delta/2$. At stellar temperatures this band is often at too low energies for direct measurements of the cross section $\sigma(E)$. One possible technique in order to solve this problem is to measure $S(E)$ in at higher energies and then to extrapolate the data downward to E_0.

The nuclei with the smallest Coulomb barrier are consumed at first in stars and they account for the most of the nuclear energy generation. When those nuclei are consumed the stars will contract gravitationally until the temperature rises to a point where nuclei with next lowest Coulomb barrier can burn. In Fig. 1.5 the Gamow peak is shown for three different ^{15}N(p,γ)^{16}O stellar scenarios is shown together with the cross section and the Maxwell-Boltmann distribution. As shown in the figure the LUNA dynamic energy range covers the Gamow peak in the most important scenarios. The resonance at E_R = 312 keV strongly affects the Gamow peak. In this way it is important to verified the data in literature. In the case of non-resonant reaction the S-factor could be approximated as constant over the Gamow peak and we can write the reaction rate as:

$$\langle \sigma v \rangle_{12} = \left(\frac{2}{\mu} \right)^{\frac{1}{2}} \frac{\Delta}{(kT)^{3/2}} S(E_0) \exp\left(-\frac{3E_0}{kT} \right) \tag{1.24}$$

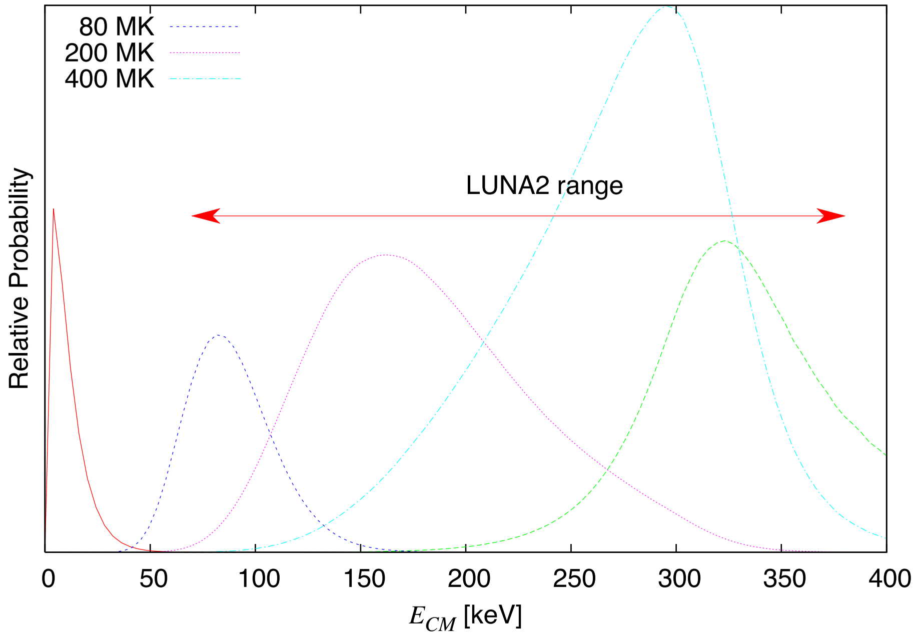

Figure 1.5: *The Gamow peak for the ^{15}N(p,γ)^{16}O reaction at three different temperatures. The Maxwell-Boltzmann distribution (1.8) is shown in red, the cross section (1.18) in green and their product in the three colors reported in figure. The y axis is linear, in arbitrary units. The curves are scaled to be clearly visible in the picture.*

More generally the S-factor is described by a slowly varying function of energy E and can be expanded in Taylor series:

$$S(E) = S(0) + \dot{S}(0)E + \frac{1}{2}\ddot{S}(0)E^2 + ... \tag{1.25}$$

The terms $S(0)$, $\dot{S}(0)$ and $\ddot{S}(0)$ are obtained from fits to experimental data. The fits are more reliable if we are able to measure closer to the energies of the Gamow peak.

For simplicity, the S-factor extrapolated to zero energy $S(0)$ is often quoted. This value can generally be used to get a first idea of $\langle \sigma v \rangle_{12}$. Reaction rates are then tabulated in compilations, for example the NACRE compilation [7].

1.2.2 Direct capture reactions

Direct capture is a particular type of non-resonant reaction that characterizes a lot of important nuclear processes in astrophysics. In particularly the ^{15}N(p,γ)^{16}O reaction al low energies is dominated by direct capture. In many (p,γ) reactions, the cross section shows a smooth variation with the proton energy onto which the resonances or the reaction are superimposed. This smooth "background" cross section is identified [8] as an extra nuclear channel phenomenon and has been designed as direct capture. Considering only the contribution of the proton Coulomb wave functions well outside the nuclear potential of the capturing nucleus it is possible to calculate the matrix elements for the process. This process is shown in Fig. 1.6 and it is not resonant since there is not involved the formation of any compound state. The direct capture process represent a transition for the projectile x from an initial continuum state (Coulomb distorted plane wave) to a final state (standing wave with characteristic orbital angular momentum l_f) via interaction with the electromagnetic field. The reaction selects those projectiles from the appropriate partial waves with orbital angular momenta l_i which can jump into final orbits (l_f) by the emission of γ-radiation of multipolarity L of energy $E_\gamma = E + Q - E_i$. In this case the cross section for the γ-ray emission ca be written as proportional to a single matrix element:

$$\sigma_\gamma \propto | < B|H_\gamma|A + x > |^2 \tag{1.26}$$

where the transition from the entrance channel A + x to the final compound nucleus B is mediated by the electromagnetic operator H_γ. The first-order time dependent perturbation theory can be used to determine the cross section since the electromagnetic forces are relatively weaker (comparing with the nuclear forces). An example is reported in [9].

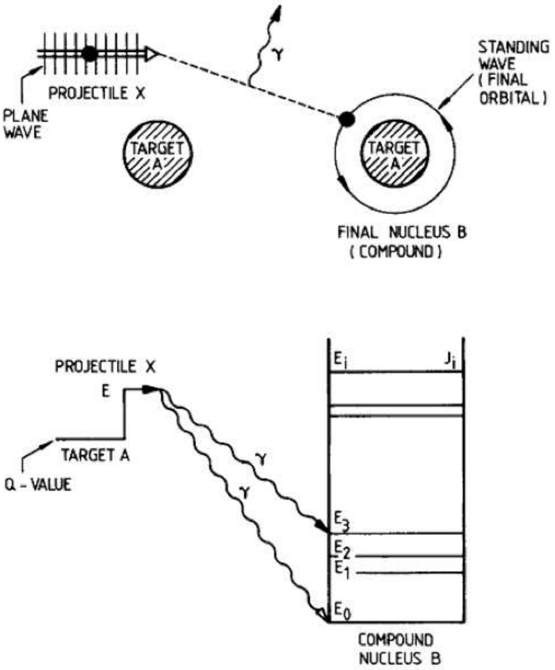

Figure 1.6: *Scheme of a generic direct capture reaction A(x,γ)B.*

1.2.3 Reaction through isolated resonances

If the reaction proceeds forming an excited state E_r that subsequently decays to lower-lying states the process is referred to as a resonant reaction. This process occurs only if the energy of the entrance channel, $Q + E_R$, matches the energy E_r of the excited state in the compound nucleus. The cross section, σ_γ, for a process where the excited state decays by emission of γ-rays to a state E_f at lower energy, is described by the product of two matrix elements:

$$\sigma_\gamma \propto |<E_f|H_\gamma|E_r>|^2|<E_r|H_f|A+p>|^2 \tag{1.27}$$

where the matrix element involving the operator H_f describes the formation of the compound state E_r. The other matrix element is referred to the subsequent γ-ray from the deexcitation of the state E_r. Each matrix element represent the probability of the process to occur and they are written by a partial width Γ_i. So we can reduce the (1.27) as:

$$\sigma_\gamma \propto \Gamma_a \Gamma_b \tag{1.28}$$

where Γ_a (Γ_b) is the partial width for the formation (decay) of the compound state. In previous section it has been said that the geometrical cross section is proportional to $\pi\lambda^2$. We can calculate this factor taking into account the momentum of the projectile ($p = \hbar k = \hbar/\lambda$) and the impact parameter and finally the value $\pi\lambda^2$ can be expressed in terms of center-of-mass energy:

$$\pi\lambda^2 = \frac{656.6}{\mu E}\,\text{barn} \tag{1.29}$$

In the case of resonant phenomena in nuclear reactions the cross section can be written as:

$$\sigma(E) = \pi\lambda^2 \frac{2J+1}{(2J_1+1)(2j_2+1)}(1+\delta_{12})\frac{\Gamma_a\Gamma_b}{(E-E_R)^2+(\Gamma/2)^2} \tag{1.30}$$

where Γ is the energy width of the excited state and $\frac{2J+1}{(2J_1+1)(2j_2+1)}(1+\delta_{12})$ is the statistical factor that takes into account the spin of the projectile (J_1), of the target nucleus (J_2) and the angular momentum of the resonant state (J). The (1.30) is the Breit-Wigner formula for a single-level resonance. This equation is valid only for isolated resonances, defined as resonances for which the separation of the nuclear levels is large compared with their total width. The resonance state can be formed via a given reaction channel if the angular momentum and parity conservation laws are respected, that means:

$$\vec{J_1} + \vec{J_2} + \vec{l} = \vec{J} \tag{1.31}$$

and

$$(-1)^l \pi^{J_1} \pi^{J_2} = \pi^J \tag{1.32}$$

where l is the relative orbital angular momentum between the target and the projectile. If the case of narrow resonance is verified ($\Gamma \ll E_R$), the Breit-Wigner cross section can be included into the stellar reaction rate per particle pair as:

$$<\sigma v>= \left(\frac{8}{\pi\mu}\right)^{1/2} \frac{1}{(kT)^{3/2}} \int_0^\infty \sigma_{BW}(E) E \exp\left(-\frac{E}{kT}\right) \mathrm{d}E \tag{1.33}$$

where σ_{BW} is the Breit-Wigner cross section reported in (1.30). In the case of narrow resonance the Maxwell-Boltzmann distribution varies very little in the energy range covered by the resonance so we can take it outside of the integral:

$$< \sigma v >= \left(\frac{8}{\pi\mu}\right)^{1/2} \frac{1}{(kT)^{3/2}} E_R \exp\left(-\frac{E_R}{kT}\right) \int_0^\infty \sigma_{BW}(E)\mathrm{d}E \tag{1.34}$$

If we can consider also λ constant over the resonance energy we can integrate σ_{BW} and we finally obtain:

$$\sigma_{BW}(E)\mathrm{d}E = 2\pi^2\lambda^2\omega\frac{\Gamma_a\Gamma_b}{\Gamma} \tag{1.35}$$

where ω is the statistical factor: $\omega = \frac{2J+1}{(2J_1+1)(2j_2+1)}(1+\delta_{12})$. The product of ω and the width ratio is referred to as the resonance strength:

$$\omega\gamma = \omega\frac{\Gamma_a\Gamma_b}{\Gamma} \; \Gamma = \Gamma_a + \Gamma_b \tag{1.36}$$

where $\Gamma = \Gamma_a + \Gamma_b$. Substituting the previous definitions into the stellar reaction rate per particles pair the (1.33) becames:

$$< \sigma v >= \left(\frac{2\pi}{\mu kT}\right)^{3/2} \hbar^2\omega\gamma \exp\left(-\frac{E_R}{kT}\right) \tag{1.37}$$

In the case of broad resonances ($\Gamma/E_R > 10\%$) the range of energies covered by the resonance is wider than in the narrow resonances case and the energy dependences in the cross section formula must be explicitly taken into account.

The low energy tail of a broad resonance is a smoothly varying function of energy and the formalism developed for non-resonant reactions (i.e. Gamow peak at energy E_0) can be applied at the low-energy wing:

$$< \sigma v >=< \sigma v >_{NR} \text{ for } E_0 \ll E_R \tag{1.38}$$

where the index NR refers to the non-resonant formalism. If there is not any interference between the resonant and non resonant mechanism the reaction rate can be written at any stellar energies as:

$$< \sigma v >=< \sigma v >_{NR} + < \sigma v >_R \tag{1.39}$$

Thanks to the much reduced background achievable in an underground laboratory direct measurements of $\sigma(E)$ for charged-particle-induced reactions can be extended to very low energies. However, only the ^{3}He(^{3}He,2p)^{4}He and d(p,γ)^{3}H could be measured at the solar Gamow peak. For the other important reactions, it is still very hard to reach relevant stellar energy region for quiescent stellar burning. The observed energy dependence of $\sigma(E)$ or equivalently of $S(E)$ must therefore be extrapolated into the stellar energy region. If there are resonances near the particles threshold, they can completely dominate the reaction rate for low stellar temperatures. It is clear that direct measurements at very low energies near the stellar energy region, are very highly requested.

1.3 The ^{15}N(p,γ)^{16}O reaction

The ^{15}N(p,γ)^{16}O reaction is an important reaction of the CNO cycles. As a matter of fact it links the first CNO cycle to the second one (see Fig.1.3) allowing for the production of the oxygen and fluorine isotopes and giving the access also to the third and fourth cycles that are responsible of the production of elements until neon. The neutrinos from the ^{17}F($\beta^+\nu$)^{17}O are produced during the second CNO cycle.

The ^{15}N can interact with proton via (p,γ) and (p,α) reactions. The Branching Ratio, or the ratio of probabilities for the occurrence of the (p,α) (strong nuclear interaction) and (p,γ) (weaker electromagnetic interaction) reaction, is given by the ratio of the corresponding reaction rates, $B_{p\alpha/p\gamma} = N_A\langle\sigma v\rangle_{(p,\alpha)}/N_A\langle\sigma v\rangle_{(p,\gamma)}$. In the case of ^{15}N(p,γ)^{16}O, the $B_{p\alpha/p\gamma}$ determines after how many cycles of CNO I the carbon will be lost as catalyst and the CNO II will proceed.

The novae have been intensively studied in recent years in relation to new methods for the tridimensional analysis of their internal mechanisms [10, 11]. In particular there are new studies [11] on the novae explosions in stars with very low metallicity. Varying the S-Factor of ^{15}N(p,γ)^{16}O by a factor two could change the amount of ^{16}O production by the 30% [12].

The astrophysical S-factor of ^{15}N(p,γ)^{16}O reaction is dominated by the resonant capture to the ground state trough the interference of the two resonances at E_R = 312 keV and E_R = 964 keV with J^π = 1^-s where E_R is the resonance energy in the center of mass. This reaction has been studied previously by Hebbard in 1960 [13] and Rolf and Rodney in 1974 [14]. Hebbard reported an S-factor extrapolated to zero energy $S(0) = 32.0 \pm 5.8$ keV barn while Rolfs and Rodney published a value of $S(0) = 64 \pm 6$ keV barn. The NACRE database uses the most recent Rolfs and Rodney value for the extrapolated S-factor. The two experimental results from direct measurements are in agreement within the high uncertainties, but there is an evident discrepancy between the two values by more than a factor two as shown in Fig. 1.7.

In 2008 new results on the S-factor, based on an indirect method, have been recently published by Mukhamedzhanov *et al.* [15]. They measured the Asymptotic Normalization Coefficients (ANC) of the reaction in order to understand the direct capture contribution. The direct capture mechanism is described in section 1.2.2 and it is related with the wave functions of the two particles involved in the reaction. At stellar energies, capture reactions proceed through the tail of the nuclear overlap function. At stellar energies, the overlapping outside the Coulomb barrier is completely determined by the Coulomb interaction. The amplitude in the exterior region must allow the overlap function to connect smoothly to the interior part of the function. The asymptotic normalization coefficient for the system A + p ↔ B specifies the amplitude of the tail of the overlap function. The amplitude of the overlapping dictates the rate of direct-capture reactions. The ANC parameters can be extracted measuring traditional nuclear reaction as peripheral nucleon transfer. In the case of the ^{15}N(p,γ)^{16}O reaction the ANC for the ground state and for seven excited states in ^{16}O were extracted from the comparison of experimental differential cross sections for the

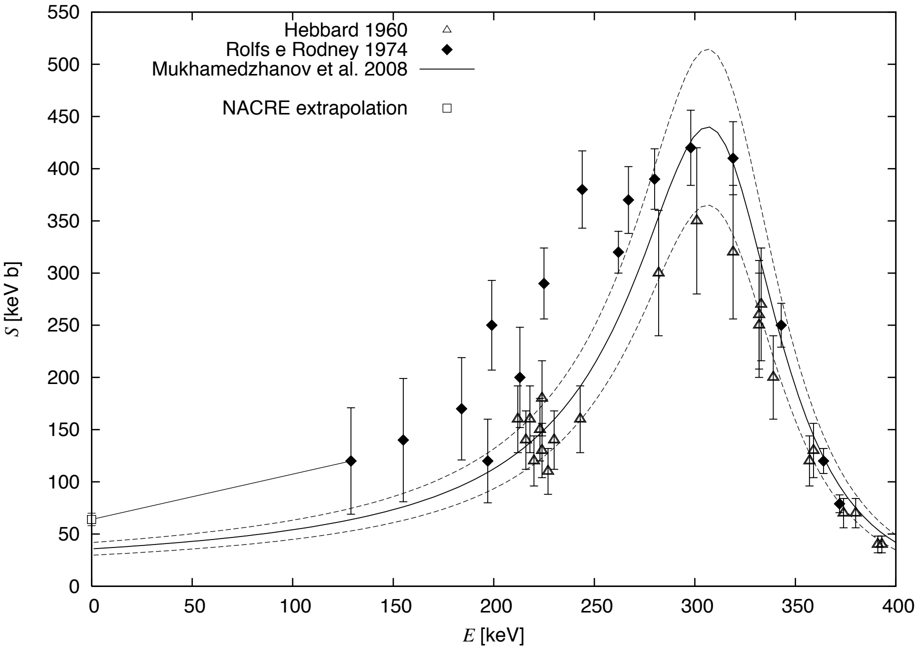

Figure 1.7: *The state of art of the measured S-factor in literature.*

^{15}N(^{3}He,d)^{16}O reaction with distorted-wave Born approximation calculations (see [15] for details). From the ANC data Mukhamedzhanov et al. extracted the direct capture component and then they performed an R-Matrix fit including the previous direct data from Rolfs and Rodney and Hebbard, together. This work reports an S-factor lower by a factor 2 than the one suggested by NACRE and in agreement with the Hebbard's extrapolated S-factor [13].

Another recent R-Matrix analysis, using again the available direct data but limited to the capture reaction to the ground state [16], also indicates a much lower S-factor.

It is therefore clear that a new direct measurement is needed to understand this discrepancy. The LUNA collaboration decided to perform an extended set of measurements on the ^{15}N(p,γ)^{16}O reaction using both gas and solid target setups. The LUNA facility, thanks to its underground location inside the Gran Sasso National Laboratory (LNGS), offers a unique opportunity for in-beam γ-rays spectrometry with very low count rate. I will discuss in detail these measurements in next chapters.

Chapter 2

The LUNA facility

LUNA (Laboratory for Underground Nuclear Astrpphysics) is placed in the Laboratori Nazionali del Gran Sasso (LNGS) near the city of L'Aquila in central Italy. This facility is up to now the unique underground accelerator in the world and it is dedicated to astrophysical nuclear measurements.

The LUNA project started with a 50 kV accelerator in order to study two important reactions of the pp-chain: ^{3}He(^{3}He,2p)^{4}He and d(p,γ)^{3}He. A new accelerator, with a 400 kV terminal voltage, has been installed in the year 2000 and it was used to measure ^{14}N(p,γ)^{15}O ^{3}He(α,γ)^{7}Be, ^{25}Mg(p,γ)^{26}Al and ^{15}N(p,γ)^{16}O.

In this chapter the advantages of an underground laboratories will be explained and the LUNA facility will be described together with the two experimental setups used for the study of the ^{15}N(p,γ)^{16}O reaction, subject of this work.

2.1 Underground measurements

The cross sections of nuclear reaction at the energies of astrophysical interest are of the order of nbarn and picobarn or lower. The measured rate of a reaction, n, is defined by the following equation (2.1):

$$n = I\sigma\epsilon N_t t \tag{2.1}$$

where I is the beam current quoted as the number of particle impinging the target in the unit of time, ϵ is the detection efficiency of the reaction products, N_t is the atom density of the target and t the target thickness. Putting the typical values of current and target composition of the most experiments of nuclear astrophysics we can calculate the reaction rate, which can differ from events/hour to events/months.

Most of the nuclear reactions of astrophysical interest are of the (p,γ), (p,$\alpha\gamma$) o (α,γ) type and they can be measured detecting the γ-rays in the produced reactions.

The γ-ray spectra, acquired by the acquisition system connected to the detectors, could be disturbed by the presence of different sources of background. The background in the γ spectrum could be divided in two main categorizes: the natural background and the beam induced background. Natural background is referred to all processes produced by the environment where the experimental setup has been placed and by the radioactive nuclide contamination in the detector itself. The beam induced background is the part of signals produced by the interaction of the beam with the setup material or the possible contamination inside the setup. The beam induced background will be discussed in this thesis (see sec. 3.5.1).

The background component in the spectra in absence of beam is called natural background and is produced mainly by two different sources:

- the cosmic radiation
- the radiation produced by the radioactive nuclides in the air (i.e. radon gas), in the rock (thorium, uranium and potassium) and in the building materials (thallium) and inside the detector itself

The cosmic radiation at the top of the atmosphere is mainly produced by an hadronic component (proton 92.4%, α particles 6.7% and heavy ions $< 1\%$) and a leptonic component (electrons). Hadrons have a very high interaction probability with atmospheric atoms (thickness of the atmosphere $\sim$1000 g/cm^2). For example, protons have an interaction length of about 90 g/cm^2, while α particles and heavier nuclei interact after smaller lengths [17]. The interaction of the primary cosmic radiation causes secondary cosmic rays at sea level: muons (70%), electrons (30%) and protons and neutrons ($< 1\%$). Muons are the most penetrating component and they produce background. The muon-induced background arises from direct ionization events in the detector volume, radioisotopes production via interactions with nuclei (for example, spallation), muon bremsstrahlung, production of δ electrons, muon decay ($\mu^{\pm} \rightarrow e^{\pm} + \nu + \bar{\nu}$), and electron-positron pair production. Furthermore, neutrons produced by muons through spallation processes in turn produce radioactive nuclei. The best solution is to install the experiment in a deep underground laboratory, where the rock shields against cosmic rays. The largest underground laboratory in the world is the Laboratori Nazionali del Gran Sasso (L.N.G.S.) in Italy. The laboratory is located in the motorway tunnel of the Gran Sasso mountain. Due to its mean thickness of 3800 m.w.e. (meter water equivalent), the flux of the most penetrating component of the cosmic rays, muons, is reduced by a factor of 10^6 with respect to the earth's surface [18]. In table 2.1 the reduction values for the most important sources of natural background in the experimental γ-ray spectra are shown.

The choice of the LUNA collaboration to install the accelerator in the LNGS (up to now LUNA is the unique underground accelerator) allows to study the reactions of astrophysical interest at energies much lower than what achievable in earth's surface laboratories.

The γ-ray spectrum at energies below 3 MeV is dominated by the γ-rays emitted by the radionuclides in the air, into the surrounding materials and the detector itself. To improve the signal to background ratio in the energy range below 3 MeV passive and active shielding are used. Usually passive shielding consists of an inner part made of copper surrounded by lead in order to reduce the γ-rays flux incident on the detector and also the X-rays and the

Particle	Energy MeV	Flux $cm^{-2}s^{-1}$	Reduction Factor
Muons	all spectrum	$2.52 \cdot 10^{-7}$	10^{-6}
Neutrons	$< 50 \cdot 10^{-3}$	$1.08 \pm 0.02 \cdot 10^{-6}$	10^{3}
Neutrons	> 2.5	$0.32 \pm 0.14 \cdot 10^{-6}$	10^{3}
Gamma	$0 \div 0.5$	78	5
Gamma	$0.5 \div 1$	25	5
Gamma	$1 \div 2$	2.5	5

Table 2.1: *Cosmic rays suppression at LNGS.*

low energy γ-rays due to the ^{210}Pb activity. In order to reduce the presence of radon gas usually the setup (consisting of the detector and the surrounding shielding) is inclosed in a box filled with nitrogen atmosphere (see section A and [19] for more details on the use of passive shielding for in-beam underground experiments).

2.2 The LUNA2 accelerator

The LUNA2 accelerator (400 kV maximum accelerating voltage) was delivered by the High Voltage Engineering Europe (HVEE). The high voltage (HV) is generated by an Inline Cockroft-Walton power supply. The tank is filled by a gas mixture composed by 75% of N_2 and the 25% of CO_2 at the pressure of 20 bar in order to avoid any possible spark due to the high voltage[20]. The basic operating principle is that the capacitors are charged in parallel to a common potential, but they discharge in series; the switching between the series and parallel connections is accomplished through rectifiers. As a result of this charging and discharging cycle, the terminal voltage is not costant, but has a small ripple that depends directly on the external load resistence and on the period of the charging voltage. The LUNA2 accelerator has 20 Vpp ripple at 400 kV for frequencies higher than 1 Hz as tested over several days.

The accelerator could produce two types of ion beam: proton and alpha particle. The ion beam is developed by a radio frequency (RF) source that is able to produce an high intensity beam current; as example 500μA of proton at the maximum possible energy (400 keV). The source bottle delivers the gas (hydrogen or helium) that is excited by the RF oscillator. The plasma is confined and positioned with an adjustable axial magnetic field and the ion source is mounted directly on the accelerator tube (Fig. 2.2). The ions are extracted by an electrode, which is part of the accelerator tube. The voltage of this electrode is thus included in the overall HV at the terminal.

The accelerator is equipped with an adjustable shortening rod that permits to maintain the high current intensity in all the accelerator voltage range, from 50 kV to 400 kV.

The accelerator parameters are controlled and monitored by a Windows computer situated in a control room next to the accelerator room. All the setting values and the condition parameters are saved in log files on the PC in order to be analyzed off-line in case of accelerator problems.

Figure 2.1: *The LUNA2 400 kV accelerator with the tank open for maintenance. Inside the tank, the metallic rings, keeping the ion source free from electric fields, are visible.*

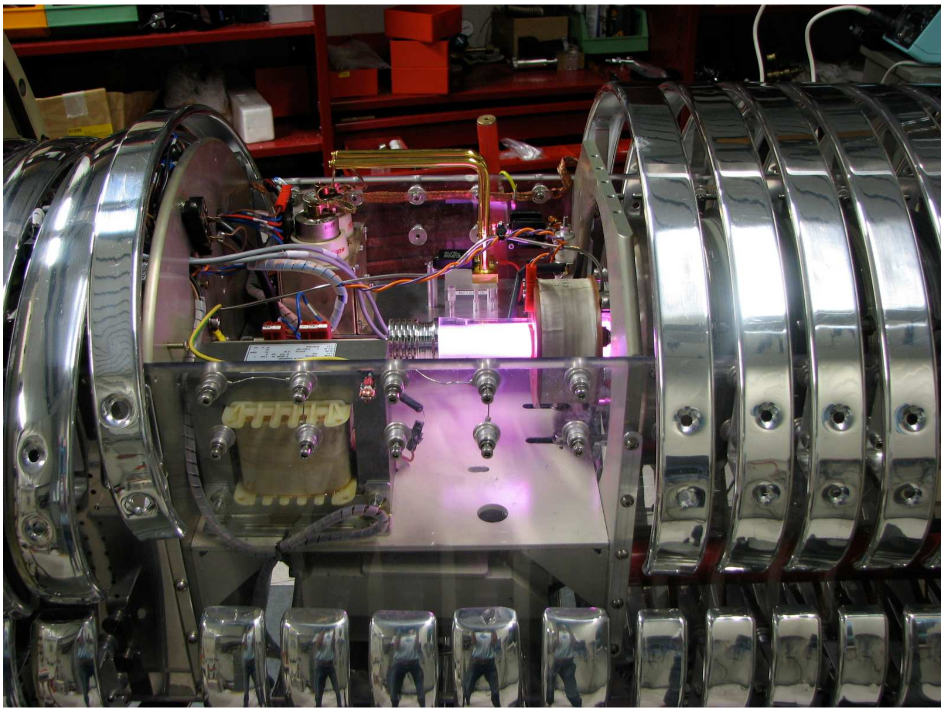

Figure 2.2: *The radio frequency ion source of the LUNA2 400 kV accelerator. The characteristic pink light of the hydrogen plasma is visible.*

$U_{terminal}$ and U_{probe}	$\Delta_{stat}E_p$ in keV	$\Delta_{syst}E_p$ in keV
80	0.07	0.3
100	0.07	0.3
150	0.06	0.3
200	0.06	0.3
250	0.05	0.3

Table 2.2: *Statistical and systematic error of the energy calibration.*

The energy calibration has been done using the non-resonant radiative capture reaction ^{12}C(p,γ)^{13}N [21, 20]. This reaction has a Q-value of Q = (1.94351±0.00027) MeV [22] and produces a direct capture γ-ray of energy $E_\gamma = Q + E_{CM}$. It is therefore suitable for an energy calibration over a wide energy range. Resonance radiative-capture reactions were also used to verify the calibration obtained with the ^{12}C(p,γ)^{13}N. The reaction used were: ^{23}Na(p,γ)^{24}Mg (E_p^{res} = 309 keV), ^{25}Mg(p,γ)^{26}Al (E_p^{res} = 316 keV and 389 keV) and ^{26}Mg(p,γ)^{27}Al (E_p^{res} = 338 keV).

The procedure for the energy calibration has been described in detail in [20]. The following calibration function has been finally obtained:

$$E_p = (U_{terminal} + U_{probe}) \cdot (0.9933 \pm 0.0002)\,\frac{\text{keV}}{\text{kV}} - (0.41 \pm 0.05)\text{keV} \qquad (2.2)$$

where $U_{terminal}$ is the accelerator voltage applied to the high voltage terminal, U_{probe} is the bias voltage applied to the anode ("probe") of the ion source. $U_{terminal}$ is measured with a chain of 0.1% precision high voltage resistors; both $U_{terminal}$ and U_{probe} are monitored on the accelerator control computer. The calibration slope is not equal to 1. This is due to a systematic effect in the high voltage resistor chain, while the offset can be explained by a potential drop in a poorly conducting region of the plasma inside the ion source. The offset was found constant over the range $U_{terminal}$ = 130 - 400 keV. In this voltage range the accelerator has been calibrated and at lower energies the calibration has been extrapolated. The systematic uncertainty derives from the uncertainty on the ^{12}C(p,γ)^{13}N reaction Q-value, which is 0.27 keV, and from an additional contribution of 0.1 keV from the calculation of the attenuation Doppler shift seen in the Germanium detector. When combined quadratically, it follows that $\Delta_{syst}E_p$ = 0.3 keV.

The energy spread of the accelerator is smaller than 0.1 keV [20] and the long term energy stability was better than 5 $\frac{\text{eV}}{\text{h}}$. In table 2.2 the statistic and systematic errors on the calibrations are reported for few energies.

2.3 The beam lines

The LUNA2 accelerator is connected to two channels by a dipole switching magnet. In this configuration we can focus the beam on two different setup typologies: gas target and solid target setups. The possibility to have in parallel these two configurations, with their substantial and unique properties, reduces the time preparation of the experiments, since the channel not used in the measurements could be used in the test phase. The beam can be delivered to one of the two channels applying a potential to the first dipole switching magnet. As a matter of fact a nuclear astrophysics experiment has to be optimized in all its part in order to reduce all the possible systematics.

In the next two section the two channels, used for the measurements of the ^{15}N(p,γ)^{16}O, will be presented.

2.3.1 The gas target channel

The main part of this channel is the differential pumping system. At low energies the cross section drops sharply with the energy. As a consequence it is impossible to divide the gas target from the chamber: the uncertainty on the beam energy due to the energy loss will be too large. Because of this, the differential pumping system has been chosen. The system (see Fig. 2.3) is composed by three pumping stages connected between them and to the chamber by small section tubes used also as collimators. The three collimators are cooled by water because they are hit by an intense beam during the measurements. In table 2.3 the tubes characteristics are reported, while in table 2.4 there are the pumps specifics.

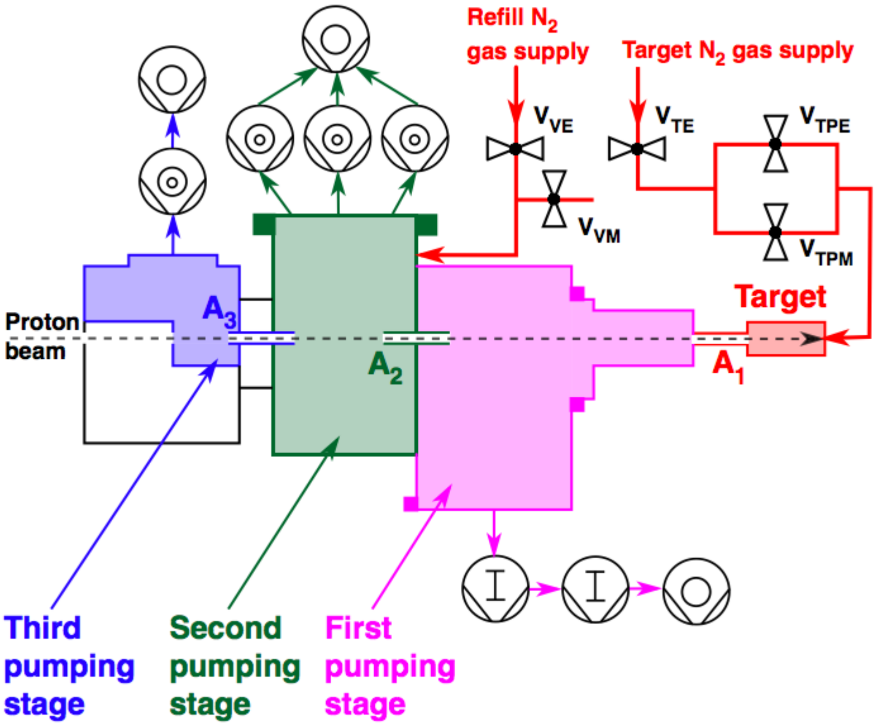

Figure 2.3: *The windowless gas target pumping system. The details for the collimator are given in the text.*

It can be seen that more than 99% of all the gas flow is transported by the first stage pumps. Already in the second pumping stage, the vacuum created by the three powerful turbo-molecular pumps is in the 10^{-6} mbar range. Thanks to third stage the system is able also to operate at a target pressure of 10 mbar instead of the 1 mbar adopted in the

Collimator	Lenght	Diameter	Current measurement
A_1	40	7	Current I_1 measured
A_2	105	10	Grounded
A_3	80	25	Current I_3 measured

Table 2.3: *Collimator dimension in millimeters.*

Stage	Pump	Operating principle	Nominal Speed $\left[\frac{m^3}{h}\right]$	Intake pressure [mbar]	Actual Speed $\left[\frac{m^3}{h}\right]$	Gas flow $\left[\text{mbar} \cdot \frac{m^3}{h}\right]$
1	Ruvac WS2000	Roots	2050	$7{\cdot}10^{-3}$	1100	7.7
	Ruvac WS501	Roots	505	$3{\cdot}10^{-2}$	400	
	Leybold Ecodry	Dry Forepump	40		40	
2	3 x Turbovac 1000	Turbomolecular	3 x 3600	$3{\cdot}10^{-6}$	3 x 1100	0.01
	Leybold Ecodry	Dry Forepump	40		40	
3	Pfeiffer TMH521UP	Turbomolecular	1800	$9{\cdot}10^{-7}$	1800	0.002
	Leybold Ecodry	Dry Forepump	40		40	

Table 2.4: *Pump system characteristics. The value in the last three columns are related to a pressure p_{T0} = 1 mbar.*

experiment. The gas can introduced in the chamber by a recirculating system or by a gas to lose system connected directly to the gas bottle. The gas flows in the chamber through a V_{TPE} valve controlled by the MKS control unit. This control unit checks the pressure p_{T0} measured by a Baratron MKS with a range of 10 Torr.

The feedback cycle, consisting of the capacitance manometer, the MKS control unit and the thermal leak valve V_{TPE}, keeps p_{T0} constant to better than 0.1%.

The presence of the gas inside the chamber prevents the current measurements using a Faraday cup due to the secondary electrons. They are produced by the beam interaction with the gas. A constant temperature gradient calorimeter has been installed at the end of the chamber in order to measure the beam intensity and it is also used also as beam stop.

The hot surface of the calorimeter, where the beam is absorbed (see Fig. 2.4), consists of a copper disk 41 mm thick. It is kept at a constant temperature $T_{hot} \equiv 70.0$ °C by eight resistances of 50 W each glued on the surface.

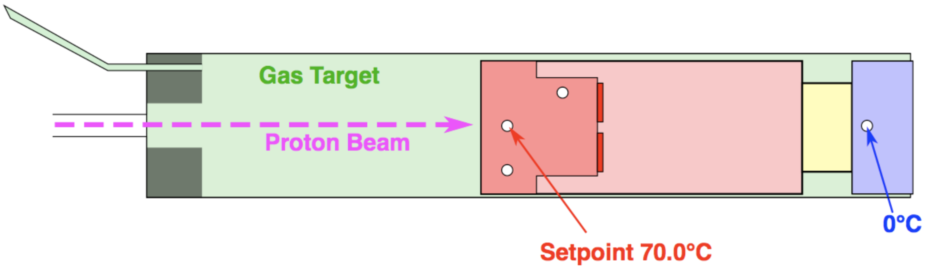

Figure 2.4: *Calorimeter for the measurement of the beam intensity. The heating resistors are marked as thick red lines. The white circles represent thermoresistors for measuring the temperature.*

The resistances are powered by direct current (DC) controlled by an analogic module NILF (National Instrument Labview FieldPoints). The temperature has been monitored in three different points on the surface by termo-resistance PT100 and all the result were saved every 5 seconds in order to have a complete monitoring for the offline analysis. In the ^{15}N(p,γ)^{16}O analysis some spectra were discarded because the beam was too much variable during the measurement.

The cold surface of the calorimeter was at a temperature of 0 °C thanks to a liquid cooling system with a variation of 0.3 °C in 24 hours.

The principle of the beam power measurement is to measure the power W_0 required for maintaining the setpoint condition $T_{hot} \equiv$ 70.0 °C (typically, $W_0 \approx$ 135 W without beam on the target).

Without the beam the power is only furnished by the resistances. When the beam is on the calorimeter it warms up the calorimeter surface so the needed power is lower than in the case of absence of beam. During the run, the power W_{run} required to maintain the set point temperature is measured and logged every five second too. With W_{beam} representing the power deposited by the beam on the beam stop, it follows:

$$\begin{aligned} W_{beam} &= W_0 - W_{run} && (2.3) \\ I_{target} &= \frac{W_{beam}}{E_{cal}} q_e \\ &= \frac{W_0 - W_{run}}{E_p - \Delta E_{target}} q_e && (2.4) \end{aligned}$$

I_{target} is the target current and $E_{cal} = E_p - \Delta E_{target}$ is the energy of the ion beam when it hits the calorimeter. ΔE_{target} is taken from the stopping power compilation by Ziegler [23] and is proportional to the target density.

2.3.2 The solid target channel

The beam-line dedicated to measurements with solid targets is connected to the accelerator by the first dipole magnet. The beam goes through the zero degree exit of this magnet and then it passes through another dipole switching magnet (second magnet) that deviates the beam by an angle of 45 °C. The beam deviation selects the $\frac{q}{m}$ ratio removing the contaminations inside the beam itself. Between the first and the second magnet there is a Faraday cup (called FC0) where we can measure the beam current produced by the accelerator. After the second switching magnet the beam will be focused by three apertures cooled by water. The three apertures (or collimators) have a diameter of 10.0 mm, 3.0 mm and 5.0 mm, respectively and they are placed at a distance of 100 cm, 70 cm and 20 cm, respectively. The presence of three different collimators puts a constraint on the beam dimension. During the experiment the current on each aperture was measured with amperometers. We acquired all spectra with the same condition of the current on all apertures. After the third collimator a cold trap has been placed. It stops impurities from being deposited on the target surface. The cold trap, electrically isolated from the target chamber, is made of copper and it is 20

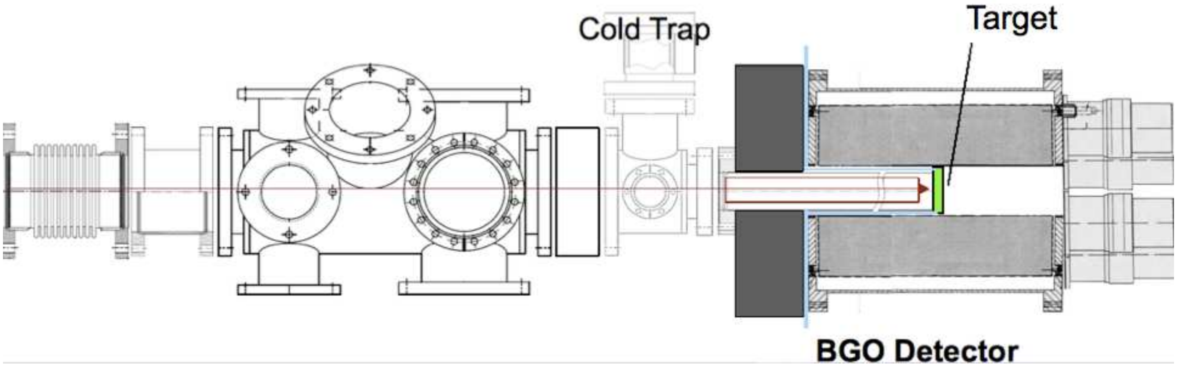

Figure 2.5: *The scheme of the solid target channel from the second dipole magnet. The cold trap and the BGO detector are also shown.*

cm long. It ends at few millimeters from the target and it is cooled at the liquid nitrogen temperature. The target was isolated by the channel and it was connected to the chamber. The current was measured on the system target plus chamber. A negative high voltage (HV = - 300 V) is applied to the cold finger in order to suppress the out coming electrons from the target when it is invested by the beam. The target backing closes the beam-line and is directly in contact with the water of the cooling system.

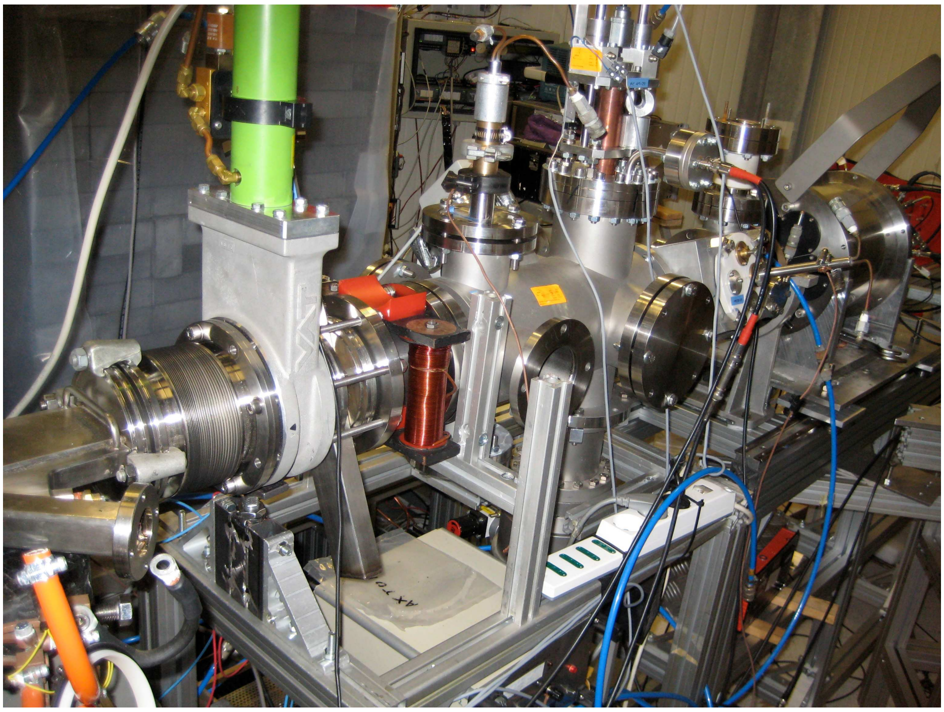

Figure 2.6: *The solid channel during the alignment. On the left there is the connection with the second dipole magnet. In the picture it is possible to see also the BGO placed around the target.*

The beam current is measured directly on the target. The target is electronically connected to the target chamber in order to maximize the efficiency in the charge collection. The target has been made by titanium nitride sputtered on a tantalum backing (see sec. 4.2.1

for more details). The tantalum has a good electric contact with the target materials, it could not be activated by the beam and it does not produce nuclear reactions with the proton at the LUNA2 energy range. The backing has also an high fusion point and it is stable against beam heating.

The BGO detector was placed around that the target (see Fig. 2.5).

2.4 The 4π BGO detector and the electronics

In both the two phases of the experiment we used a Bismuth Germanate inorganic scintillator (chemical composition $Bi_4Ge_3O_{12}$, commonly called BGO) detector [24] made by SCIONIX. The high atomic number and density of the Bismuth (Z_{Bi} = 83) grants an high detection efficiency also at energies above 10 MeV (the γ-rays emitted by the ^{15}N(p,γ)^{16}O have an energy around 12 MeV), but the energy and temporal resolution of the detector are not optimal. The detector crystal is a cylinder 28 cm long with a coaxial hole Φ = 6 cm diameter and a radial thickness of 7 cm. The crystal is optically divided into 6 six sector each of them coupled to two Hamamatsu R1847-07 photomultipliers (PMTs). The scintillation light produced in each segment is detected by the connected PMTs We used this configuration in the setup in the gas target setup, whereas only one PMT was mounted on each sector of the BGO for the solid target setup because of geometrical reason. In Fig. 2.7 and Fig. 2.8 there are the pictures of gas and solid configurations of BGO, respectively.

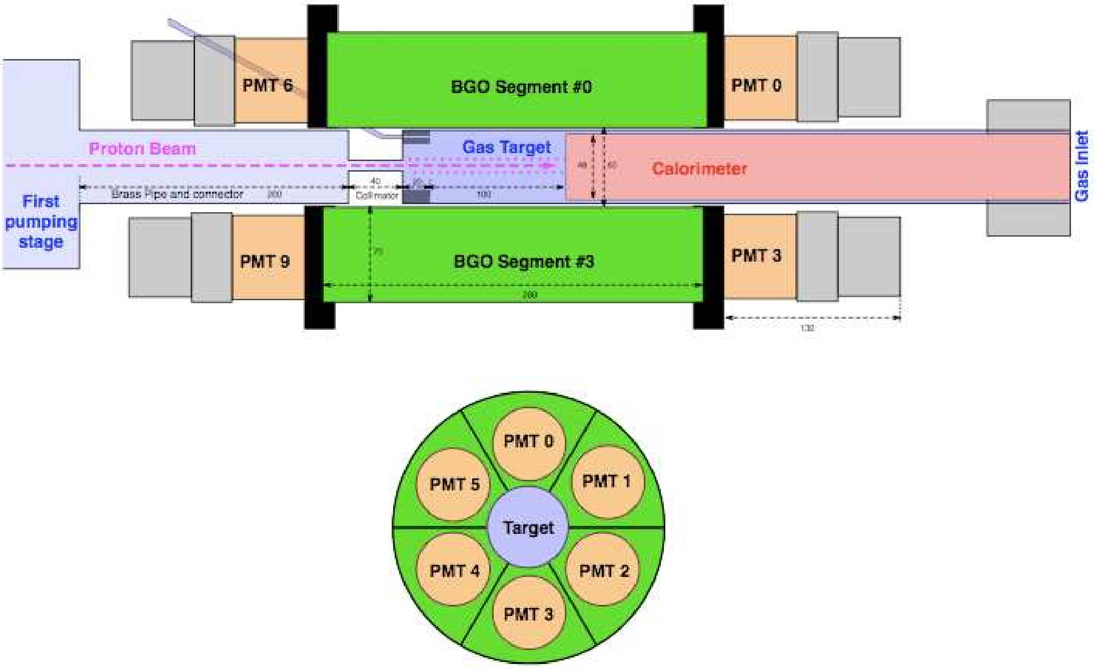

Figure 2.7: *BGO detector in the configuration used for the* ^{15}*N(p,*γ*)*^{16}*O experiment with gas target setup. The photomultipliers positions are indicated in two different lateral views. The BGO crystal is shown in green, the target area in blue and the photomultipliers in orange. All dimensions are given in mm.*

In each setup the target was totally surrounded by the BGO detector in order to improve the efficiency. The detector covered almost the total part of the solid angle. The signal from the six crystals could be acquired separately for each crystal (single mode) or summed altogether (sum mode). Summing the signals produced in all six sectors allows to recover the full energy of the detected γ-rays. The sum mode increases also the efficiency in the case of cascade transition to intermediate levels, leading with high probability to a summing peak at the total γ-ray energies. On the other hand the optical separation of each sector facilitates the pile-up rejection.

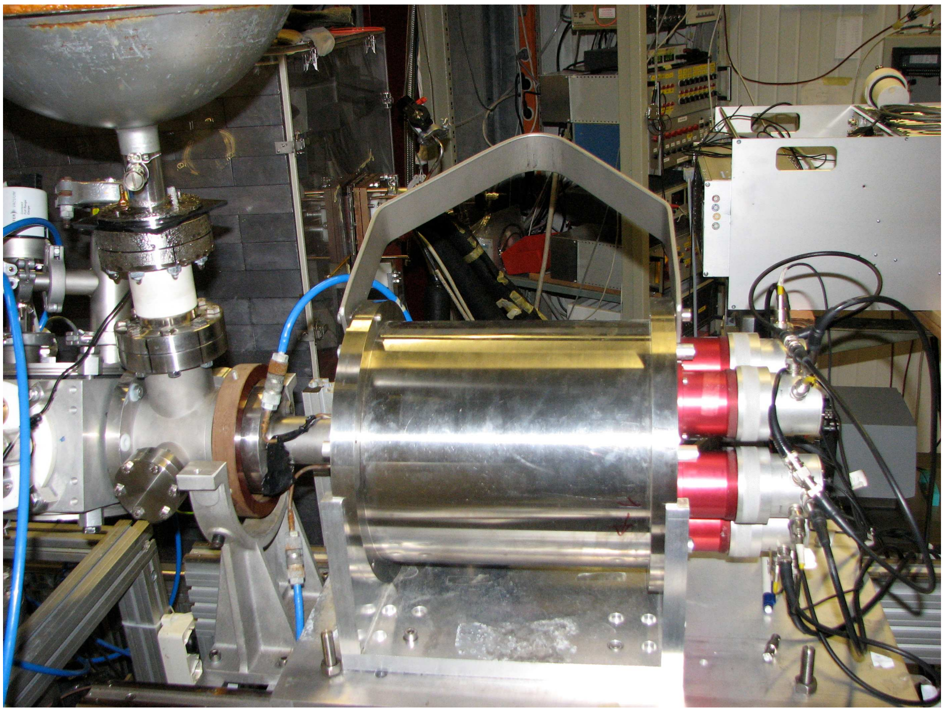

Figure 2.8: *BGO detector in the configuration used for the* ^{15}*N(p,*γ*)*^{16}*O experiment with solid target setup.*

The detector was connected to two different acquisition system in the two experiment performed at the LUNA accelerator. In the case of the gas target setup the signals from the 12 PMTs were added in a preamplifier, amplified and recorded in a standard Ortec multichannel analyzer. For solid target setup we used a dedicated data acquisition (DAQ) system called LUNA-FAIR. In this configuration the signal from each of the 6 PMTs was separately amplified and recorded in the 6 channels of the DAQ. The dynode signals were added in order to produce the trigger signal when the summed signal corresponds to $E_\gamma > 0.7$ MeV. When the DAQ was triggered all the six channels are read out. As a consequence we are able to record the γ-spectra event per event (list mode). The threshold was chosen at that level to minimize the dead time due to the natural background.

The electronics used for the Ortec MAESTRO data acquisition chain were:

- Last dynode signal of each photomultiplier
- Ortec scintillation preamplifier

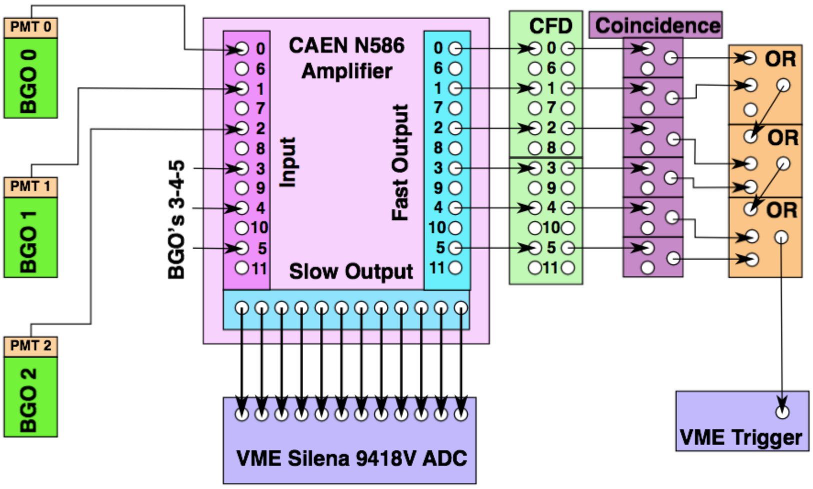

Figure 2.9: *Schematic layout of the LUNA-FAIR DAQ chain. Shown are the relevant channels of the 16-fold amplifier, constant fraction discriminator (CFD), coincidence and logical OR units.*

- NIM Ortec 672 spectroscopic amplifier
- NIM Ortec 919E EtherNIM multi channel analyzer
- Wndows XP computer for DAQ control, istogram read-out and histogram saving with commercial Ortec MAESTRO software

The electronics used for the LUNA-FAIR data acquisition chain were:

- Anode signal of each photomultiplier
- NIM CAEN N568B 16-channel spectroscopic amplifier
- NIM Costant Fraction Discriminator (CFD) EG&G CF 8000
- NIM Coincident unit
- NIM Logical Fan-in / Fan-out unit
- VME Silena 9418V 32-channel ADC
- VME LUNA-FAIR data acquisition computer, real-time operating system LynxOS
- Linux computer for DAQ control, histogram read-out and list mode data saving with dedicated software

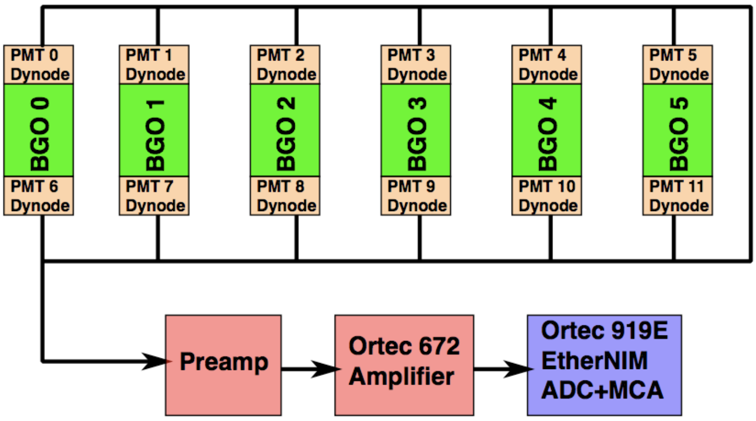

Figure 2.10: *Schematic layout of the Ortec MAESTRO DAQ chain. The amplification for each channel is adjusted by fine-tuning the PMT high voltage with the procedure described in the text.*

Chapter 3

^{15}N(p,γ)^{16}O cross section from the gas target experiment

The first approach to the study of the ^{15}N(p,γ)^{16}O reaction was a new analysis of the γ spectra acquired in 2003-2004 for the measurements of the ^{14}N(p,γ)^{15}O reaction. This experiment has been described in [3, 4] and was performed with the gas target setup already described in sec. 3.8. In the natural nitrogen gas there is a small amount of ^{15}N, still enough to perform the evaluation of the S-factor of the ^{15}N(p,γ)^{16}O reaction at the energies of novae scenarios.

In this chapter the analysis procedure will be described. In particular I will discuss in details the efficiency detection evaluation and the spectra analysis. Also the isotopic composition of the target will be explained.

3.1 Isotopic composition of ^{15}N in various materials

The yield is directly proportional to the number of ^{15}N nuclei in the target and in order to extract the S-factor it is important to determine this number with a good precision. In the case of the gas target experiment the gas used in the chamber was natural nitrogen. The isotopic enrichment of ^{15}N in nitrogen is used as a tracer of different biological and chemical processes and has therefore been the subject of much study, mainly in the geoscience. Sensitive methods to measure the ratio ^{15}N/N$_{TOT}$ have existed for a long time, and the main results have been reviewed [25]. The isotopic standard for ^{15}N is simply atmospheric air, which has been shown [26] to be sufficiently well-mixed that it does not deviate by more than 2.6% from the average, with most measurements even closer to the standard value.

Even other materials such as commercial nitrogen from a bottle [27] display isotopic ratios that are very close to the standard 0.3663% (Fig. 3.1).

In September 2007, the isotopic ratio of ^{15}N in the gas of the bottles (chemical purity 5.5 corresponding of 99.9995% natural nitrogen) used by LUNA was analyzed in three different laboratories using mass spectroscopy. This bottle-pack has the same characteristics and is furnished by the same supplier as the bottle-packs that provided the target gas for the LUNA

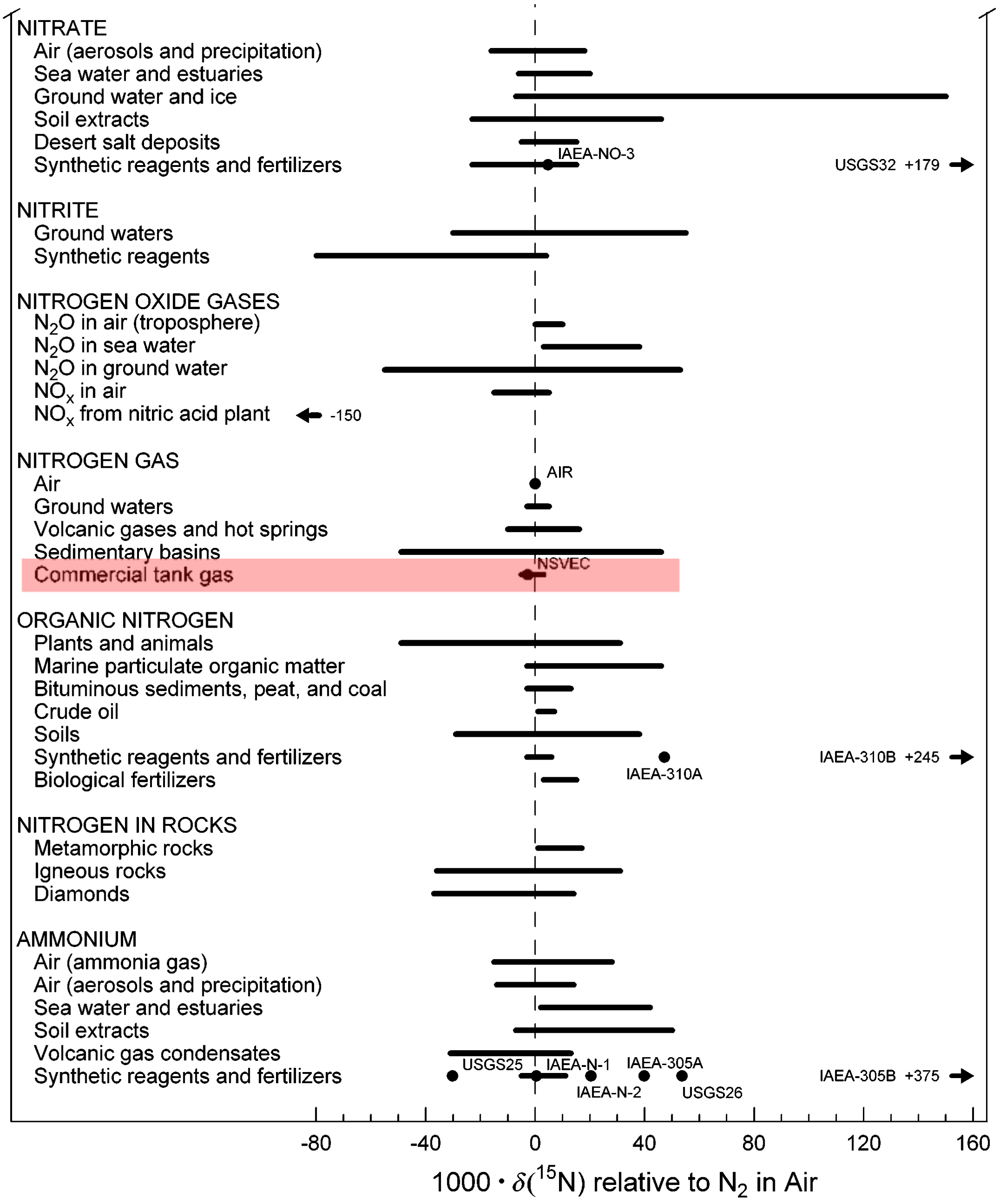

Figure 3.1: *Isotopic abundances of* ^{15}*N, plotted are the permille deviations from the standard. The figure has been adapted from [25].*

experiment in 2003-2004.

The resulting enrichment is expressed as

$$\delta^{15}N = \left(\frac{\frac{A^{sample}(^{15}N)}{A^{sample}(^{14}N)}}{\frac{A^{standard}(^{15}N)}{A^{standard}(^{14}N)}} - 1 \right) \cdot 1000 \tag{3.1}$$

with the standard being atmospheric air. The discrepancy from the standard value is expressed in permille as in literature [25]. The measurments were done with high precision and their results are reported in table 3.1. However, for the purpose of the present work much less precision is needed, so a conservative uncertainty that covers all three measurements has been adopted (table 3.1).

Sample	Measured at	δ^{15}N		
A	CIRCE Caserta	-27.2	±	0.3
B	MPI Biogeochemistry Jena	-1.1	±	0.2
	ATOMKI Debrecen	-0.4	±	0.2
Adopted for the present work		0	±	30

Table 3.1: *Isotopic ratio of the Gran Sasso nitrogen samples.*

The final value in the analysis was 0.366±0.011.

3.2 Target density and beam heating

The reaction yield is directly proportional to the density of the gas, deduced from the pressure value. The target density changes during the in-beam measurements due to the beam heating effect. The beam loses energy inside the gas and as a consequence the temperature increases thinning the target along the beam axis. Fig. 3.2 shows the set-up we used to measure such effect in the experiment. The small NaI detector is movable along the beam axis and it is shielded with lead (hole diameter 5 mm, lead thickness 70 mm). From the position of the E_R = 259 keV ^{14}N(p,γ)^{15}O resonance along the axis (and the beam energy at the target entrance) the energy loss has been obtained and then the target nuclei density has been calculated. For instance, at the beam current of 100 μA and a pressure in the target of 1 mbar, a density reduction along the beam has been measured to be about 7% as compared to the one given by the perfect gas law. The target density study has been described in details in [3, 4]. Finally the target density n is obtained as:

$$\frac{n}{n_0} = (0.968 \pm 0.013) - (4.59 \pm 0.34) \cdot 10^{-3} \frac{dW}{dx} \left[\frac{\text{mW}}{\text{mm}} \right] \tag{3.2}$$

where n_0 is the density at T = 296 K and $\frac{dW}{dx}$ is the power deposited in the gas target by the ion beam calculated according to:

$$\frac{dW}{dx} = n_0 \cdot \frac{dE}{dx} \cdot I_{target} \tag{3.3}$$

where $\frac{dE}{dx}$ is the stopping power and I_{target} the beam current.

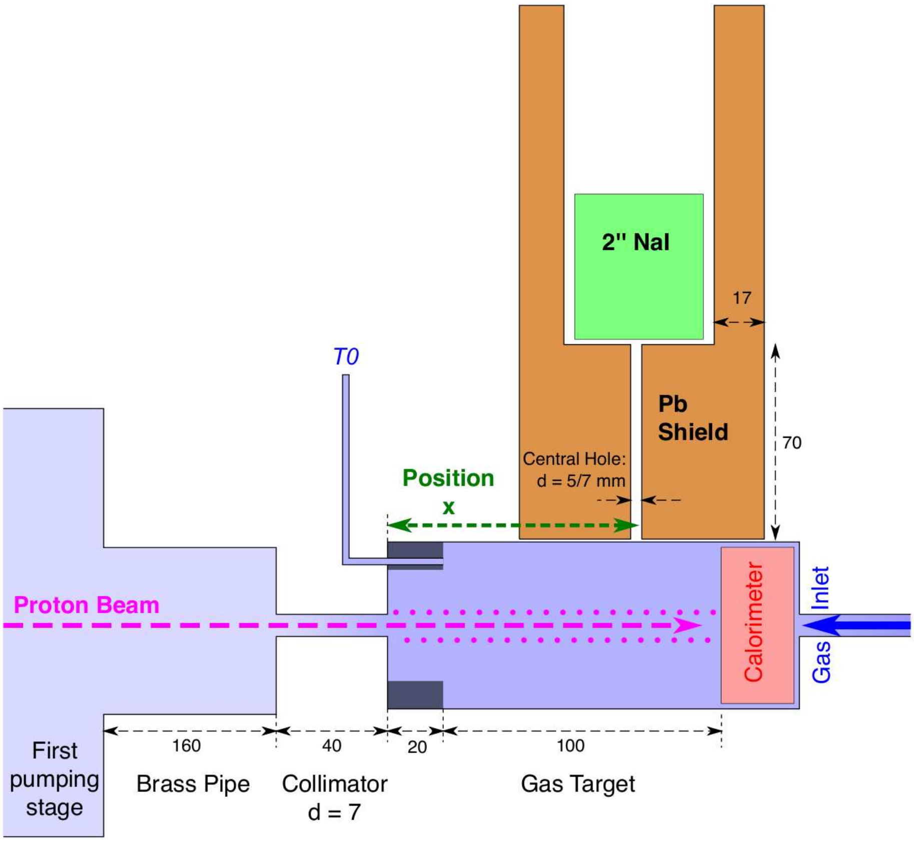

Figure 3.2: *The setup used to measure the beam heating effect.*

3.3 Localization of contaminants

In the experiment, a BGO detector with high detection efficiency, but low energy resolution, was used. As a consequence, it was necessary to study the beam induced background previous to the actual experiment with a HPGe detector with lower efficiency but much better resolution. In particular, in a gas target setup the contaminant localization is a critical point. As a matter of fact the cross section for γ-ray emission by the contaminant depends on the beam energy. If the contaminant is located at the beginning or at the end of the target chamber the beam energy varies due to the energy loss through the gas target. In our setup the main contaminant was the boron and its presence on the collimator or on the calorimeter would change the analysis results.

A 125% HPGe detector was employed for this purpose. A close geometry (see Fig. 3.3) was selected in order to have a high enough absolute detection efficiency to be able to identify all relevant background sources from their γ-lines. In this configuration it is impossible to localize the weak background components by moving the detector closer to different parts of the setup, but, knowing that the focused beam could only interact with the collimator (5% of the beam current) and on the calorimeter, we can use a doppler technique in order to localize all contaminant sources.

The germanium spectra were acquired at several beam energies from 100 keV to 200 keV with a gas pressure of 1 mbar (the same used in the measurements with the BGO detector) and without gas in the chamber in order to see a possible differences.

In a radiative capture transition to the exited state E_x of the compound nucleus, the reaction takes place at a beam energy E_p and is characterized by its Q value and the masses m and M for the projectile and target, respectively. The detected energy E_γ of the γ-ray is then given by the relation [6]:

$$E_\gamma = Q + \frac{M}{m+M} E_p - E_x - \Delta E_{Recoil} - \Delta E_{Doppler} \tag{3.4}$$

The recoil correction ΔE_{Recoil} and the Doppler correction $\Delta E_{Doppler}$ are given by:

$$\Delta E_{Recoil} = \frac{E_\gamma^2}{2(m+M)c^2} \tag{3.5}$$

$$\Delta E_{Doppler} = \frac{v}{c} E_\gamma \cos\theta = \frac{\sqrt{2mE_p}}{(m+M)c} E_\gamma \cos\theta \tag{3.6}$$

where θ is the angle between the beam axis and direction of emission of the γ-ray and v the velocity of the recoiling nucleus in the medium at the time of emission of the γ-ray.

Since we need only to distinguish between two very different positions ($\Delta x \approx 16$ cm) the method can also be applied in close geometry (see Fig. 3.3). The experimental correlation between E_p and E_γ could be studied in order to deduce the position of all contaminants. In particular the boron was found to be on the collimator.

Another method in order to evaluate the boron position with the BGO detector is discussed in section 3.7, because this is one of the most critical point in the analysis.

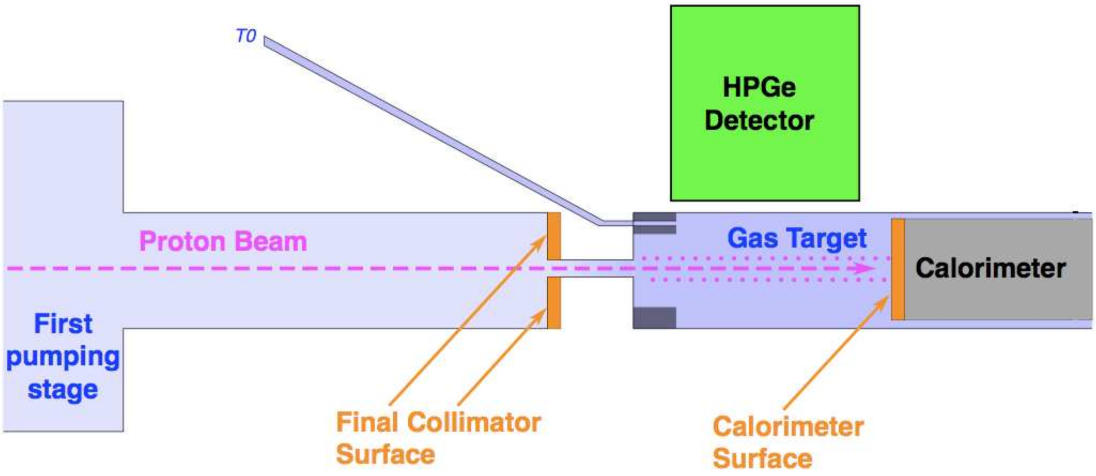

Figure 3.3: *Setup for the beam-induced background study. The two main sources of beam induced background, i.e. at the surfaces of the final collimator and of the calorimeter are marked in orange.*

3.4 Detector efficiency

The detector efficiency was evaluated for the gas target and the solid target experiment separately due to the relevant differences between the two setups (target length, passive layers, number of PMTs for each crystal). In this section the efficiency evaluation for the gas target setup is described.

Since there is not a radioactive source that produces a γ-ray at 12 MeV (the energy of the γ-ray emitted by the ^{15}N(p,γ)^{16}O) a GEANT4 [28] code has been developed to evaluate the efficiency.

3.4.1 Detector description

The geometry of the detector was taken from previous work [29] used for the analysis of the ^{25}Mg(p,γ)^{26}Al measurements that were done in 2007. Since the magnesium experiment was done with solid target setup the chamber description has been corrected to take into account the present setup. The detector and all the passive materials have been checked in the GEANT4 visualization mode (Fig. 3.4).

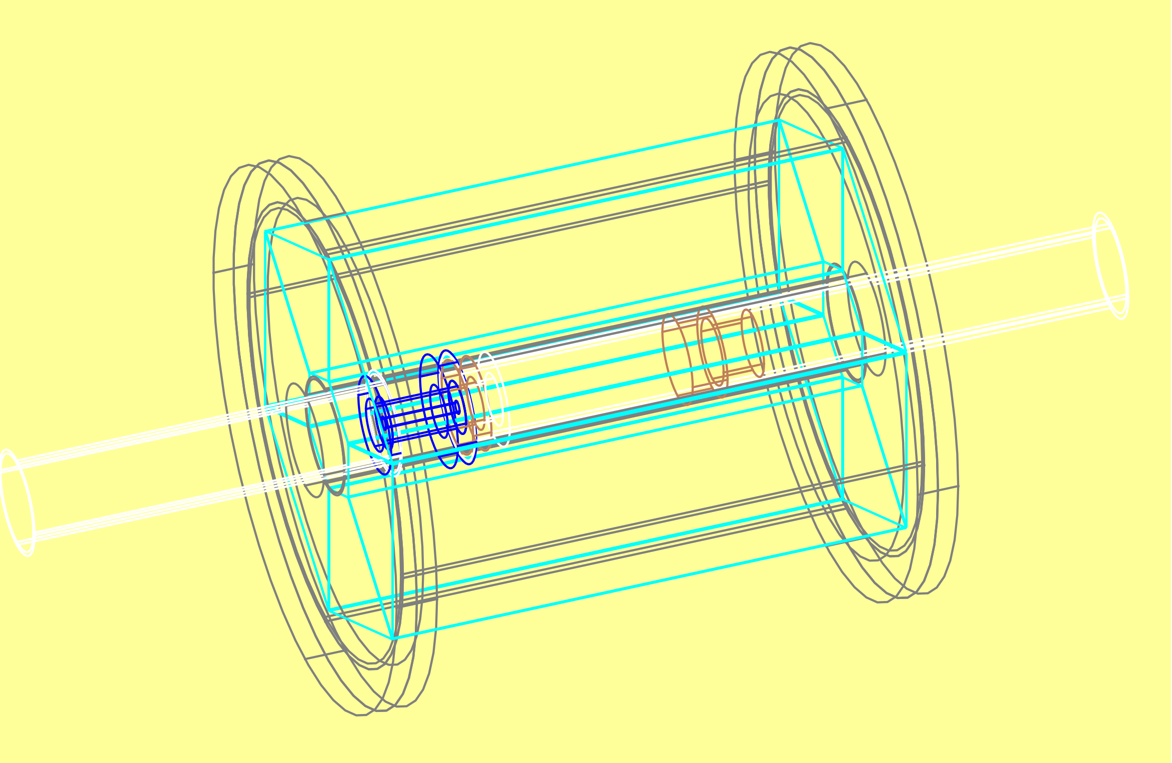

Figure 3.4: *BGO detector, together with all the passive materials modeled for the present description.*

3.4.2 Validation using radioactive sources, without target chamber

GEANT4 has been checked in several experiments [30]. In particular, the geometry of the active and passive materials have to be described in the code with high precision in order to simulate the correct detector response. The low energy γ-rays would be the most affected by wrong description of the geometry. For this reason the simulation was compared to runs acquired with two different calibrated sources: ^{137}Cs and ^{22}Na (a weak enough ^{60}Co source was not available at the time). For this comparison the target chamber was not included. The measurements were done with the sources in different position inside the detector along the beam axis. The count-rate of the ^{137}Cs spectra taken at various position inside the detector were reproduced to within better than 1%. The reproduction of the ^{22}Na count-rates (Fig. 3.5) was somewhat inferior, in same cases only 3% could be reached. The ^{137}Cs (^{22}Na) source calibration was known to 1.5% (3.1%) with 1σ uncertainty.

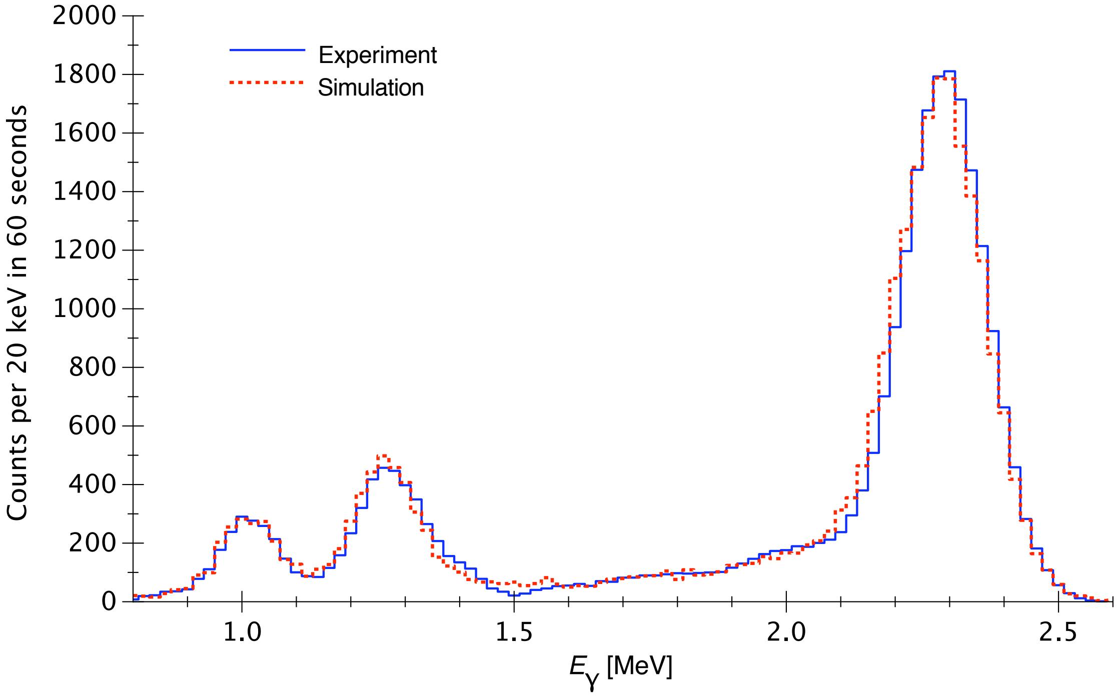

Figure 3.5: *Experimental and simulated spectra for a position near the center of the BGO crystal. The target chamber was not included in experimental spectrum.*

3.4.3 Validation using radioactive sources, with gas target chamber

The passive materials of the BGO crystals support are well described in the simulation as shown in the previous section and in Fig. 3.5. In order to check also the description of the chamber geometry runs with a ^{22}Na source have been performed with the target chamber and collimator present. Since near the collimator there is the most important presence of passive materials the most difficult case was to reproduce the experimental data in the position closest to the collimator (Fig. 3.6). The ^{137}Cs spectra, taken during the same period, were not used for quantitative purposes because the low energy cut-off in those spectra hampered the integration of the full-energy peak. The ^{22}Na spectra are well reproduced by the code, as shown in Fig. 3.5. This shows that the passive chamber materials are properly described, at the level of precision of the source calibration (3.1%).

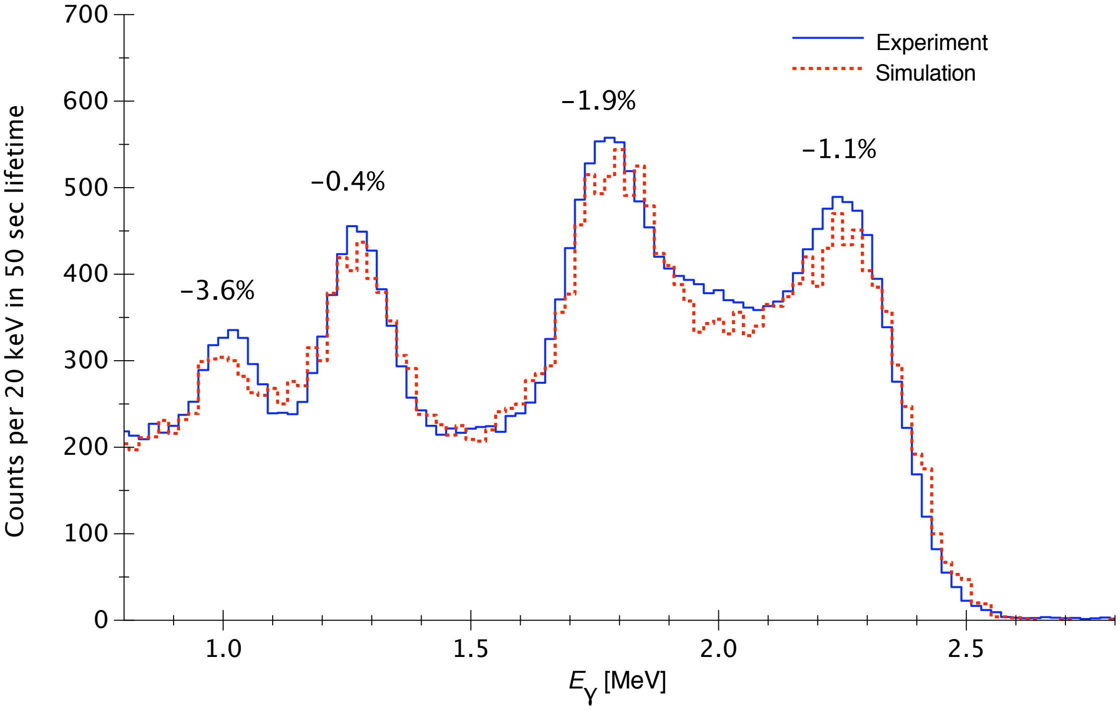

Figure 3.6: *Experimental and simulated spectra for a position near the final collimator. The position of the* ^{22}*Na source was adjusted by 6 mm in the simulation to fit the peak height ratios. The laboratory background has been subtracted from the experimental spectrum. The relative difference between experimental and simulated spectrum is given next to each peak.*

3.4.4 Comparison with previous GEANT3 simulations

In the previous study of the ^{14}N(p,γ)^{15}O reaction with gas target setup an other simulation code [24, 31], based on GEANT3, was used and the reliability of this code was tested in different analysis [3, 4] and compared to the experimental results [2] with very good agreement.

The new code has been compared with the GEANT3 in order to check if the GEANT4 code gives results consistent with the previous one.

GEANT4 simulated detection efficiency curve for 12 MeV γ-ray in function of the beam axis is shown in Fig. 3.7. It is superimposed with the same result from the previous GEANT3 code. This comparison shows a good overall agreement. However, the GEANT4 curve is systematically lower than the GEANT3 curve near the beginning of the target chamber. In this area the collimator and the chamber together with the brass pipe are connected by a teflon insulating ring and some metal. The position and dimension of all pieces were verified, however no errors have been found. The discrepancy amounts to 9% in this 20 mm long region, but over the 120 mm long target chamber the two simulations agree within 1%.

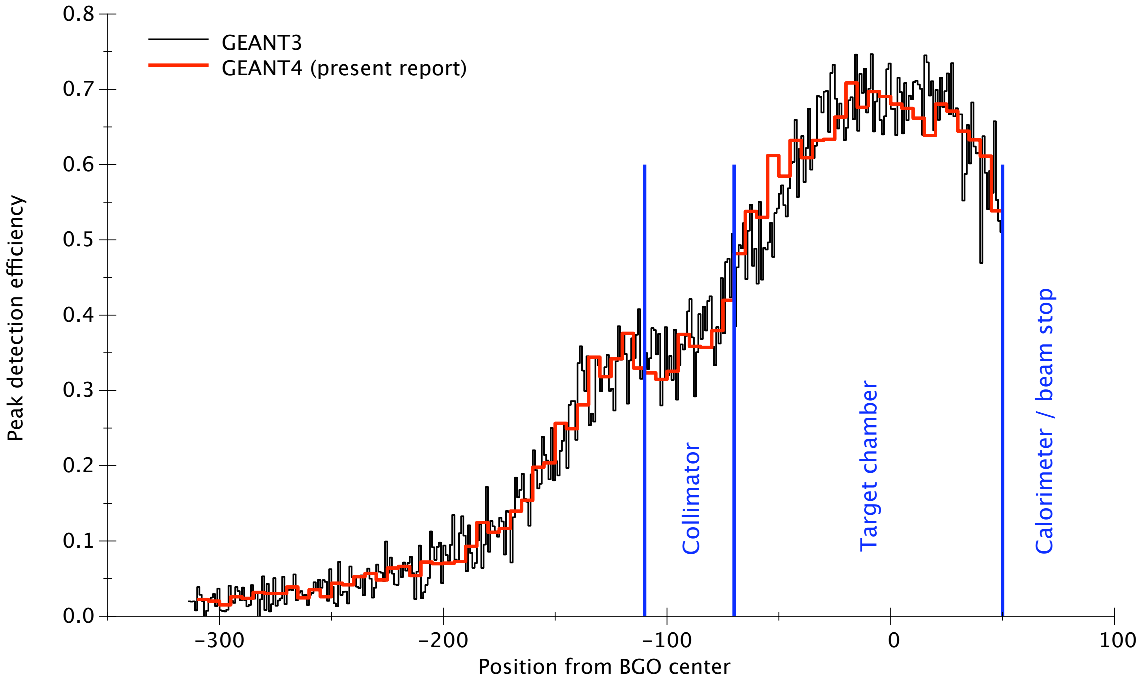

Figure 3.7: *Detection efficiency for detecting* ^{14}*N(p,*γ*)*^{15}*O* γ*-rays in the 6.5-8.0 MeV region of interest, for the run at* E_{beam} *= 100 keV. Black thin (red line), GEANT3 simulation (present GEANT4 simulation, in total 30000 emitted* γ*-rays.*

The final uncertainty from this validation procedure is evaluated to be 4%.

3.4.5 Angular distribution and cascade transitions

The summing detector efficiency evaluated with GEANT4 depends, however, also on inputs from experiment, such as the decay scheme and the angular distribution of the emitted γ-radiation.

The branching ratio for cascade through excited state is reported in literature [32]. A small branching on the 7.117 MeV ($J^\pi = 1^-$) level and on the 6.049 MeV ($J^\pi = 0^+$) level have been detected (Fig. 3.8). In the case of capture into the 0^+ first excited state at 6.049 MeV the secondary state decays through e$^+$e$^-$ emission and the transition from that level remains undetected.

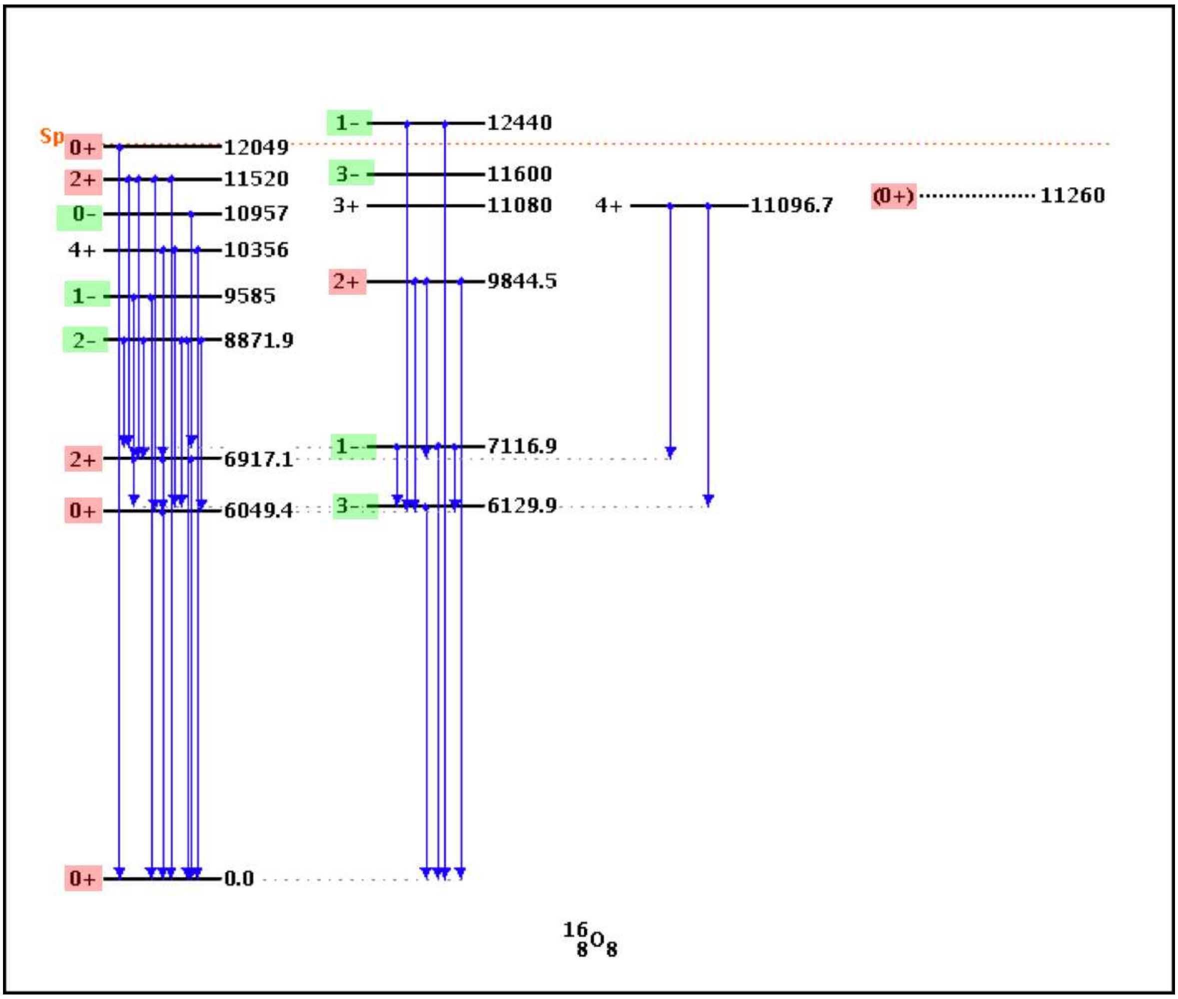

Figure 3.8: *Level scheme of the ^{16}O nucleus. Many levels are in principle accessible for E1 and E2 capture. The proton separation energy is shown by a dotted red line.*

The experimental cascade transitions were partially studied also at the LUNA accelerator analyzing the spectra acquired with a germanium detector and the gas target setup and with a HPGe Clover detector [5] that was used to study the ^{14}N(p,γ)^{15}O. The details are discussed in sec. 3.6.

The effect of the cascade through the level at 7.117 MeV was simulated in two opposite conditions of branching ratio: 0% and 100% as shown in Fig. 3.9 The effect on the

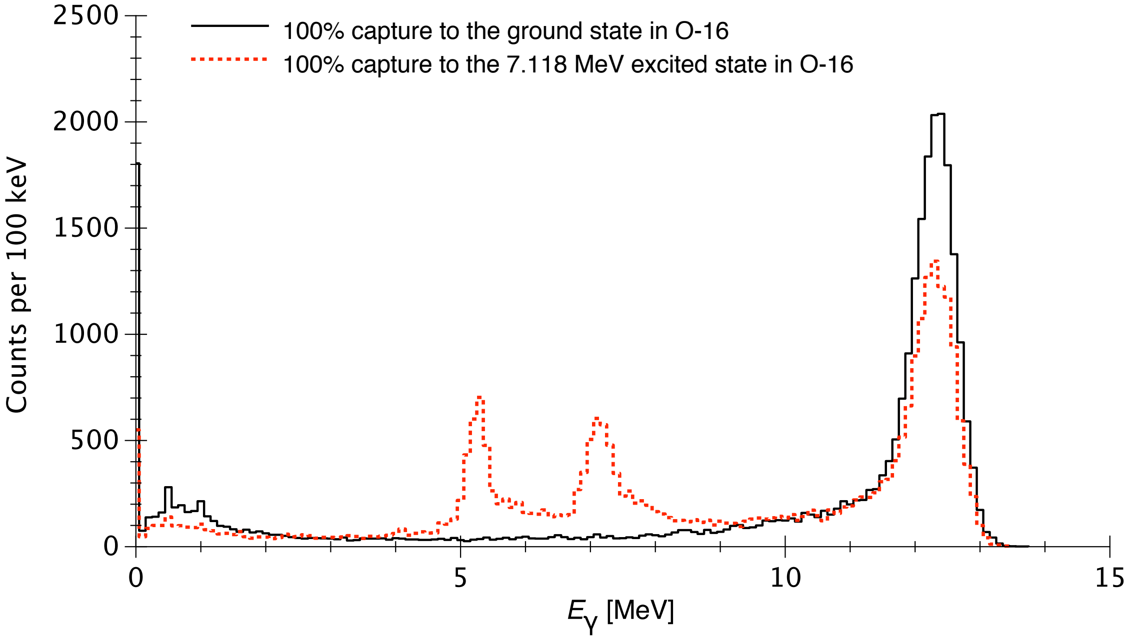

Figure 3.9: *Simulation of the effect of a possible cascade transition on the detection efficiency.*

efficiency for detection in the 9.7 - 13.5 MeV full-energy-peak region is reduced by 27% for 100% branching trough this level.

Combined with the previous mentioned experimental upper limits (section 3.6) obtained below and above the E_{lab} = 335 keV resonance, possible cascades give a 1.8% contribution to the total systematic uncertainty on the BGO detection efficiency.

The angular distribution is an other parameter which has to be taken into account to simulate efficiency particularly if the target has an extended length, as in this case. The angular distribution has been measured by Rolfs and Rodney [14] on the resonance at E_p = 1028 keV and was found to be isotropic and has been assumed isotropic. Consequently we assume isotropic in the present analysis. The simulation shows that due to the large solid angle covered by the BGO the detection efficiency is enhanced only by 4% if assuming a complete $\sin^2\theta$ shape instead. In order to account this effect, 4% is adopted as systematic uncertainty.

3.5 Spectra analysis

During the data taking γ-ray spectra were acquired at twelve different energies in a range from 100 keV up to 250 keV. For each beam energy two spectra were recorded: with nitrogen gas in the target chamber and with helium as gas target. In the case of nitrogen the chamber was filled with a pressure of 1 mbar for all the measurements while in the case of helium (chemical purity 99.9999%) with a range of pressure from 0.5 mbar to 2.0 mbar. The helium runs were done in order to monitor the beam induced background during the mea-

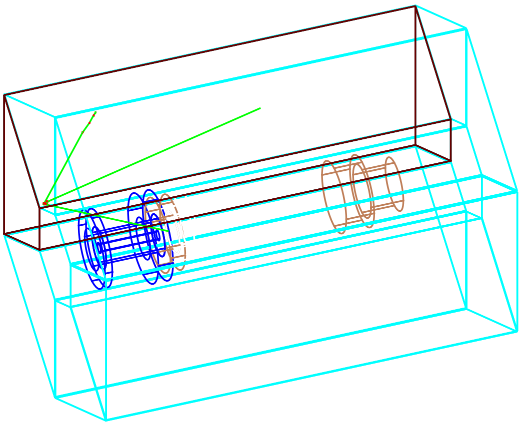

Figure 3.10: *Event caused by a 12 MeV γ-ray inside the BGO detector. The passive materials shown in Fig. 3.4 have been considered in the simulation, but were omitted from this figure for clarity. The final collimator and the calorimeter are shown.*

surements. In addiction laboratory background spectra were acquired during accelerator downtimes.

The spectra analysis will be described in details in next sections, but before I would discuss the shape of the spectra. In the following the structure of the γ-ray spectra will be analyzed in order to explain each peak. At low γ-ray energies ($E_\gamma \leq 4$ MeV) the in-beam spectrum is dominated by the natural background and the resultant pile-up. For 4 MeV $< E_\gamma \leq 8.5$ MeV, the following in-beam γ-lines are evident [34]:

- the 4.4 MeV γ-ray produced by the de-excitation of the first excited state of the ^{12}C. This line is produced by the ^{11}B(p,γ)^{12}C, which is the main source of the beam induced background and by the ^{15}N(p,$\alpha\gamma$)^{12}C. The line is well visible in all nitrogen spectra and in some of the helium spectra (in the case of the ^{11}B(p,γ)^{12}C reaction the 4.4 MeV γ-ray is summed in the peak due to the transition to the ground state),

- around 5.5 MeV there is a peak due to the ^{2}H(p,γ)^{3}He reaction (visible only for $E_p \geq$ 180 keV in the helium spectra),

- the 6.1 MeV γ-ray from the decay of the second excited state of the ^{16}O populated in the ^{19}F(p,$\alpha\gamma$)^{16}O reaction (visible only for $E_p \geq 180$ keV in the helium spectra),

- the 6.2 MeV and 6.8 MeV secondary γ-rays and the ~7.5 MeV summing peak from the ^{14}N(p,γ)^{15}O reaction (well visible in all nitrogen spectra, not visible in the helium spectra),

- the ~7.7 MeV peak from the ^{13}C(p,γ)^{14}N reaction (well visible in the helium spectra, covered by the ^{14}N(p,γ)^{15}O lines in the nitrogen spectra) and

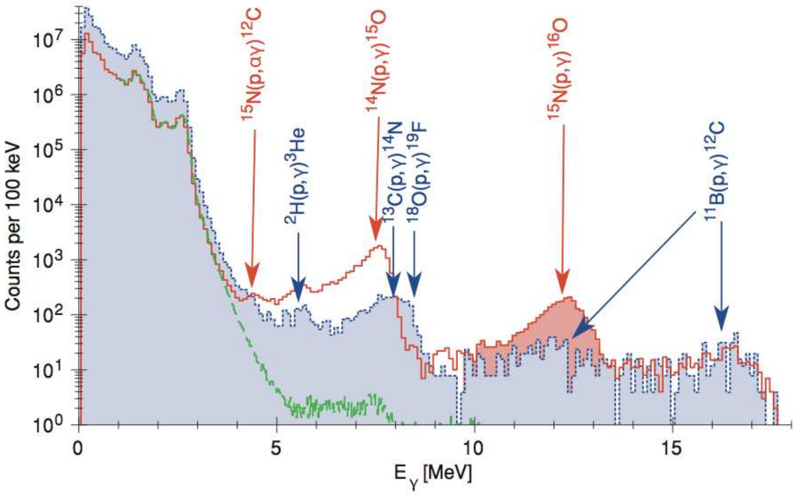

Figure 3.11: *The γ-ray spectrum, E_{beam} = 220 keV. Solid red (dotted blu) line: the nitrogen gas in the target (helium gas, rescaled to match the nitrogen spectrum in the 14.4-18.0 MeV region). Dashed green line, laboratory background, rescaled for equal live-time. This figure has been taken from Bemmerer, Caciolli* et al.*[33].*

- the 8.1 MeV summing peak from the ^{18}O(p,γ)^{19}F reaction (visible only in a few helium spectra)

At higher γ-ray energies in the spectrum, above 8.5 MeV, the contribution from the natural background is totally negligible for the purposes of the present study (Fig. 3.11). This region of the γ-ray spectrum is dominated by only two reaction:

- The ^{15}N(p,γ)^{16}O produces a γ-ray with an energy $E_\gamma = Q + E_{beam} \approx$ 12.3 MeV. This peak is visible only in the spectra with nitrogen gas in the target chamber. The resolution of the BGO detector in this range of energy is quite high and a region of interest (ROI) from 9.7 to 13.5 MeV has been adopted. For this ROI the efficiency evaluated by the simulation is 77%.

- The second reaction is the ^{11}B(p,γ)^{12}C that is the unique source of beam induced background. Since the boron was present on the collimator (see section 3.3) the peaks from this reaction are visible in both the nitrogen spectra and in the helium spectra. The ^{11}B(p,γ)^{12}C reaction produces two γ-rays in this part of the spectrum: a summing peak at $E_\gamma = Q + E_{beam} \approx$ 16 MeV (Q = 15.957 MeV) and the primary ($E_\gamma \approx$ 12 MeV) γ-ray from capture to the 4.439 MeV first excited state in ^{12}C (The decay of that state has been previously discussed).

Other sources of beam induced background were investigated in the γ-ray spectra at high energies. In example the ^{7}Li(p,γ)^{8}Be reaction has a Q-value of 17.26 MeV, but no γ-rays have been found.

3.5.1 Spectra analysis and ^{11}B background subtraction

In this section the analysis of the spectra is discussed and in particular the method of the beam induced background subtraction will be described in details.

The spectra were calibrated using the two lines of the laboratory background (^{40}K and ^{208}Tl) and the peak at the energy near 12 MeV (Fig. 3.12). In the spectra taken with helium this peak is situated at $E_\gamma = (15.957 - 4.439)\,\mathrm{MeV} + E_{CM}^{p+^{11}\mathrm{B}}$ (transition to the first excited state of ^{12}C). In the spectra taken with nitrogen it was $E_\gamma = 12.127\,\mathrm{MeV} + E_{CM}^{p+^{15}\mathrm{N}}$. The peak position has been evaluated using a Gaussian fit. In Fig. 3.12 the three peaks used in the calibration are shown. The precision of the calibration has been checked with the ^{11}B(p,γ)^{12}C peak at 16 MeV.

A quadratic calibration was used on the three peaks in order to take into account the well-known nonlinearity of the BGO detector / photomultiplier system. As previously mentioned the calibration has been validated checking the position of the peak around 16 MeV produced in the interaction of the proton on boron. A linear calibration was also tried in order to do another check of the reliability of the quadratic one and we found the same results for the counts in the selected region of interest (ROI).

In some spectra acquired at low energies the statistic in the peak at E_γ = 12 MeV was not enough to distinguish the peak position. In that cases we used the calibration of spectra taken immediately before or immediately after where the natural background lines were situated at the same position (Fig. 3.13).

Every peak was integrated in two regions of interest, called ROI_1 and ROI_2. ROI_1 has a range from 9.7 to 13.5 MeV, and ROI_2 from 14.4 to 18 MeV. In ROI_1 there are the events

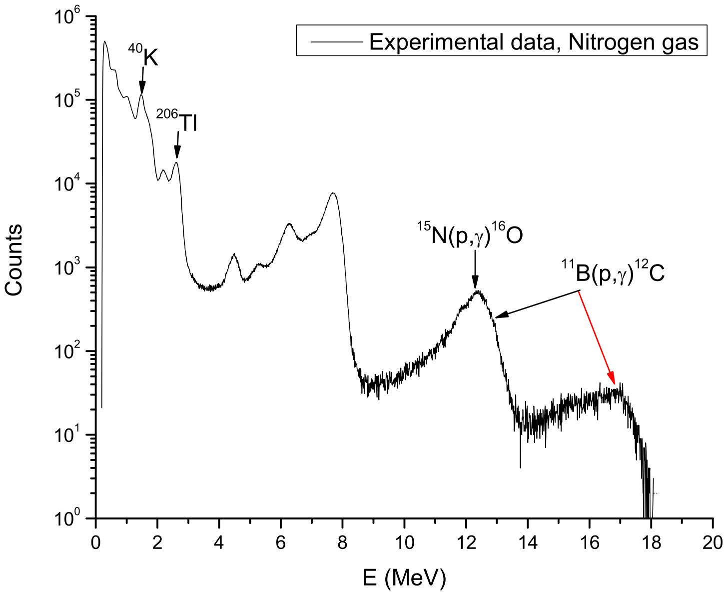

Figure 3.12: *γ-ray spectrum, E_p = 250 keV. The peaks used for the calibration (black) and the peak at 16 MeV (red) are pointed by arrows.*

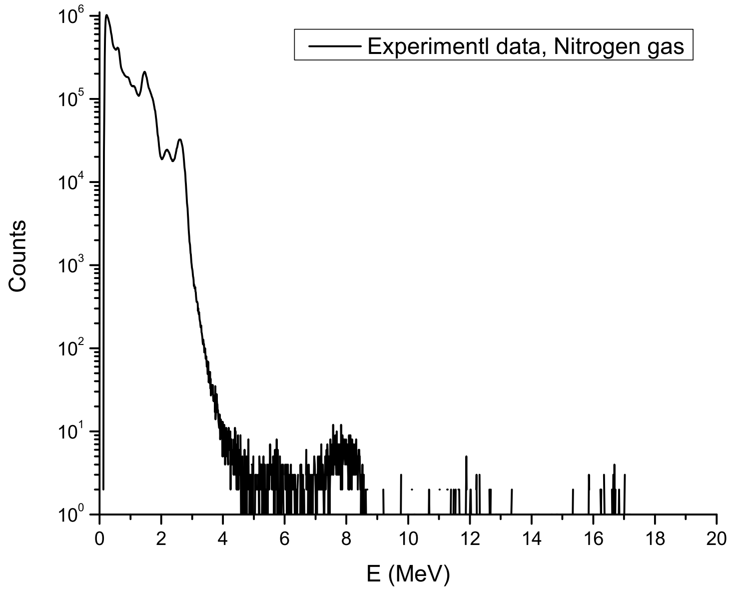

Figure 3.13: *γ-ray spectrum, E_p = 150 keV.*

produced by the ^{15}N(p,γ)^{16}O reaction and those produced by the ^{11}B(p,γ)^{12}C. In ROI$_2$ are only the events produced by the reaction on ^{11}B. The two ROIs are shown in Fig. 3.14. In this figure also the laboratory background normalized to the lifetime of the nitrogen spectrum is displayed. This latter contribution is negligible. In some cases a different calibration for nitrogen and helium spectra was noticed. Maybe it was due to the problems of fitting the peak (containing both the contribution of boron and nitrogen) with a gaussian function. So the integration method was used in both type of spectra maintaining the calibrations obtained from helium spectra and nitrogen spectra. The obtained net counts, for the ^{15}N(p,γ)^{16}O reaction, with these two types of calibrations and also, using a third method, calibrating with the peak expected at energies around 16 MeV (this third method was applied only to a few selected spectra), were consistent within the statistical uncertainty. This shows the robustness of the present method.

The ratio between the two ROIs $\beta = \left(\frac{ROI_1}{ROI_2}\right)$ was calculated for each helium spectrum. The $\beta(E_{beam})$ factor for each proton energy was calculated averaging all the β values of all the spectra at the same energy. We used the statistic uncertainty for all β values we obtained. Fixed an energy, all the β values measured in the helium spectra were in agreement, also in the case of a run acquired with a different pressure with respect to the normal pressure of 1 mbar. This is an indication that the boron position is on the last collimator, as it has been assumed in this analysis. An extended discussion about the boron position on the collimator will be presented in the next sections (especially in section 3.7), because this is an important point of the analysis.

Since the boron was localized on the collimator, the β value depends only on the energy of the beam. Fixed the energy beam the β_E factor for each proton energy was calculated

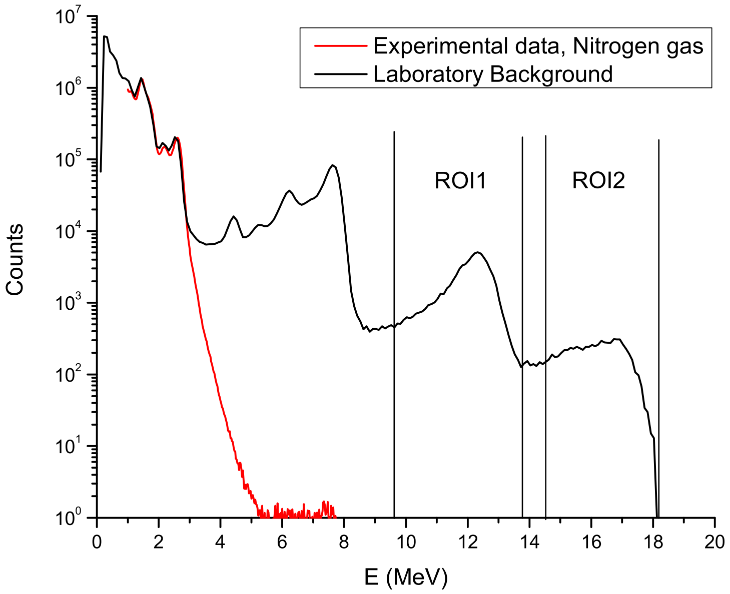

Figure 3.14: *γ-ray spectrum, E_p = 250 keV (black line) and laboratory background normalized to the lifetime (red line). The two ROIs are indicated.*

averaging all the β values at the same energy measured from the single spectrum (obviously after checking that all results were consistent within one standard deviation). Since the nitrogen spectra acquired with a gas pressure different from 1 mbar were not used in the analysis, also in the case of helium was adopted the same decision. β was multiplied by the ROI_2 in the nitrogen spectrum in order to deduce the value of the boron beam induced background, BKG, as in the following equation:

$$BKG = ROI_2^{N_2}\frac{ROI_1^{He}}{ROI_2^{He}} = ROI_2^{N_2}\beta_E \tag{3.7}$$

The BKG counts were subtracted from ROI_1 in order to know the net counts due only to the ^{15}N(p,γ)^{16}O reaction. If we divide the net counts in $ROI_1^{N_2}$ by the integrated charge during the run, this leads to the reaction yield at the selected energy.

The yield, Y, was calculated using eq. (3.8), where C is the integrated charge, for each nitrogen spectrum at the same energy:

$$Y = \frac{ROI1_{N2} - BKG}{C} \tag{3.8}$$

Then the weighted average of these values was used in order to obtain an unique value for the yield. Using reasonable choices for angular distribution [35, 36], angular correlation [37] and branching ratios [35] based mainly on the values at the E_{beam} = 163 keV resonance (outside this resonance there is only limited data in the literature) values $\beta = \left(\frac{ROI_1}{ROI_2}\right) =$ 1.5 – 3.0 have been obtained in the simulation, consistent with the data. The $\beta = \left(\frac{ROI_1}{ROI_2}\right)$

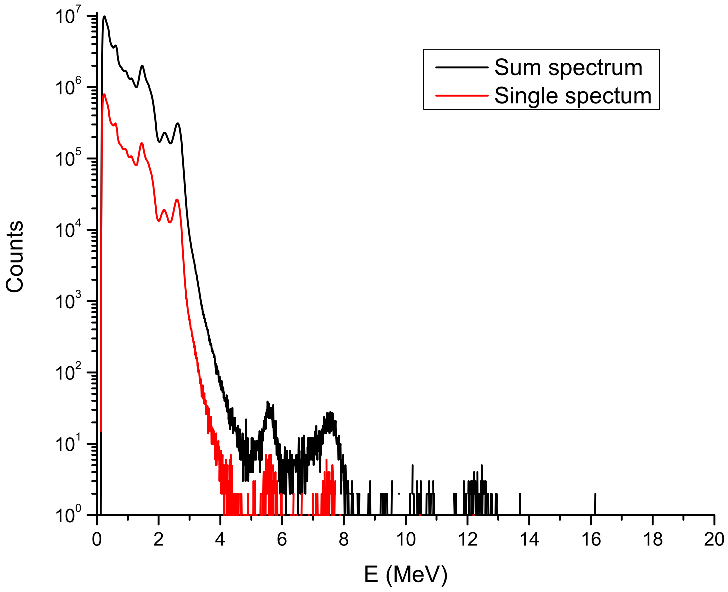

Figure 3.15: *γ-ray spectrum, E_p = 100 keV.The sum of all spectra at this energy is shown in black and the contribution from only one spectrum is given in red.*

values given by the experiment have been used in all cases in order to make the ^{15}N(p,γ)^{16}O result independent from the theory-based assumptions on the ^{11}B angular distribution and angular correlation and to improve the precision.

At the energy E_p = 120 and 100 keV we analyzed the sum of the nitrogen spectra all together. We did the same for the helium spectra, because it was impossible to distinguish any structure in single spectrum in the two ROIs, and so it was not possible to proceed with a calibration Fig. 3.15. The spectra where the pressure of the gas was not equal to 1 mbar or when some problems occurred during the measurement (accelerator sparks, current to much variable, etc.) were not analyzed. Only in the case of the nitrogen spectrum at E_p = 180 keV two spectra acquired at 0.5 mbar pressure were implemented in the analysis, because at 1 mbar pressure the γ-ray due to the ^{11}B reaction overwhelmed the signal from the ^{15}N(p,γ)^{16}O. As a matter of fact in that run the beam hit a lot the collimator where the boron was located (see Fig. 3.16).

In addiction, the runs where the ratio $\frac{ROI_1^{N_2}-BKG}{BKG}$ was below 1 (signal over background below 1) were not used in the analysis (especially at low energy and around E_{beam} = 163 keV). As a matter of fact the counts due to the ^{15}N(p,γ)^{16}O were lower than the counts due to ^{11}B(p,γ)^{12}C.

3.6 Experimental upper limits on possible cascade transitions

The BGO efficiency depends also on the decay scheme and on the angular distribution of the emitted γ-radiation (see section 3.4.5). Few measurements of this parameters for the

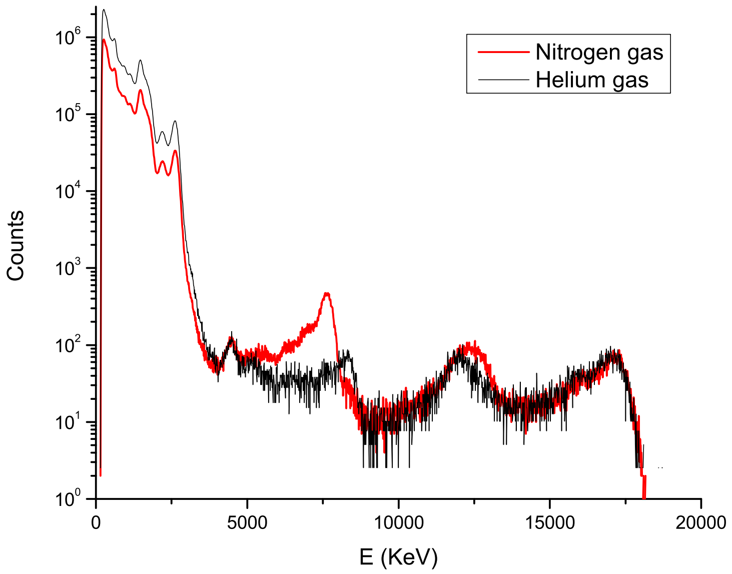

Figure 3.16: *γ-ray spectrum, E_p = 180 keV, the spectrum with helium gas has been scaled up to match the nitrogen spectrum in the 14.4 - 18 MeV region.*

^{15}N(p,γ)^{16}O reaction has been done [14, 32] and only at selected energies. At low energies, dedicated runs were performed at the LUNA accelerator with two different setups in order to obtain an upper-limit of the cascade transition contribution.

3.6.1 Runs with an HPGe detector and the present gas target setup

The first runs analyzed for the evaluation of the cascade contribution were taken with the same setup already used for the boron studies (section 3.3).

In these spectra the primary γ-rays from capture into the states at 7.117 and 6.049 MeV and the 7.117 MeV secondary γ-ray were searched. Because the statistics was too low, only the spectra at E_p = 200 keV were analyzed. The spectra had the same calibration so it was possible to sum them all. The resulting spectrum is plotted in Fig. 3.17. Two possible cascades were studied. The former proceeds to the excited state with energy E_X = 7.117 MeV, and the latter to the 6.049 MeV state. For the second cascade it was possible only to analyze the primary γ-ray, because the γ-transition to the ground state of ^{16}O is forbidden.

In the 200 keV spectrum there are some background lines at the same energy as the two primary γ-rays, so only the region where the secondary is expected was analyzed. Fig. 3.18 shows in details this energy in the spectrum. Clearly it is not possible to distinguish any structure at the place where the peak should be found. In order to give an upper limit to the peak the spectrum was integrated in a region around the γ-ray energy as large as for the other peaks. The background was subtracted using a linear interpolation between two regions immediately nearby. The two background regions have to be at the same distance from the peak region and they should be of the same width. Using eq. (3.9) [38] a 2σ upper limit for the peak counts was calculated:

$$L^{up} = N + 1.645\sqrt{N + 2B} \tag{3.9}$$

where N is the net counts in the peak (if the net counts are negative a values of zero was used) and B the background under the peak. The upper limit cross section σ^{up} was obtained normalizing to the known ^{14}N(p,γ)^{15}O cross section for the 6.79 MeV line [2] (also integrated in the experimental spectrum) and correcting for the different isotopic abundance of ^{14}N and ^{15}N. The change of the detection efficiency between 6.8 and 7.1 MeV was neglected for this purpose.

In conclusion, a 6% upper limit was obtained for capture to the 7.117 MeV state. Using the known 27% reduction in detection efficiency for this transition (sec. 3.4.5), this gives 1.6% systematic uncertainty in the final ^{15}N(p,γ)^{16}O cross section due to a possible cascade transition.

3.6.2 Runs using a Clover germanium detector and solid targets

The Clover spectra taken at E_p = 400 keV have been analyzed, looking for the primary γ-rays from capture into the states at 7.118 and 6.049 MeV. The 7.118 MeV secondary γ-ray was masked by a γ-ray from the ^{19}F(p,$\alpha\gamma$)^{16}O reaction. This fluorine contribution was not present in the gas target experiment. This experimental setup is described in [5]. Briefly it consists in a clover germanium detector placed in close geometry with a solid target of titanium nitride. The target was made using natural nitrogen.

Upper limits of 1.9% for the primary to the 7.118 state and 1.8% for the primary to the

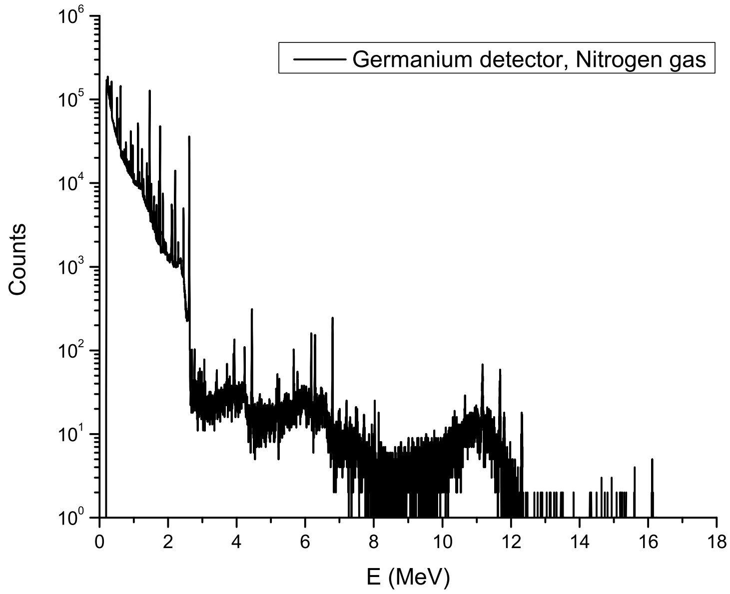

Figure 3.17: *γ-ray spectrum, E_p = 200 keV, 1 mbar nitrogen in the gas target, germanium detector.*

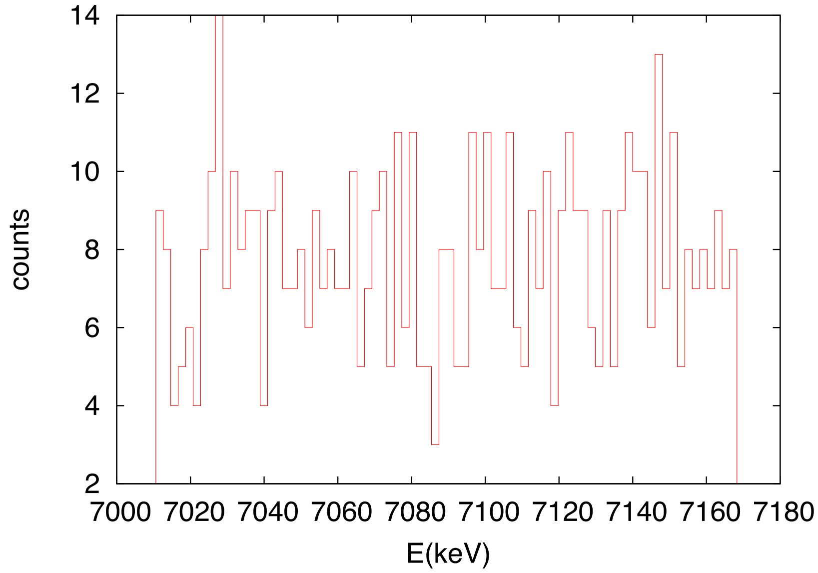

Figure 3.18: *γ-ray spectrum, E_p = 200 keV, germanium detector, detail of the region near 7.1 MeV.*

6.049 MeV state have been obtained. The effective energy for these spectra is still higher than the peak of the wide E_{beam} = 335 keV resonance. However, the present upper limit is consistent with the reported [32] 1.2% branching for decay of the 335 keV resonance to the 6.049 MeV state.

3.7 Localization of the ^{11}B contaminant and the GEANT4 simulation code

In previous sections the assumption of the boron localization on the last collimator, at the entrance of the target chamber, has been done. In this assumption the interacting proton energy on boron is not dependent on the type of gas in the chamber. As a consequence we can compare the nitrogen and helium spectra acquired at the same beam energy. The other possibility was that the boron was deposited on the calorimeter. In that case, due to the different stopping power of the two gases (helium and nitrogen), at the proton beam energy at the calorimeter depends on the filling gas.

The boron was localized using the Doppler shift technique with the setup described in section 3.3 and the results of this analysis have already been published [34].

A further check has been done in order to verify the position of the ^{11}B by comparing the experimental β values with GEANT4 simulations. The simulation has been carried out under the two different possible positions of the boron:

1. The ^{11}B is located at the final collimator [34].
2. The ^{11}B is located at the beam-stop. In this case β is expected to be much smaller, because of the increased summing probability.

For each of two cases, two different angular distributions have been adopted:

A The angular distribution [35, 36] and correlation [37] are the same as on the E_{beam} = 163 keV resonance

B Assume isotropic angular distribution and no angular correlation.

In this way four simulations were carried out: Sim1A, Sim2A, Sim1B and Sim2B. The branching ratios used in the simulation are the ones reported in [35]. The simulated spectrum for Sim1A is shown in Fig. 3.19 superimposed with the experimental spectrum. The two spectra are in good agreement. For all the four simulations the value of the β ratio has been calculated and shown in Fig. 3.20. As expected the simulation 2 gives a smaller β value than the one in simulation 1 due to an higher summing effect.

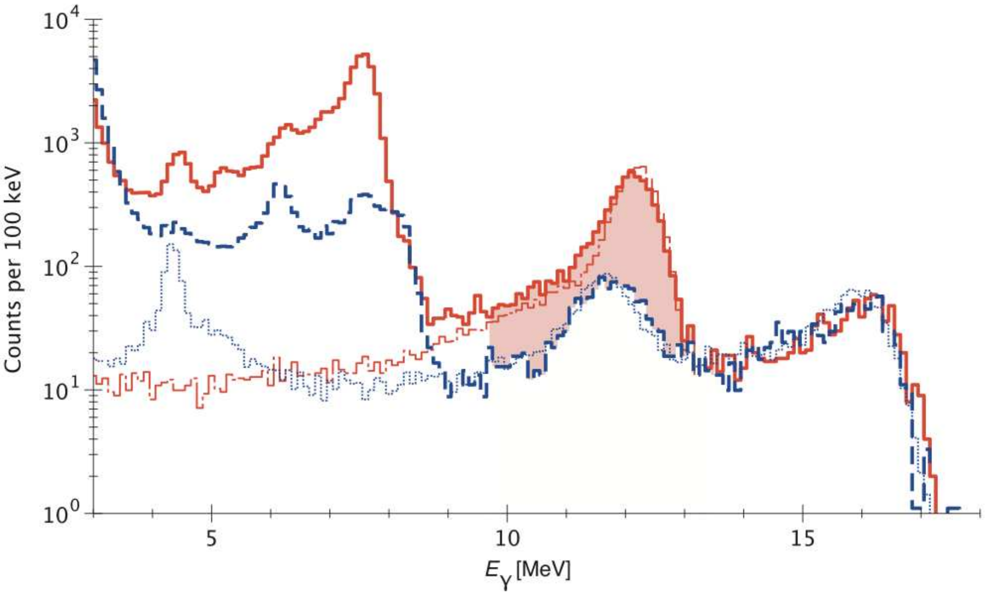

Figure 3.19: *The γ-ray spectrum, E_{beam} = 220 keV. Red solid (dot dashed) line: experimental, nitrogen gas (simulated, assuming only the ^{15}(p,γ)^{16}O reaction). Blue dashed (dotted) line: experimental, helium gas, rescaled as in Fig. 3.11 (simulated with Sim 1B, assuming only the ^{11}B(p,γ)^{12}C reaction.This figure has been taken from Bemmerer, Caciolli* et al.*[33].*

In Fig. 3.20 the experimental values of β are plotted together with the simulated points in the four configurations. The comparison of the data and the simulations shows that none of the twelve data points is consistent with the assumption 2 (boron on calorimeter). Instead, all data points are consistent with assumption 1.

Since the experimental uncertainty on the factor β is quite high, it was impossible to exclude totally configuration 2. It seems plausible that given the limited input data (the simulation strongly depends on the value of angular distribution and correlation) the simulation does a better job close to E_{beam} = 163 keV than far away at lower and higher proton beam energies. A conservative final uncertainty on the β_E factor has been adopted. For $\Delta\beta_E$ either the statistical uncertainty or ±1.0 (an upper limit on the full difference between the four simulations) is used, whichever is greater. In table 3.2 all the numbers for the boron subtraction have been reported.

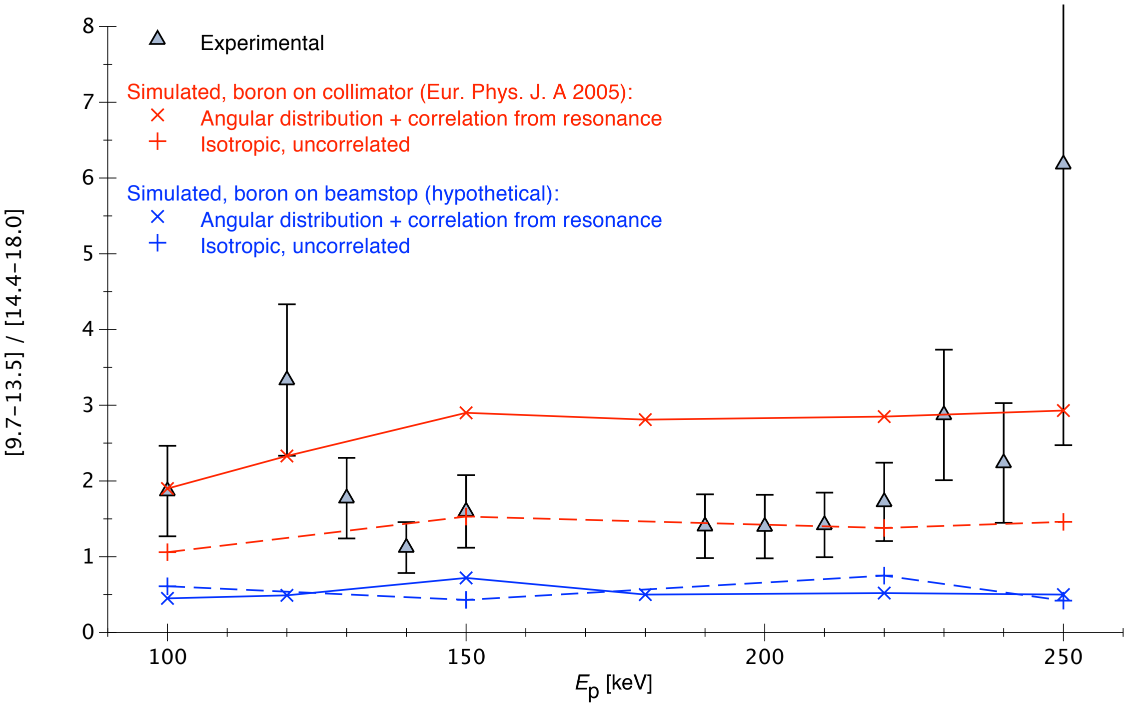

Figure 3.20: *$\beta(E_{beam})$: ratio of counts in the regions ROI$_1$ (9.7-13.5 MeV) and ROI$_2$ (14.4-18.0 MeV). Plotted are the experimental $\beta(E_{beam})$ data points that were also used for the final data analysis. The curves are from GEANT4 simulations. See text for details.*

	Raw counts		β				Boron background	Net counts		
E_{beam}	ROI$_1$	ROI$_2$	Experiment	Sim. 1	Sim. 2	Adopted	ROI$_1$	ROI$_1$	Δ_{stat}	Δ_{Boron}
101	293	69	1.9±0.6	0.70	1.13	1.9±1.0	130±70	164	10%	43%
122	355	31	3.3±1.0	0.75	1.37	3.3±1.0	100±40	252	7%	14%
131	662	79	1.8±0.5	0.77	1.33	1.8±1.0	140±80	522	5%	15%
141	1703	172	1.1±0.2	0.80	1.44	1.1±1.0	190±170	1510	3%	11%
151	2739	433	1.6±0.2	0.80	1.46	1.6±1.0	700±400	2047	3%	21%
188	12126	2895	1.4±0.3	0.81	1.46	1.4±1.0	4100±2900	8064	1%	36%
201	1300	222	1.4±0.05	0.84	1.52	1.4±1.0	310±220	990	4%	22%
210	32569	3836	1.42±0.03	0.80	1.49	1.4±1.0	5400±3800	27120	1%	14%
221	6360	902	1.72±0.07	0.78	1.46	1.7±1.0	1600±900	4805	2%	19%
229	1930	98	2.9±0.2	0.80	1.43	2.9±1.0	280±100	1649	3%	6%
238	1517	33	2.2±0.8	0.77	1.51	2.2±1.0	70±40	1443	3%	2%
250	958	18	6±4	0.81	1.38	6±4	110±70	847	4%	8%

Table 3.2: *Spectrum integration and background subtraction. The raw counts in the ROI$_1$ and in the background monitoring region (ROI$_2$) are given. For the ratio β, the experimental data are from runs with helium gas in the target. The simulation 1 and 2 and the adopted uncertainty are explained in the text. The boron background in the ROI$_1$ (column 8) is obtained by multiplying columns 3 and 7. The net counts in the peak (column 9) are obtained by subtracting column 8 from column 2.*

3.8 Data Analysis

The yield,Y, depends directly on the pressure profile and the efficiency. It is also proportional to the cross section. Since σ depends on the beam energy we have to take into account the beam energy loss into the target. The yield should be written as:

$$\begin{aligned} Y &= \frac{N_\gamma}{N_p} = && (3.10)\\ &= \int_{x_0}^{x_{max}} n_{target}(x)\cdot\sigma(E_{beam}(x))\cdot\eta(E_{beam}(x),x)\mathrm{d}x && (3.11)\end{aligned}$$

where

- N_γ is the the net number of γ-rays in the region of interest, after the boron subtraction,
- N_p is the number of incident proton evaluated by the calorimeter method (sec.),
- $n_{target}(x)$ is the target density where we have already taken in account the effect of the beam heating,
- $\sigma(E_{beam}(x))$ is the reaction cross section. Due to the stopping power (calculated by SRIM [23]) the energy depends on the position x, which is the coordinate along the beam axis,
- $\eta(E_{beam})$ is the detection efficiency, evaluated with the simulation (sec. 3.4).

The cross section can be written in term of the S-factor, $S(E)$, and the Coulomb barrier:

$$\sigma(E_{beam}(x)) = S(E)\frac{1}{\frac{m_{15}}{m_p+m_{15}}E_{beam}(x)}\exp\left(-2\pi\cdot 7\cdot\alpha\cdot\sqrt{\frac{m_pc^2}{2E_{beam}(x)}}\right) \tag{3.12}$$

where m_p and m_{15} are the mass of proton and of ^{15}N, respectively, c the vacuum speed of light, $E = \frac{m_{15}}{m_p+m_{15}}E_{beam}(x)$ the center of mass energy, $\alpha = \frac{2\pi q_e^2}{hc}$ the fine structure constant. The exponential function gives the tunnel probability through the Coulomb barrier for incident s-wave protons.

The reference density, n_0, without beam heating correction has been calculated for the condition of p_{T0} = 1 mbar and T = 306 K using the atomic mass, taking into account the 0.366% isotopic abundances of ^{15}N.

For simplicity we introduce two abbreviations, $\epsilon(E_{lab}(x))$ and $\kappa(x, E_{beam}(x), n_{target})$:

$$\begin{aligned} \epsilon(E_{beam}(x)) &\equiv \frac{1}{\frac{m_{15}}{m_p+m_{15}}E_{beam}(x)}\exp\left(-2\pi\cdot 7\cdot\alpha\cdot\sqrt{\frac{m_pc^2}{2E_{beam}(x)}}\right) && (3.13)\\ \kappa(x,E_{beam}(x),n_{target}) &= \frac{n_{target}(x)}{n_0}\cdot\eta(E_{lab}(x),x)\cdot\epsilon(E_{beam}(x)) && (3.14)\end{aligned}$$

The energy E_{beam} has been calculated using the energy loss $\frac{dE}{d\tilde{x}}(E_{beam}(\hat{x}))$ in units of $\frac{\mathrm{eV}}{10^{15}\frac{\mathrm{atoms}}{\mathrm{cm}^2}}$ from [23]. The resulting integral is evaluated numerically in small steps x_i:

$$\begin{aligned} E_{beam}(x) &= E_p - \int_{\hat{x}=0}^{\hat{x}=x} \frac{dE}{d\tilde{x}}(E_{beam}(\hat{x})) \cdot n_{target} & (3.15) \\ E_{beam}(x_i) &= E_{beam}(x_{i-1}) - \frac{dE}{d\tilde{x}}(E_{beam}(x_{i-1}) \cdot (x_i - x_{i-1}) & (3.16) \end{aligned}$$

Assuming a constant S-factor over the energy range given by the energy loss inside the target, equation (3.10) becomes:

$$Y = S(E) \cdot n_0 \cdot \int_{x_0}^{x_{max}} \kappa(x, E_{beam}(x), n_{target}) \mathrm{d}x \tag{3.17}$$

The astrophysical S-factor can finally be obtained from the experimentally determined yield and the integral over κ:

$$S(E) = \frac{Y = \frac{N_\gamma}{N_p}}{n_0 \cdot \int_{x_0}^{x_{max}} \kappa(x, E_{beam}(x), n_{target}) \mathrm{d}x} \tag{3.18}$$

If as $\eta(x)$ a pressure profile as in [39] were adopted then the final S(E) changes by 0.6%.

The proton energy has to be weighted by the coefficient κ in order to calculate the effective energy $E_{eff,beam}$. It is derived as follow:

$$E_{eff,beam} = \frac{\int_{x_0}^{x_{max}} \kappa(x, E_{beam}(x), n_{target}) \cdot E_{beam}(x) \mathrm{d}x}{\int_{x_0}^{x_{max}} \kappa(x, E_{beam}(x), n_{target}) \mathrm{d}x} \tag{3.19}$$

3.9 Astrophysical S-factors

The astrophysical S-factor from this analysis is shown in Fig. 3.21 and the values reported in table 3.4.

The statistical uncertainties are due to the peak integration and the charge. The first contribution is Poisson distributed and it plays an important role also in the background subtraction (i.e. if the background contribution in the ROI_1 was higher than the resulting net counts after subtraction we decided to not use the run). The number of incident proton is calculated according to equation (2.3). The target density, n_{target}, depends from the pressure measurement p_T. This is quoted with 0.1% uncertainty which is negligible in comparison with the other sources of statistical uncertainty.

Most of the systematic uncertainties (table 3.3) were discussed in previous sections of this work and in previous papers [3, 4]. The last uncertainty we have to take in account is the energy calibration. It introduces errors $\Delta_{stat}E_p$ and $\Delta_{syst}E_p$ that are shown in table 3.3.

As shown in Fig. 3.21 the LUNA gas target results [33] are lower than the previous data [14]. Our data are still in agreement with both the previous direct measurements at 2σ level given the previous high uncertainties. In the limited overlapping energy region,

Source of uncertainty	Details found in	Effect on S-factor
Target density	[3]	3.2%
^{15}N isotopic ratio	[25, 26]	3.0%
Beam intensity	[24, 3]	1.0%
Effective energy	[20]	3.0%
γ-ray detection efficiency	Section 2.4	3.0 %
γ-ray capture to excited states	Section 2.4	1.9%
γ-ray angular distribution	Section 2.4	4.0%
^{11}B(p,γ)^{12}C background	Section 3.5.1	1.8% - 43%
Total systematic uncertainty		8% - 44%

Table 3.3: *Systematic uncertainties and their effect on the S-factor value.*

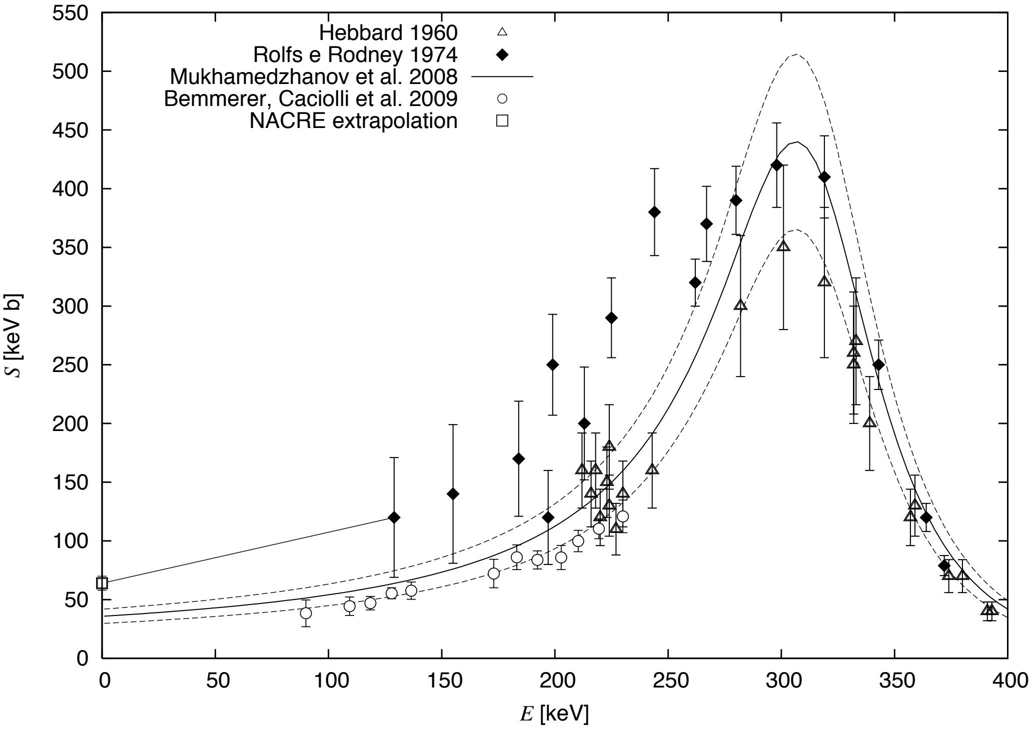

Figure 3.21: *Astrophysical S-factor for the ^{15}N(p,γ)^{16}O reaction as as function of the center of mass energy. The LUNA gas target are presented (circles) with data from Hebbard [13] (triangle) and from Rolfs and Rodney [14] (black diamonds). The curve represents the R-matrix fit from the ANC data [15] with the quoted errors (dashed curves). The NACRE extrapolation is also reported.*

		$\Delta S/S$		
E_{eff} (keV)	S(E_{eff}) (keV barn)	Statistical	Total systematic	Systematic (boron)
90.0	38.4	14%	44%	43%
109.3	44.4	11%	16%	14%
118.5	47.0	6%	17%	15%
127.9	55.4	3%	13%	11%
136.6	57.6	4%	22%	21%
173.0	72.2	2%	37%	36%
183.2	86.1	4%	24%	22%
192.3	83.8	1%	16%	14%
202.8	85.9	2%	20%	19%
210.3	99.9	3%	9%	6%
219.4	110.4	3%	7%	2%
230.0	120.9	5%	11%	8%

Table 3.4: *Effective center of mass interaction energy E_{eff}, S-factor and relative uncertainties. The systematic uncertainty due to the boron background subtraction has been derived in table 3.2 and is repeated here (column 5). The boron uncertainty is already included in the total systematic uncertainty given above (column 4).*

the present data seem to agree with [13], if [13] low energy data points (affected by beam induced background) are excluded. The NACRE extrapolation [7], based on the data from Rolfs and Rodney [14], are a factor 2 higher then our results.

The LUNA gas target data are still in agreement with the indirect data published by Mukhamedzhanov [15]. They are also lower than the fit shown in [16].

The LUNA results cover almost completely the Gamow peak in novae, but not the resonance at E_R = 312 keV. The two R-matrix fits are heavily dependent on the resonance and so from the previous data that are higher than our present results. Therefore we decided to proceed with further experiment in order to cover all the LUNA2 accelerator energy range from 80 keV up to 400 keV in order to measure the resonance and to explore the energy region below E_{beam} = 100 keV (the minimum energy covered by the gas target experiment). This experiment will be discussed in the next chapter.

Chapter 4

^{15}N(p,γ)^{16}O cross section from the solid target experiment

In the previous chapter we learnt that the main problem in the analysis of the gas target experiment was the subtraction of the in-beam induced background. The lack of statistic, due to the very small content of ^{15}N in the natural nitrogen (0.366%), enhances the role of the boron contribution and prevents the analysis of some runs.

In addiction, the large amount of the ^{14}N in the gas target prevented the analysis of the spectra acquired at the energies near the the ^{14}N(p,γ)^{15}O resonance at E_{beam} = 278 keV, because of the high pile-up in the region of interest for the ^{15}N(p,γ)^{16}O reaction.

In this view we chose to perform a new experiment using targets enriched in ^{15}N (nominally at 98%) where the statistic is improved by a about factor 200 with respect the previous experiment. Since the measured yield is directly proportional to the number of active nuclei in the target, an intensive study of the target characteristics has been done (section 4.2).

The γ-rays detector is the same BGO already used in the gas target experiment. We have determined its efficiency with the same GEANT4 code (sec. 3.4) changing the geometry in order to take into account the different target chamber and the target dimension (section 4.5).

The data acquisition and analysis will be discussed in section 4.1 togeter with the new data result for the S-factor.

4.1 Data taking

We have measured spectra in an energy range from 80 keV up to 400 keV in the laboratory system using two sets of titanium nitride target for a total of 7 targets: five produced in the Forschungszentrum in Karlsruhe and two produced in Laboratori Nazionali di Legnaro (LNL). The target deterioration (sec. 4.2) should be taken in account in each day of measurements since the beam changes the targets thickness, the stoichiometry and the isotopic ratio (the problem of target deterioration will be discussed in details in section 4.2)

For the targets produced in Karlsruhe we have done a scan of the ^{14}N(p,γ)^{15}O resonance at E_{lab} = 278 keV and we acquired three runs (called "reference points") at the energy of 340, 350, and 360 keV on the broad resonance at E_{lab} = 350 keV[1] of the ^{15}N(p,γ)^{16}O. Both the resonance scan and the reference points were used in order to control the target behavior and they were done before and after each long measurement. In this work the terms long measurement refers to a run performed during the night: a time long enough in order to have a possible target thickness change. For the Legnaro targets we did not performed the scans on the resonance of the ^{14}N(p,γ)^{15}O reaction every day, but only after mounting and dismounting the targets.

In each run we collected a spectrum by saving event per event the anode signal (list mode) for each BGO crystal and also a spectrum of the summed signal acquiring the sum of all dynode signals. Each run was saved by the VME system described in section 2.4, converted to the ROOT format and finally analyzed by root macros. The sum of all dynodes was sent also to the trigger threshold in order not to acquire the γ-rays in the energy range below 0.7 MeV. In this way we reduced the dead time and the pile-up produced by this γ-rays. The threshold level did not affect the high energy region while in the low energy part of the γ-spectrum it prevented the detection of the ^{137}Cs γ-rays. As a consequence, we have modified the threshold level in order to acquire spectra with this radioactive source for calibration purposes. The possibility to have both the online sum spectrum and the list mode (that allows to reconstruct the offline sum spectrum) is a good check for the offline analysis with the root macros. The spectra were saved in root files and were analyzed in following way: the single spectra were calibrated separately using a quadratic calibration on three peaks: the one at 511 keV, the 4.4 MeV due to de-excitation of the first exited level of ^{12}C (Fig. 4.5) and the peak at E_γ = Q + E_{CM} around 12 MeV (see Fig. 4.1 and Fig. 4.2). In the case of the third peak the beam energy, E_{CM}, was corrected to take in account the energy loss in the target, but the Doppler effect and the recoil energy subtraction (eq. (3.4) and eq. (3.5)) were considered totally negligible due to the bad energy resolution of the BGO type detector. In any case a shift of 10 keV maximum (the contribution due to the stopping power on the target thickness) does not affect the final integral in the Region Of Interest (ROI). In Fig. 4.3 the three calibration peaks are shown together with the fit used to find the mean energy. The first and the second peak were analyzed with a normal gaussian fit, but for the third peak it has been necessary to implement a skewed gaussian function:

$$F(E) = A * \exp((E - E_{mean})/C) * Erfc((E - E_R)/(\sqrt{2} * B) + B/(\sqrt{2} * C)) \qquad (4.1)$$

where A, B and C are function parameters, $Erfc(x)$ is the error function and E_{mean} is the mean energy of the peak. The eq. (4.1) has been used, since the peak has a long tail on the left, because it is a primary peak and it is produced by the proton direct capture (see sec. 1.2.2). The tail on the left is due to the integration of the cross section along the energy loss ΔE into the target.

After calibration of the six spectra of the six crystals were summed on event per event

---

[1] The effective energy of the resonance in the laboratory system is E_R^{lab} = 335 keV, but the target thickness shifts the maximum in the measured yield plot to higher beam energies.

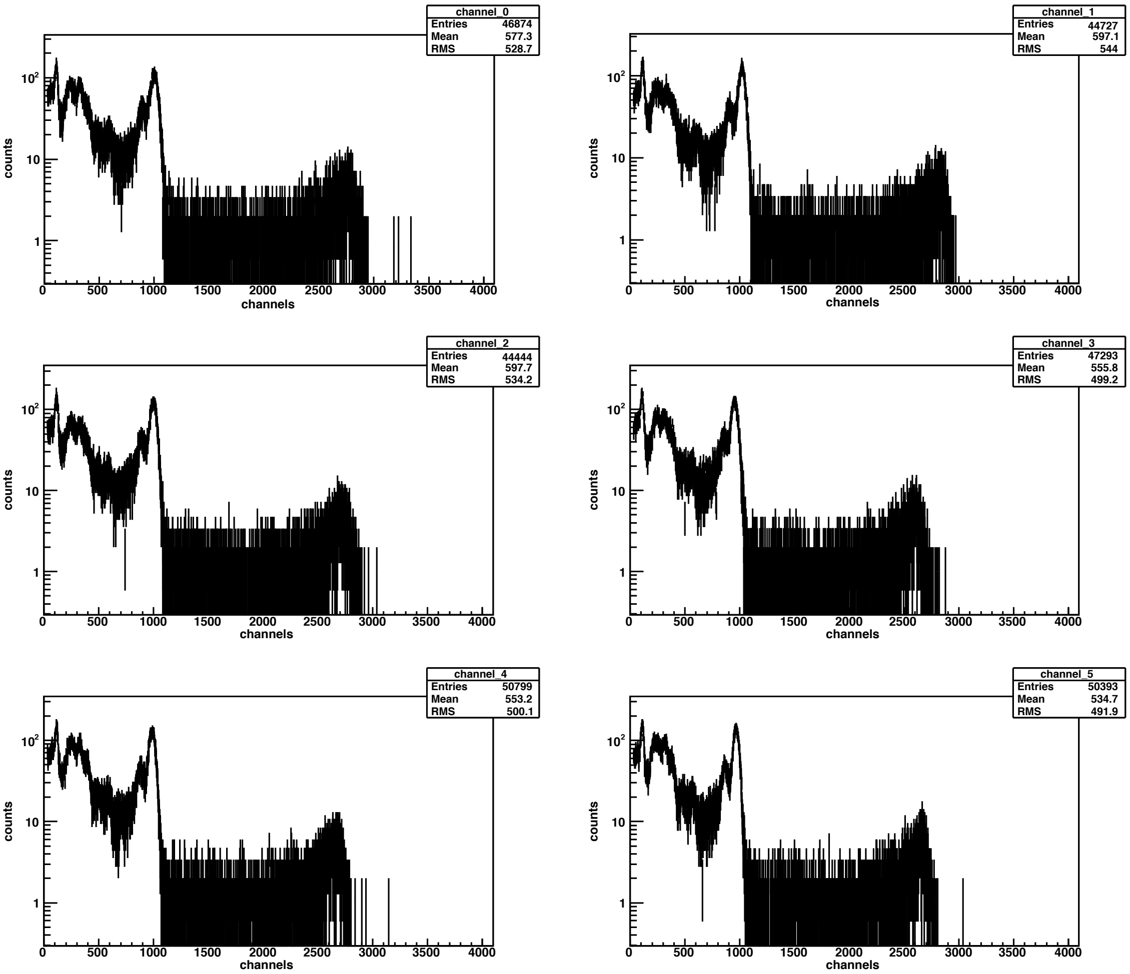

Figure 4.1: *The six raw spectra from all crystals are reported. The not perfect gain matching is evident in channel 3 and channel 5 spectra. The software sum procedure neglects totally this problem. The spectrum has been acquired on the target LNL2 at an energy of 385 keV in the laboratory system.*

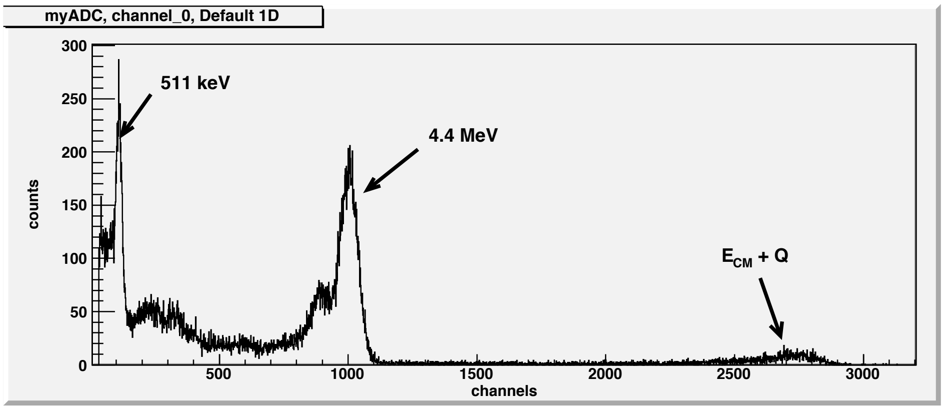

Figure 4.2: *A not calibrated single crystal spectrum acquired at* E_{beam} *= 380 keV.*

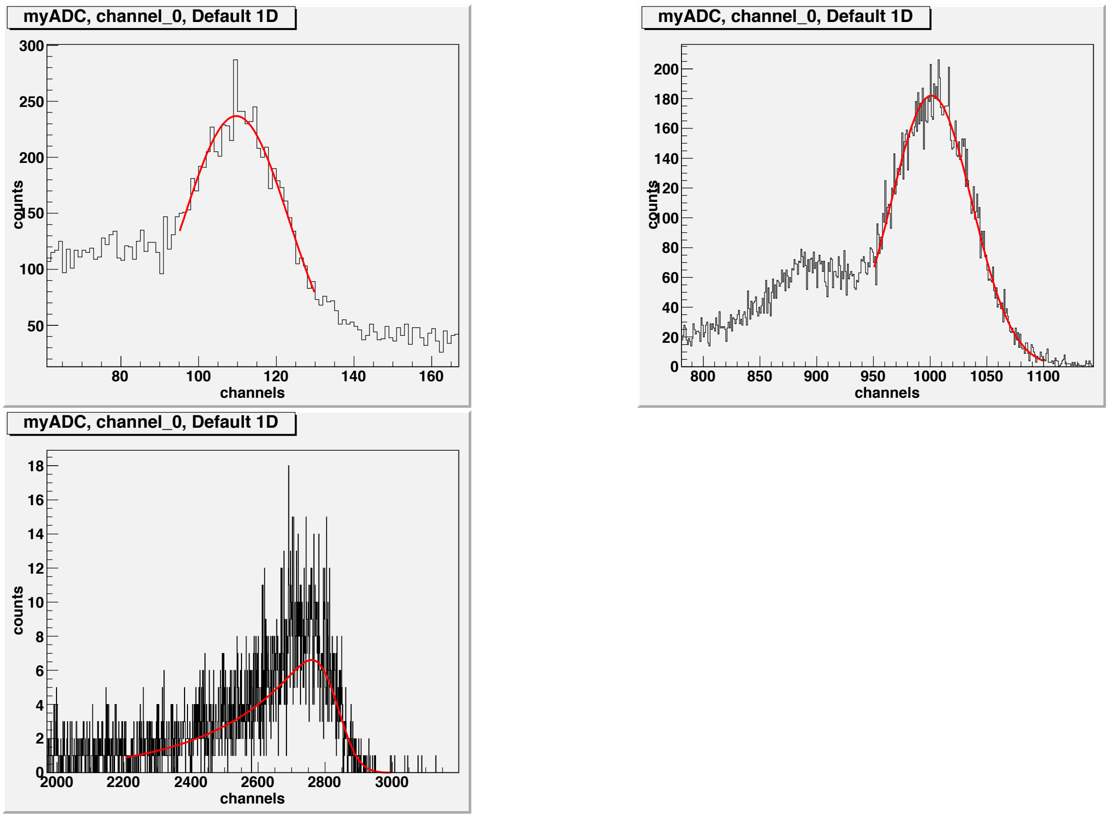

Figure 4.3: *An example of the three fits to the peaks shown in Fig. 4.2 and used in the calibration. The red curve represent the fit.*

base. In this way we were able to reconstruct the energy of a γ-ray that lost its energy in more than one crystal. Since the reaction goes directly to a de-excitation to the ground state and it produces an high energy γ-ray, the probability that a γ-ray loses energy in two or three crystals is not negligible as reported in Fig. 4.4.

Two examples of software sum spectrum are shown in Fig. 4.7 and Fig. 4.6 for an energy on the broad resonance (E_{beam} = 380 keV) and an energy below the resonance (E_{beam} = 120 keV) respectively. In the spectrum in Fig. 4.7 the peaks from the ^{14}N(p,γ)^{15}O reaction and from the ^{19}F(p,$\alpha\gamma$)^{16}O reaction are evident in the energy window from 5 to 10 MeV together with the small contamination due to the d+p reaction. At E_γ = 4.4 MeV there is the intense peak from the de-excitation of the first excited level of ^{12}C. This γ-ray is produced both by the ^{11}B(p,γ)^{12}C and the ^{15}N(p,$\alpha\gamma$)^{12}C reactions as already discussed in the analysis of the gas target setup (see sec. 3.5). At $E_\gamma > 8.5$ MeV the spectrum is dominated only by two reactions (as in the case of the gas target measurements): the full energy peak due to the transition to the ground state in the ^{15}N(p,γ)^{16}O reaction, that we are interested to study, and the peak around 16 MeV produced by the ^{11}B(p,$\alpha\gamma$)^{12}C reaction. This reaction produces also a γ-ray with an energy around 11 MeV due to the primary transition to the first exited level of ^{12}C as already explained in sec. 3.5 (In Fig. 4.5 there is the scheme levels of ^{12}C related to the direct capture ^{11}B(p,γ)^{12}C reaction). This 11 MeV γ-ray is placed in the same energy region where there is also the peak produced by the ^{15}N(p,γ)^{16}O reaction of our interest and it is

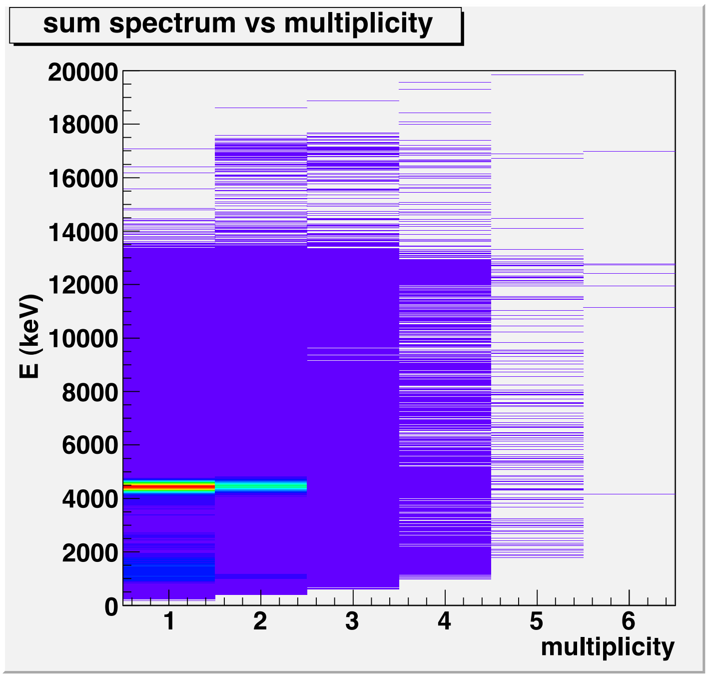

Figure 4.4: *Multiplicity spectrum. The multiplicity represents the numbers of crystals where the γ-ray energy has been lost.*

impossible to decouple the two.

In the gas target experiment we acquired spectra with helium in the target chamber and we derived the ratio of the counts in the peak at 12 MeV and the peak at 16 MeV in order to subtract the boron contribution. In solid target experiment no monitor spectra has been acquired, but we measured the boron resonance at E_R = 163 keV for efficiency calculation. Analyzing the spectrum of proton on boron targets ($LiBO_2$ produced by ATOMKI in Debrecen) the ratio β (see sec. 3.5.1 for the definition) has been measured to be always close to 0.5 (other details on the boron spectra are in sec. 4.5 where the efficiency of the detector has been discussed in comparison with the measurement on the $LiBO_2$ target). This is due to the target position at the center of the target chamber that enhances the summing effect. This value for β means that the boron contribution measured in the region from 14-18 MeV in the γ-ray spectrum (ROI_2) is quite the double of the one present in the region of interest for the ^{15}N(p,γ)^{16}O reaction (ROI_1)[2]. It was decided to exclude from the analysis the spectra when the boron counts in the ROI_2 were more than the 3% of the raw counts in ROI_1. In this case we are sure that the boron contribution should be lower than the 3%, also in ROI_1. This value is lower than the other contributions to the systematic uncertainty. The spectrum at energies below 3 MeV is dominated by the natural background, which in contrary is negligible at high energies. The peaks from ^{40}K and ^{208}Tl are evident. In the γ-ray energy region below 700 keV the spectrum is cut by the trigger threshold. The cut due to the trigger threshold is evident only in the summed spectrum and not in the single one, because

---

[2] A precise definition of the two ROIs is in section 4.6 where the procedures to calculate the S-factor are described.

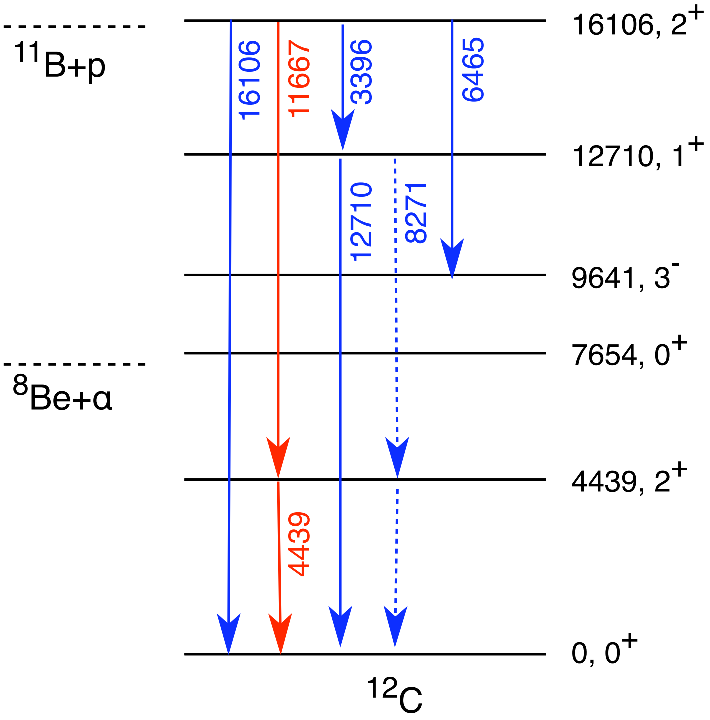

Figure 4.5: *Level scheme of* ^{12}*C from ENSDF database [40], the levels and transitions important for the* E_{beam} *= 163 keV resonance in* ^{11}*B(p,*γ*)*^{12}*C (*E_X *= 16106 keV in* ^{12}*C) are highlighted. The main* γ*-rays found in the spectrum are shown as arrows. The two* γ*-rays used for the efficiency calibration is shown in red.*

the threshold has been set only in the module that produce the trigger and not in the ADCs connected to the single crystals (there is also a threshold in each ADC but it is too low to affect the γ spectrum shape). Since the region of interest is at high energies this cut did not affect the measurements, but it reduced the dead time and the pile up at low energies where the events are mainly from the natural background.

4.2 Target production and analysis

In the solid target phase two sets of targets were used. The former set was made in the Forschungszentrum Karlsruhe and the latter in the Laboratori Nazionali di Legnaro (LNL). The targets were done using the reactive sputtering technique (section 4.2.1). The gas for the target production was enriched in ^{15}N in order to maximize the statistic of the measurements. Each set was composed of five targets of titanium nitride on tantalum backing produced simultaneously in order to obtain the same deposition on each targets (small differences in stoichiometry has been measured after the production). The natural nitrogen gas (N_2) is one of the main contaminants in the experimental setups for target production, because it is the main constituent of the air and it is used also for venting the setups during the maintenance. The final isotopic ratio between ^{14}N and ^{15}N (they are the unique stable isotopes of nitrogen) could be changed by a small contamination of natural nitrogen inside the preparation chamber. Reactive sputtering is a dynamic technique, as a consequence the final amount of deposition could vary in a range of 10-15% both for the target thickness and

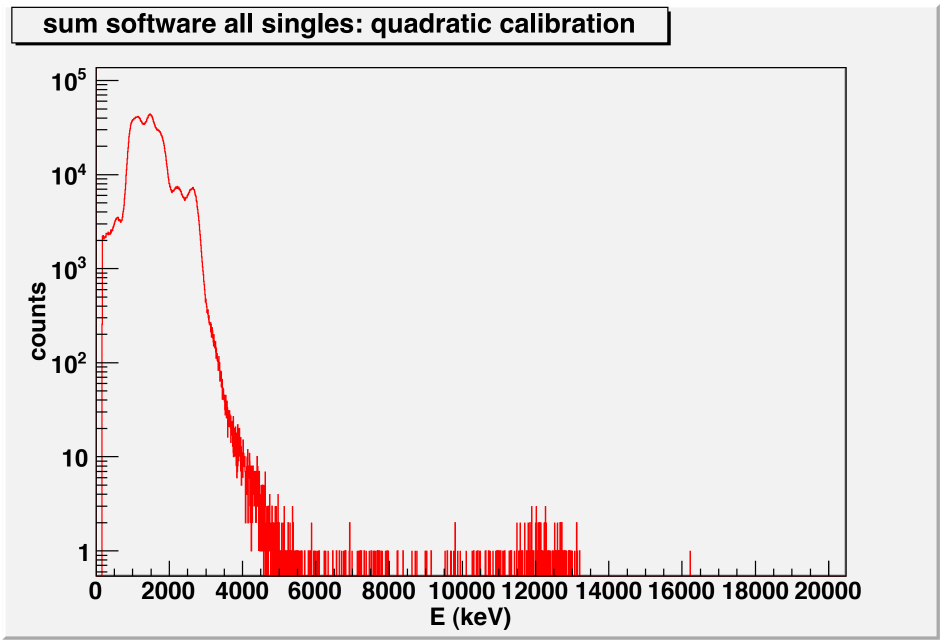

Figure 4.6: *Software sum spectrum acquired at* E_{beam} *= 120 keV.*

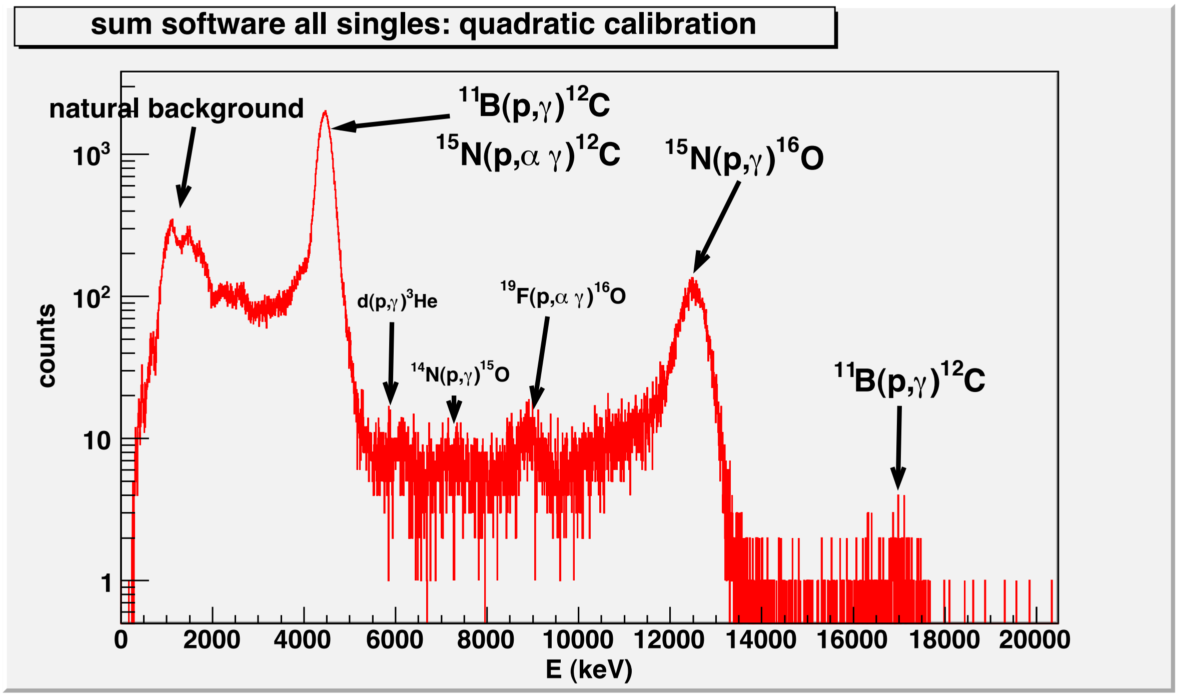

Figure 4.7: *Software sum spectrum acquired at* E_{beam} *= 380 keV. In the figure the main peaks are identified.*

Karlsruhe set		
Target	Integrated Charge (C)	Offline Analysis
Ka1	35	SNMS, ERD
Ka2	26	SNMS, Res Profile
Ka3	116 (20)	SNMS, ERD, Res Profile
Ka4	46	SNMS, Res Profile
Ka5	39	SNMS, ERD, Res Profile

Legnaro set		
Target	Integrated Charge (C)	Offline Analysis
LNL1	7	ERD, Res Profile
LNL2	10	ERD, Res Profile
LNL3	not used at LUNA	ERD, Res Profile
LNL4	not used at LUNA	Res Profile
LNL5	not used at LUNA	ERD, Res Profile

Table 4.1: *The two sets of targets. For each target the integrated charge collected during the LUNA measurements is given. For target Ka3 the total integrated charge was 116 C, but we analyzed runs only until 20 C. Some targets from the LNL set have been used only for the target offline analysis.*

target stoichiometry.

The target composition is one of the most important parameter for the analysis because it affects directly the measured yield. As a consequence the target characteristics were measured in different laboratories. Four different techniques were performed in order to investigate the target properties:

- scan profile of the resonance at 429.5 keV of the ^{15}N(p,$\alpha\gamma$)^{12}C reaction performed at the Forschungszentrum Dresden-Rossendorf in Dresden (called Res Profile in table 4.1).
- Secondary Neutral Mass Spectroscopy (SNMS) performed at ATOMKI in Debrecen
- High Z beam Elastic Recoil Detection (ERD) performed in Munich
- nuclear reaction induced by deuterium on nitrogen performed in Sevilla

The specific measurements performed in each target are reported in table 4.1.

The measurements done with the SNMS technique were in disagreement with the results of the other two techniques and with the specifics from the producer and I decided not to use them in the analysis. Nuclear reactions induced by deuterons were investigated on one target, but the final uncertainties were to much high as compared to the other techniques. In appendix B I will discuss on SNMS and the measurements performed in Sevilla.

4.2.1 Sputtering process for solid target production

Before going deeply into the target analysis procedures a brief description of the targets production will be given in this section.

The deposition sputtering process is based on the erosion of a bulk via the bombardment of the ions of a weakly ionized plasma. The atoms emitted from the bulk cross the plasma region and deposit on a specific backings, this way creating a thin film. The structure and thus the properties of the deposited film are influenced by the characteristics of the bulk, the backing and the plasma.

The plasma is an ionized gas composed by charged and neutral particles as electrons, positive and negative ions, atoms and molecules. When an external electric field is applied, the charged particles form an electric current inside the plasma region and the plasma can be compared to a conducting material. The plasma could be divided into different regions depending on the specific process. In the case of sputtering deposition, the most important plasma regions are the following: the thin glowing region that is produced at the cathode (cathode glow), the dark region close to the cathode (cathode dark space) and the region of negative discharge, as it is represented in Fig. 4.8.

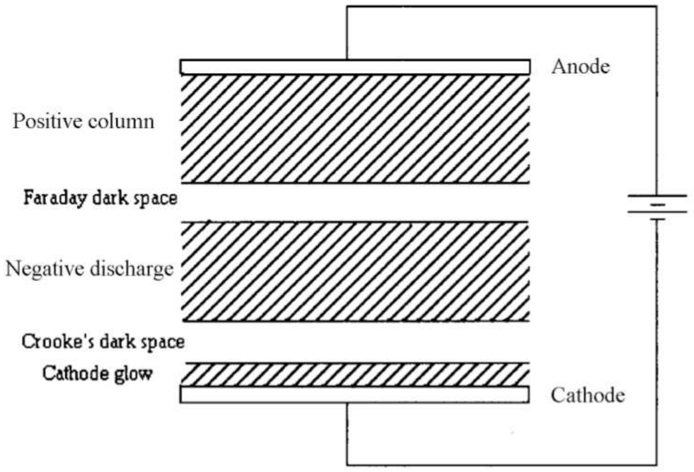

Figure 4.8: *Region of a DC plasma.*

Many important processes for plasma support and film deposition take place in the very thin region called cathode glow: electron emission with consequential ionization of the gas atoms, emission of ions and atoms from the bulk and their deposition on the accreting films. The potential, between cathode and anode, increases linearly until the plasma starts (breakdown). At this time the total voltage is localized between the extremes of the cathode dark space region and this brings to the emission of secondary electrons and the sputtering of the bulk. The Paschen curve (Fig. 4.9) indicates the voltage of the breakdown as a function of Pd, where P is the pressure inside the chamber and d is the distance between the electrodes.

This curve has a minimum for the pressure that minimize the voltage needed with a given geometry of the sputtering chamber. This pressure is used to start the plasma and then it is tuned to the better value for the deposition.

Reactive sputtering [41] is the best technique in order to produce titanium nitride targets

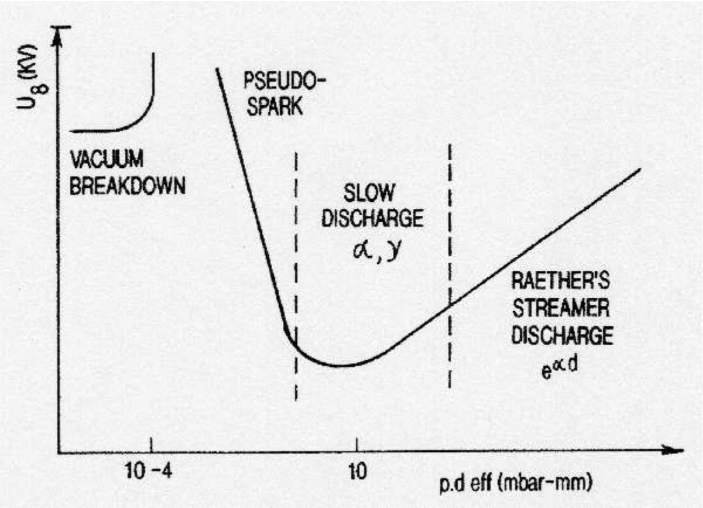

Figure 4.9: *Paschen curve that indicates the electrodes voltage necessary to start the plasma as a function of Pd (P = pressure in the sputtering chamber, d = distance between the electrodes).*

and it could be used when the bulk emits atom species that react chemically with the gas producing the plasma. Reactive sputtering is a quite complex process since the efficiency depends on several parameters: power supplied to the source, concentration of the reactive gas, geometry of the experimental setup. During the process the reactive gas (nitrogen) is mixed with a non reactive gas (argon) inside the sputtering chamber. The argon permits the erosion of the bulk while nitrogen reacts with the atoms sputtered from the bulk and also with the inner surface of the chamber.

The Ti atoms are emitted from the bulk and they cross the plasma reacting with the nitrogen atoms. The created TiN molecules reach the backing and deposit on it. To improve this process the flux of the reactive gas (N_2) is maintained very low.

4.2.2 LUNA target monitor measurements

The scan profile technique is a common method in order to investigate the targets already used several times at LUNA. This technique was performed during the measurements with the LUNA2 accelerator in order to monitor the target condition. It was also used for the study of the target characteristics determined at the tandetron accelerator in Dresden. It exploited the properties of the measured yield on a narrow resonance of reactions well known in literature. The yield of a capture reaction is defined as the ratio between the measured counts in the reference γ-line and the integrated charge on the target by the beam ($Y = \frac{\text{counts in the peak}}{\text{charge}}$). In the case of a resonance at an energy E_0 the measured yield over a target thickness ΔE is:

$$Y(E_0) = \int_{E_0-\Delta E}^{E_0} \frac{1}{E}\frac{\lambda^2}{4\pi}\omega\frac{\Gamma_a\Gamma_b}{(E_r-E)^2+(\Gamma/2)^2}dE \tag{4.2}$$

$$= \frac{\lambda_r^2}{2\pi}\frac{\omega\gamma}{\epsilon_r}\left[\arctan\left(\frac{E_0-E_r}{\Gamma/2}\right)-\arctan\left(\frac{E_0-E_r-\Delta E}{\Gamma/2}\right)\right] \tag{4.3}$$

with the substitution $\omega \equiv (2J+1)(1+\delta_{01})/[(2j_0+1)(2j_1+1)]$ and $\omega\gamma \equiv \omega\frac{\Gamma_a\Gamma_b}{\Gamma}$. In eq. (4.2) λ_r and ϵ_r denote the de Broglie wavelength and the stopping power at the resonance energy E_r, respectively. The yield profile is shown in Fig. 4.10. The value of the plateau is easily to deduce from the (4.2):

$$Y_{max} = \frac{\lambda_r^2}{2\pi}\frac{\omega\gamma}{\epsilon_r}\arctan\left(\frac{\Delta E}{\Gamma}\right) \tag{4.4}$$

If the energy target thickness is much larger than the width of the resonance we can assume

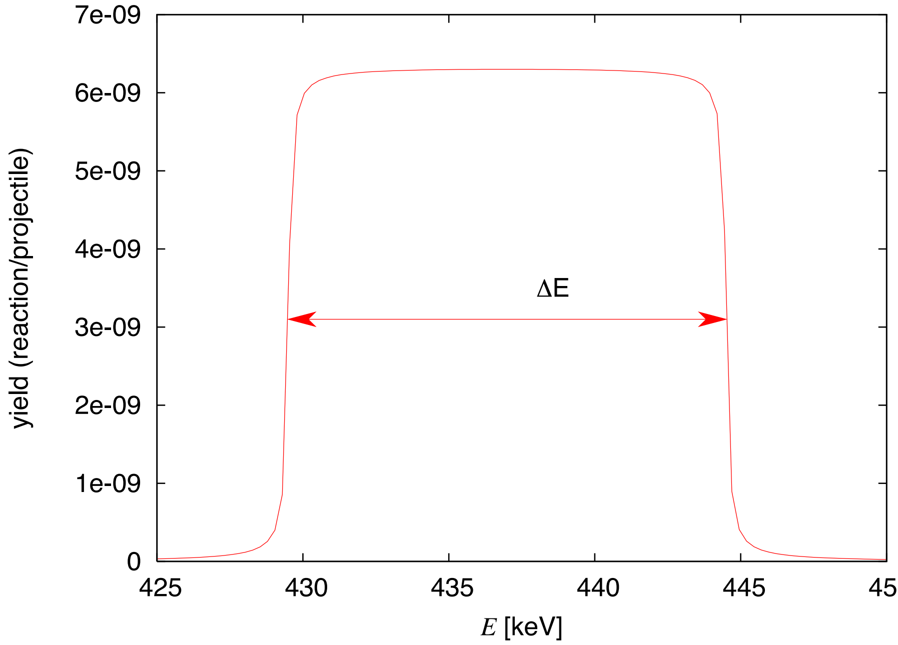

Figure 4.10: *The yield curve of eq. (4.2) plotted for the ^{15}N(p,$\alpha\gamma$)^{12}C resonance at E_p = 429.5 keV. The target thickness, ΔE, is 15 keV. The straggling effect is not considered. For the stopping power ϵ_r eq. (4.6) has been used.*

that the ratio $\frac{\Delta E}{\Gamma} \to \infty$ and the the yield becomes:

$$Y_{max,\Delta E\to\infty} = \frac{\lambda_r^2}{2\pi}\frac{\omega\gamma}{\epsilon_r} \tag{4.5}$$

If the target is not a pure element, but consists of a compound of different element the stopping power, ϵ_r, must be substituted with the effective stopping power:

$$\epsilon_{eff} = \epsilon_X + \sum_i \frac{N_i}{N_X}\epsilon_i \tag{4.6}$$

where X is the active element. In Fig. 4.11 there is an example of measured yield acquired at LUNA with the BGO on the narrow ^{14}N(p,γ)^{15}O resonance at $E_{r,lab}$ = 278 keV. Knowing all the informations on the resonance (i.e. the $\omega\gamma$) and the efficiency of the setup it is possible to deduce the elements abundances in the target measuring the plateau of the yield and the target thickness. Since in the energies range of the LUNA2 accelerator there is not a

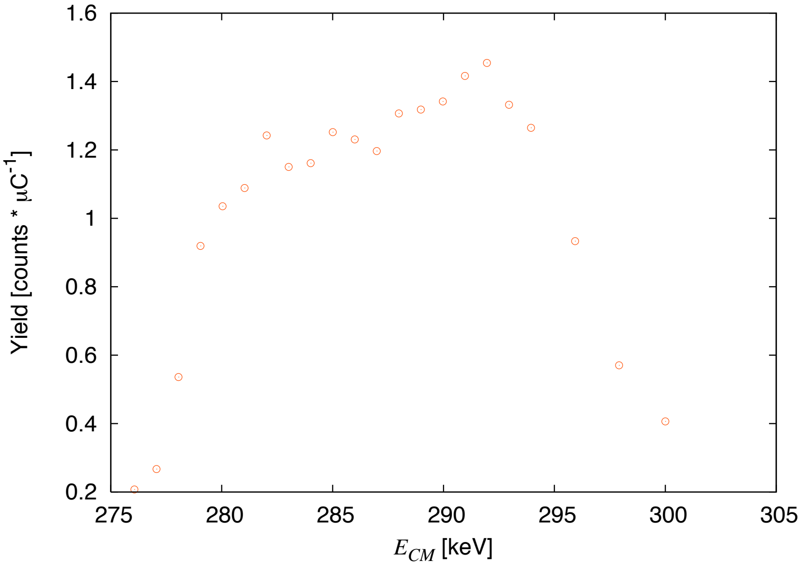

Figure 4.11: *The measured yield acquired on the LNL2 target with the BGO detector at LUNA. The scan is related to the resonance at* E_p *= 278 keV of the* ^{14}N(p,γ)^{15}O *reaction. The peak in the plateau at the* E_{CM} *= 292 keV is not well understood yet. It is probably due to the dynamic flux of the nitrogen gas in the sputtering chamber. Variations in this flux can affect highly the amount of* ^{14}N *in the targets.*

narrow resonance for any reaction induced by proton on ^{15}N , we tried to monitor the target stability and the target properties by measuring the very well known ^{14}N(p,γ)^{15}O resonance at $E_{r,lab}$ = 278 keV (Fig. 4.11). The target deterioration was also monitored acquiring spectra on the resonance of the ^{15}N(p,γ)^{16}O at three different beam energies: 340, 350 and 360 keV. In the case of the Karlsruhe set the scans on the ^{14}N(p,γ)^{15}O resonance showed a strange behavior during the days of measurements. As a matter of fact it seems that the amount of ^{14}N increased by a factor 3 during a week of measurements. In Fig. 4.12 the scans acquired during a week of measurements on the second target of the Karlsruhe set are shown. The ^{14}N is present in the target in a small percent, so its amount can be changed by a small implantation of natural nitrogen (99.634% of ^{14}N) into the target due to the beam, but this prevents to use the scans on the resonance at 278 keV in the target analysis. The effect shown in Fig. 4.12 has been seen in all the targets of the Karlsruhe set, but not in the two targets produced in Legnaro (Fig. 4.13). The reason is that the Legnaro targets had an higher abundance of ^{14}N after the production. In this case the nitrogen implantation effect, due to the LUNA beam is reduced. The LNL targets were also irradiated with less charge as compared to the Karlsruhe one on each target and also this fact can be the reason of the different target behavior.

The resonance scan at the energy of E_{beam} = 278 keV cannot be implemented in the analysis to correct for the target deterioration, but it has been used to get the value for the isotopic enrichment of the ^{15}N. The yield given by the first measured plateau of each target was put in (4.5) to extract the value of the effective stopping power, ϵ_{eff}. Since the plateau was not constant in most targets, we decided to average the values along all the plateau energies. This increased the uncertainty but gave us more stability in the result. The ϵ_{eff}

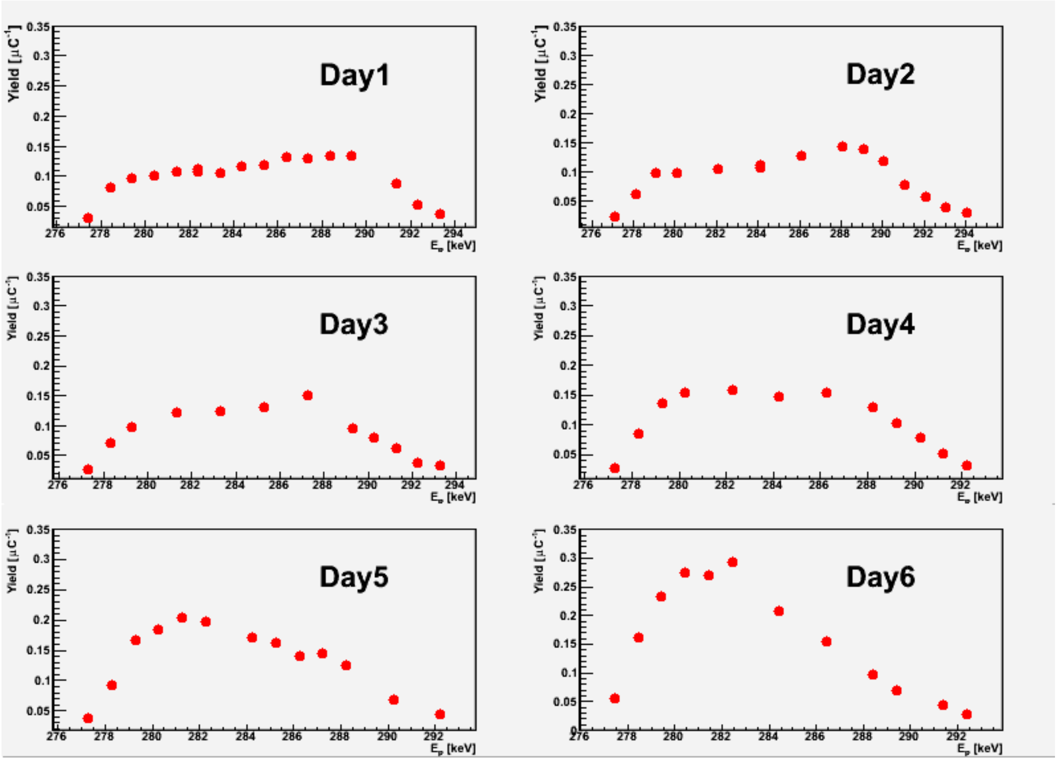

Figure 4.12: *The scans acquired over a week on the target Ka2. The y-axis scale is the same in all graphs in order to underline the increasing of the plateau.*

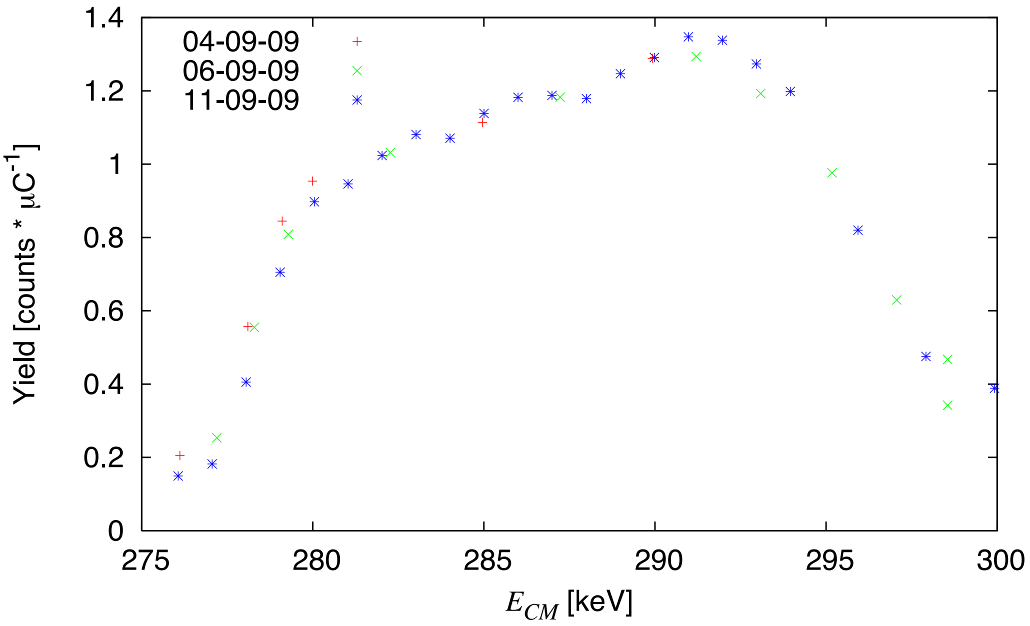

Figure 4.13: *Three scans acquired over a week on the target LNL1.*

value, in the case of the TiN enriched targets, depends on two different parameters: the stoichiometry Ti/N and the isotopic ratio ^{14}N/^{15}N. To show this dependence eq. (4.6) could be written as:

$$\epsilon_{eff}(^{14}\mathrm{N}) = \epsilon_N + \frac{^{15}\mathrm{N}}{^{14}\mathrm{N}}\epsilon_N + \frac{\mathrm{Ti}}{\mathrm{N}}\frac{\mathrm{N}}{^{14}\mathrm{N}}\epsilon_{Ti} \tag{4.7}$$

where $\frac{\mathrm{N}}{^{14}\mathrm{N}}$ can be easily extracted from the isotopic ratio and the stopping power for ^{14}N and ^{15}N has been considered equal since the difference can only arise from the nuclear contribution which is one order of magnitude smaller than the electronic component. The stoichiometry has been determined by the ERD measurements (sec. 4.3) and inserted in the eq. (4.7) in order to obtain a precise value for the isotopic ratio. The amount of ^{14}N has been determined with the ^{14}N(p,γ)^{15}O resonance scans with an uncertainty of 25%. From this value we have reconstructed the ^{15}N concentration in our targets taking into account the stoichiometry of the targets. The final results are reported in table 4.2

4.2.3 Dresden measurements

The ^{15}N(p,$\alpha\gamma$)^{12}C reaction has a very narrow (Γ = 0.19 keV [32]) resonance at 429.5 keV in the laboratory system. This energy is beyond the range of the LUNA2 accelerator. As a consequence we have to performe those measurements at the Tandetron accelerator at the Forschungszentrum Dresden-Rossendorf (see Fig. 4.14).

Figure 4.14: *The tandetron accelerator.*

The proton beam is produced by a cesium sputtering source, IONEX 860-C, that produces negative ions. They are accelerated in two steps by the same potential. The accelerator can accelerate proton beam in a range of energies from 0.2 MeV to 6.6 MeV. The beam current could vary from 1 nA up to 200 μA according to the transmission parameters. The target chamber was mounted on the channel at 30°. On that channel there is a quadrupole and a steerer system in order to focus and direct the beam on the target. We used two different type of chambers: the one shown in Fig. 4.15 and the one already used in the measurement at LUNA (Fig. 4.16). In both cases a collimator was inserted at a distance of 40 cm from the target in order to focus the beam. We used collimators with different diameter size (diameter = 2, 4 and 5 mm) and with the hole shifted in respect to the beam axis (shift = 0, 2, 3 mm) in order to control the beam size and position on the target. This because we were interested in measuring the target surface at different points. In the chamber in Fig. 4.15 the target could be inserted at 55° in respect to the direction of the beam and it was cooled by a water recirculating system. This system cooled also the copper collimator. A high purity germanium detector with efficiency of 60% was used for the γ-ray detection and was put at an angle of 55° in close geometry (Fig. 4.15).

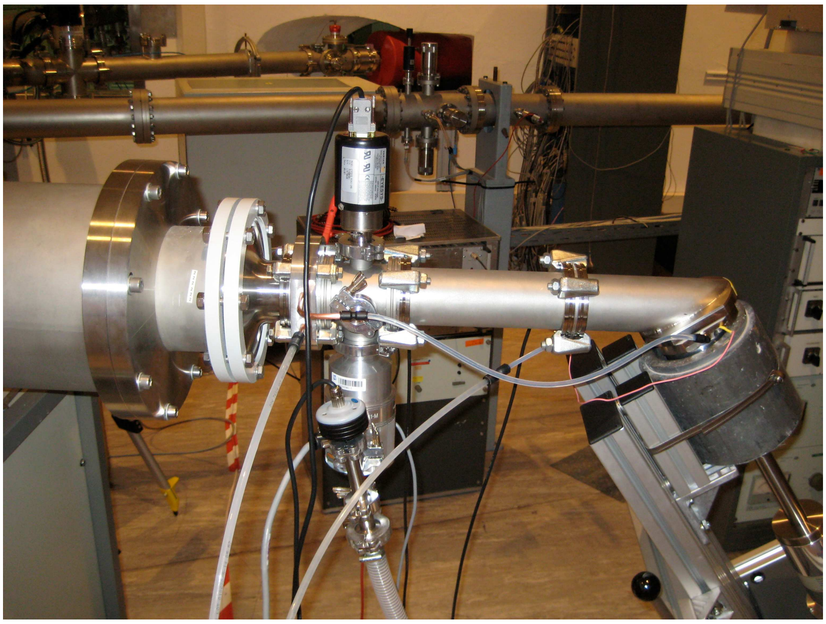

Figure 4.15: *The chamber with the target at 55° in respect to the beam direction. The 60% Germanium detector is placed in the position used in the measurements.*

The targets were measured after the irradiation at the LUNA accelerator. For all targets[3] the resonance profile was investigated in two different positions: inside the area irradiated by the LUNA beam (called "beamspot" area) and in a area outside the LUNA beamspot (called "virgin" area) (Fig. 4.17). In this way we got information of the target conditions after and before the irradiation at LUNA. The beam position measuring the target has been measured putting a paper instead of the target in the holder. We decided to rotate the target in order to measure different position instead of changing the beam position by the collima-

---

[3] The target 1 of the set from Karlsruhe has been not measured, beacuse was used in the destructive SNMS technique.

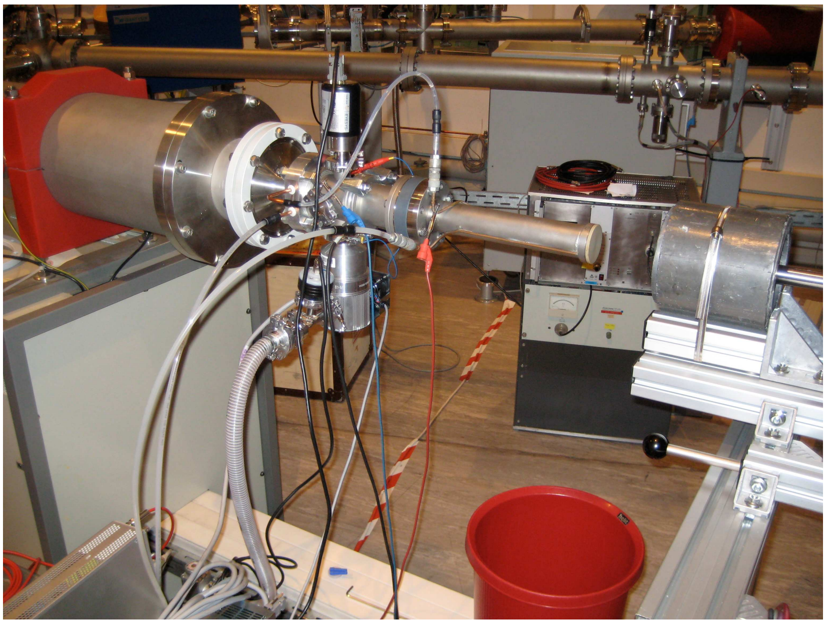

Figure 4.16: *The target chamber already used in the measurements at LUNA with the BGO detector. The 60% Germanium detector was placed at 0° in respect to the beam direction.*

tors. We checked the stability of the beam position during all the measurements. During the measurements the current was about 1 μA.

Figure 4.17: *An example of the "virgin" area (left) and "beamspot" area (right) measured position for the target Ka2. The beam position is defined by the black circle. This cirlce has been superimposed on the target picture by a graphic software.*

We deduced the resonance scan on the γ-ray at 4.4 MeV due to de-excitation of the first exited state of ^{12}C. In Fig. 4.18 and Fig. 4.19 the results of the profile measurements on the targets produced in Karlsruhe and in Legnaro are shown. It is evident that the first set of targets was used too much, because not only the target thickness was reduced, but also the target plateau. Looking at eq. (4.5) this means that the nitrogen concentration changed during the measurement, since the ϵ_r in (4.5) changes with the stoinchiometry ratio Ti/N. The LNL targets seem more stable probably because we decided not to irradiate too much this second set of targets in order to prevent possible negative effects on the analysis at the resonance energies around 335 keV.

At low energies the yield is relatively affected by the target deterioration in respect to at

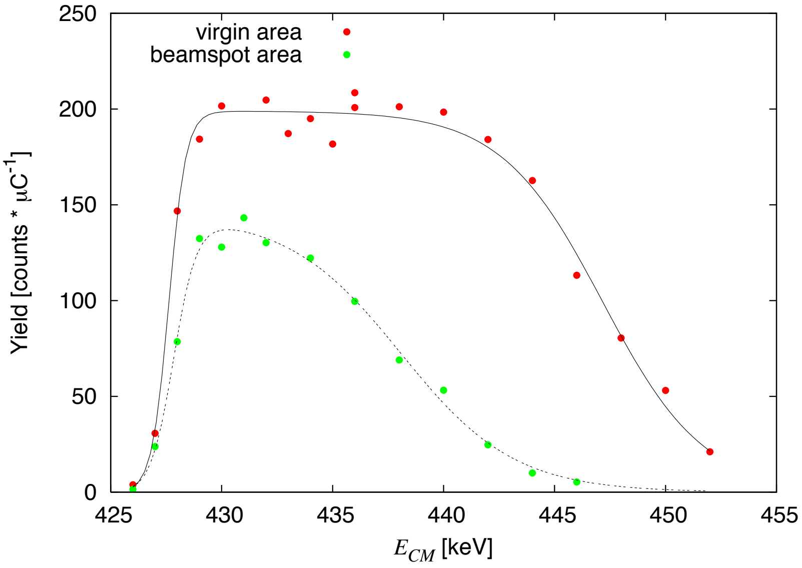

Figure 4.18: *Resonance scans on "virgin" (red points) and "beamspot" (green points) areas on the target Ka4. The profiles have been fitted with a arctan function in order to show the profile behavior. This function has not been used in the analysis.*

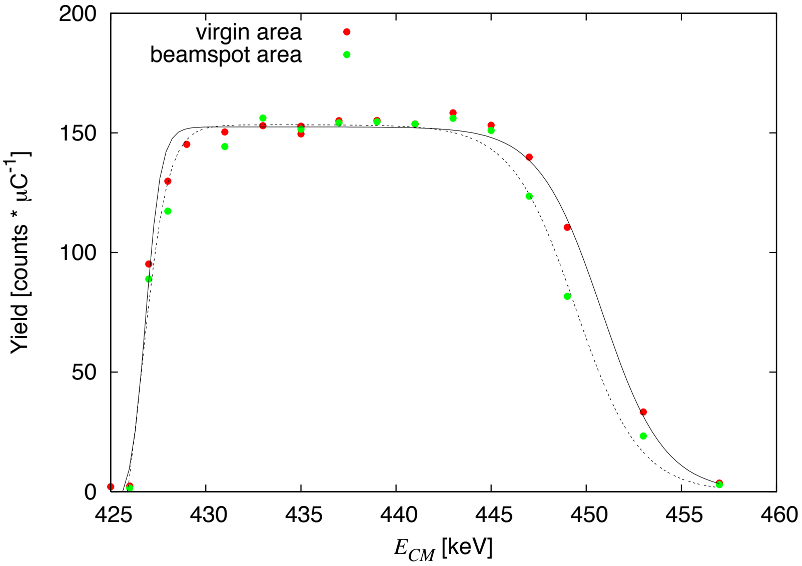

Figure 4.19: *Resonance scans on "virgin" (red points) and "beamspot" (green points) areas on the target LNL2. The profiles have been fitted with a arctan function in order to show the profile behavior. This function has not been used in the analysis.*

high energies. This is due to a combination of two factors: the Coulomb term in the cross section and the stopping power. The stopping power for titanium nitride is shown in Fig. 4.20. It has been calculated using the most recent database [23] for a stoichiometry ratio Ti/N = 1. The energy loss is more significant at energies around 80 keV where the Bragg peak is.

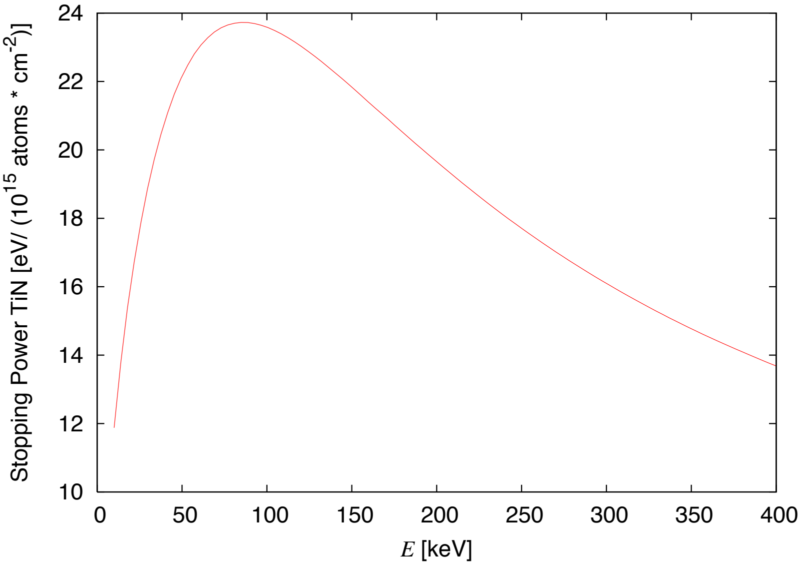

Figure 4.20: *The stopping power curve for TiN from [23].*

The cross section (the one given in the Mukhamedzhanov *et al.* paper [15]) has been integrated over the target thickness (assumed of 20 keV at E_p = 278 keV from the experimental resonance scans as in Fig. 4.12) in order to understand how much the target deterioration changes the measured yield. In Fig. 4.21 we have reported the percentage difference of the integral cross section in the case of new target and a target at the 70% of its initial thickness value: $\Delta\sigma(\%) = \frac{\int\sigma(\Delta E=100\%)-\int\sigma(\Delta E=70\%)}{\int\sigma(\Delta E=100\%)}$. From the blue curve in Fig. 4.21 we can see that the measured yield at energies below 100 keV is different by less then 10% in the case of a target reduced by 30% in respect to the original target. The effect of the resonance at E_R = 312 keV is evident in the blue curve and it affects the curve slope, but the effect of the Coulomb potential remains predominant. In order to minimize the uncertainty due to the deterioration in the final S-factor at higher energies we decide to analyze only the low energy runs for each Karlsruhe target. The targets from the Legnaro set were measured limiting the integrated charge to 10 C. In this way the target deterioration is quite negligible (less than 10% at all energies). In section 4.6 the spectra analysis is described in details including the deterioration corrections.

Since the current integrated on the target at LUNA was a very well known parameter, it was used in order to interpolate between the "beamspot" and "virgin" scans using the integrated charge as parameter. In that way it is possible to reconstruct the target properties at time of each acquired spectrum. The procedure of target reconstruction is discussed in sec. 4.6.

Using the value of the ^{15}N(p,$\alpha\gamma$)^{12}C $\omega\gamma$ = (0.017 ± 0.004) keV [32], the efficiency curve

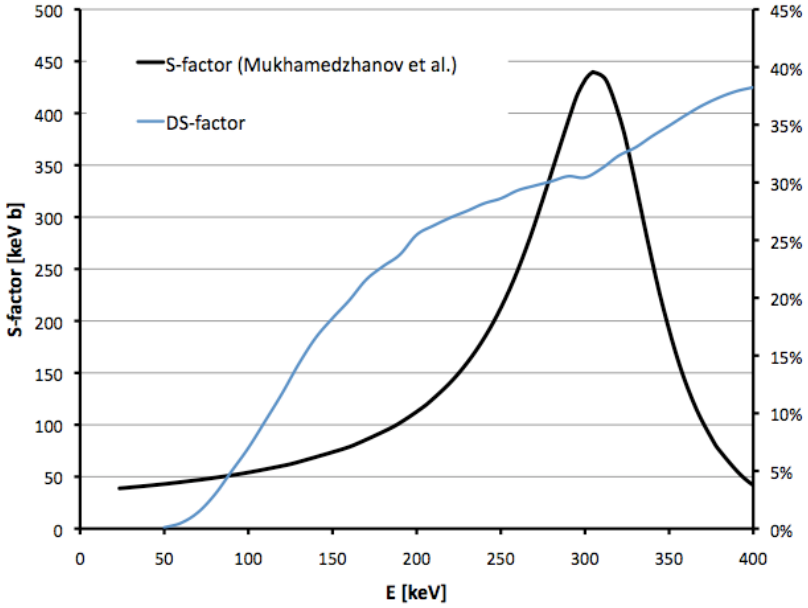

Figure 4.21: *The value of* $\frac{\int\sigma(\Delta E=100\%)-\int\sigma(\Delta E=70\%)}{\int\sigma(\Delta E=100\%)}$ *is reported in blue. For comparison the* ^{15}N(p,γ)^{16}O *S-factor from [15] is shown in the black curve.*

of the detector and taking into account the angular distribution quoted in literature [42] it is possible to extract a value for the stoichiometry and the isotopic ratio from eq. (4.5) and eq. (4.6). Unfortunately the uncertainties on the $\omega\gamma$ and on the angular distribution given in literature are larger than 15%. This value is too high compared to the other sources of systematic uncertainty in the analysis. Therefore we decided to use the resonance scan results only in relative ad to evaluate the stoichiometry parameter and isotopic ratio with other techniques.

4.3 High Z Elastic Recoil Detection

The High Z Elastic Recoil Detection (ERD) has been used in order to find an exact value for the stoichiometry and isotopic for the ratio of the targets.

The inherent advantage of Ion Beam Analysis (IBA) is its potential for quantitative analysis of elemental contents. The ion-atom scattering processes could be in good approximation described as two body reactions where many body contributions are weak and they can be corrected for. At high energies the elastic scattering reaction could be well described by point-like Coulomb interaction, as long as the energy is significantly lower than the Coulomb threshold for nuclear reaction, and this allows the detection of all elements in the sample at the same time. In ERD analysis the recoil ions scattered off into forward directions are detected (see Fig. 4.22). The usage of heavy ions, in respect to the light ions used in RBS, has two advantages: the momentum transfer is sufficient to detect all light elements with different technique (time fo flight, ΔE E spectra, magnetic or electrostatic analysis) and the number of projectile scattered into the detector is significantly reduced.

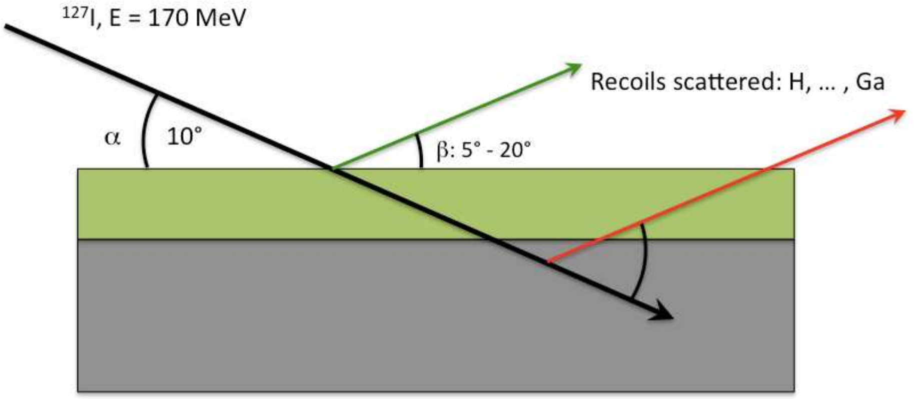

Figure 4.22: *Geometric scheme for the ERD experiment.*

The beam is ^{127}I with 170 MeV energy. The high energy beam reduces the effect of beam straggling and it allows to explore deeper layer of the target in respect to low energy beams. The indium beam hits the target with an angle of 10° as shown in Fig.4.22 and the elements of the target are sputtered at different angles according to the kinematics. The charge and the mass of the recoils can be investigated with two different type of detectors:

- a double stage $\Delta E - E$ detection system composed by an ionization chamber for ΔE detection and a silicon detector for the E measurement,
- a large magnetic spectrograph for specific recoil ion identification if higher mass detection resolution is needed.

The first solution has been used for the detection of titanium, tantalum and the total nitrogen. The above mentioned setup is shown in Fig. 4.23. This is an hybrid detector telescope, principally consisting of transversal field Frish grid ionization chamber and a silicon position sensitive PIN dynode for residual energy measurements. The cathode electrode and the entrance window are kept at ground potential. The cathode is positioned 21 mm from the Frish grid and the anode electrode is 7 mm apart from the grid. Isobutane is used as detector gas filling and an electronic regulation ensured constant gas flow and pressure. The entrance window is made of a grid-supported mylar foil of 125 μg/cm^2 thickness and 90% transmission. The maximum solid angle of detection Ω of the detector is 4.5 msr and it is regulated by slits in the scattering plane. They could be reduced in the case of simultaneously measurements with both the ionization chamber and the Q3D magnet, but this is not our case.

The ERD cross section scales as:

$$\sigma_{ERD} \sim \left(\frac{Z_1(M_1 + M_2)}{M_2 E_1} \right)^2 \tag{4.8}$$

where E_1, Z_1 and M_1 are the energy, nuclear charge and mass of the projectile, respectively, M_2 the recoil ions mass. The ERD cross section has been used in order to calculate the

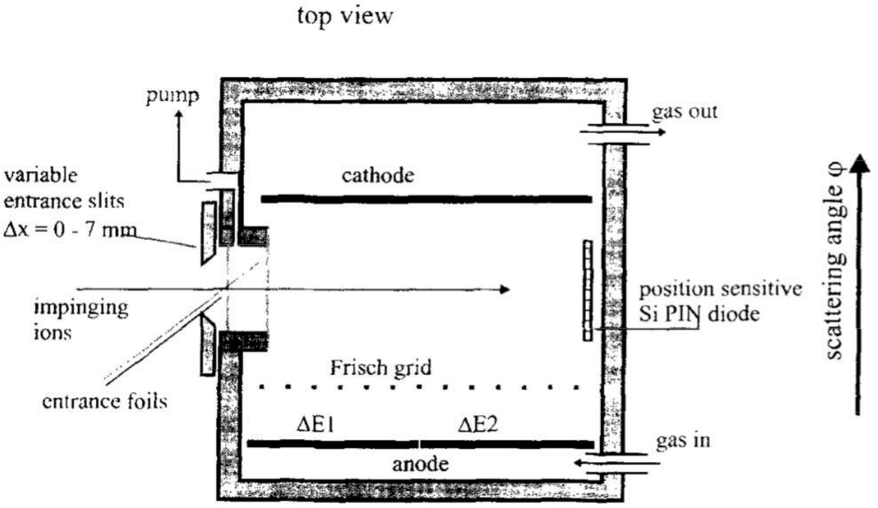

Figure 4.23: *Schematic view of the detector layout [43].*

Target	Ti/N	^{15}N/N$_{tot}$
Ka2	0.973±0.015	0.984±0.020
Ka3	0.993±0.015	0.984±0.020
Ka4	0.98±0.02	0.984±0.020
Ka5	0.971±0.016	0.985±0.020
LNL1	1.18±0.02	0.946±0.019
LNL2	1.16±0.02	0.942±0.019

Table 4.2: *The stoichiometry ratio obtained for each target with the ERD technique.*

different amount of elements in the targets weighting the measured counts by this value in order to obtain the absolute value for the stoichiometry. The results of this analysis are reported in table 4.2.

The measured sample is intended to be destroyed when depth profile of any element is altered by the impinging beam. For this reason in order to keep sensitivity as good as possible large solid angles of detection are required. Several msr of solid angle of detection are used in the ERD experiment. An energy profile can be generated from the $\Delta E - E_{tot}$ spectrum (Fig. 4.24) for any element by separately projecting the corresponding area of every element to the energy axis. From the 2D spectrum the contribution of each element in the target could be easily deduced and separated. The analysis were performed in Munich using the conversion algorithm KONZERD [44]. More details of the ERD technique with heavy ion beam could be found in [43] and reference therein.

4.4 Target Analysis

The target description is an important parameter to be implemented in the analysis, because it is directly connected to the measured yield via the integrated cross section along the target thickness.

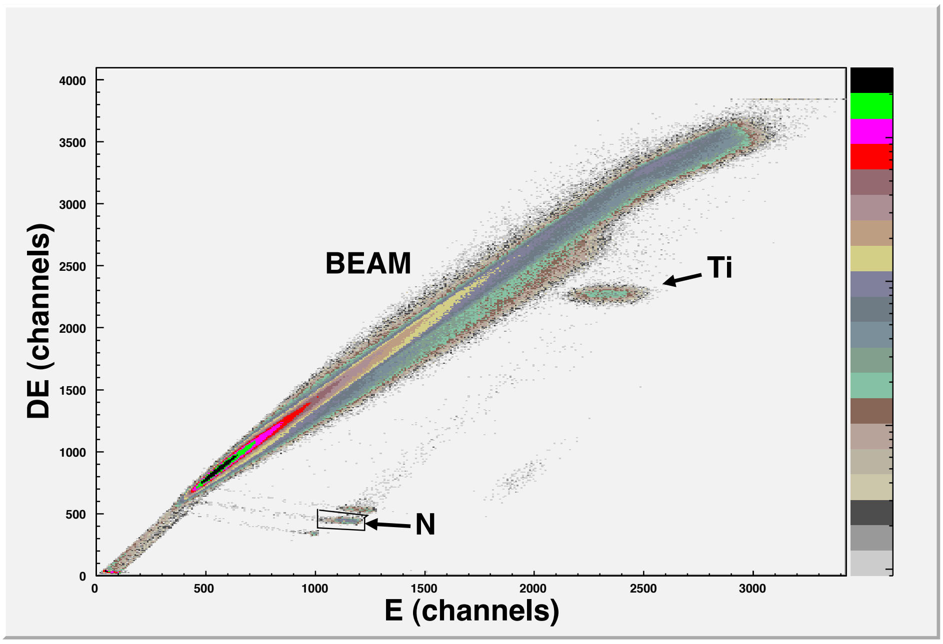

Figure 4.24: *$\Delta E - E_{tot}$ spectrum of recoil scattered from the enriched target produced in Legnaro. Most of the counts in the spectrum are from the scattered ^{127}I beam. This noise is very well separated from the recoil counts. The two regions of titanium and nitrogen are visually selected by a circle.*

The resonance scans performed on the ^{15}N(p,$\alpha\gamma$)^{16}O reaction at the Tandetron in Dresden have been converted into target profiles implementing the stoichiometry measured by ERD and the isotopic ratio calculated from the resonance scans performed at LUNA with the ^{14}N(p,γ)^{15}O.

We have considered that the yield of the plateau in the "virgin" area scan is the one related to the Ti/N and ^{15}N/N$_{tot}$ ratios at the initial condition of the target. Since the yield for a target with a thickness higher than the Γ of the resonance is only affected by this two parameters, as shown in eq. (4.5) and eq. (4.6), the variation of the yield in the target is only due to the variation of the stoichiometry ratio Ti/N. This is an assumption, because we did not consider the straggling effect that should be negligible since it is smaller than the right tail of the scans.

For each target scan on "virgin" area the value of the plateau has been called Y_{Max}. It has been calculated as the average of the yield values on the plateau on the "virgin" scan, for each target. This value could be analytically expressed, combining (4.5) and (4.6) as:

$$Y_{Max} = \frac{\lambda^2}{2\pi} \frac{\omega\gamma}{\epsilon_N + \frac{^{14}\mathrm{N}}{^{15}\mathrm{N}}\epsilon_N + \left(\frac{\mathrm{Ti}}{\mathrm{N}}\right)_{ERD} \frac{\mathrm{N}}{^{15}\mathrm{N}}\epsilon_{Ti}} \tag{4.9}$$

where λ is the de Broglie wavelength and ϵ_i is the stopping power for the element i. In each point of the resonance scans (see Fig. 4.18 and Fig. 4.19) the measured yield, Y_i, is given by the same equation as the Y_{Max} but with a different stoichiometry Ti/N. The ratio between this two yields can be written as:

$$\frac{Y_{Max}}{Y_i} = \frac{\epsilon_N + \frac{^{14}\mathrm{N}}{^{15}\mathrm{N}}\epsilon_N + \left(\frac{\mathrm{Ti}}{\mathrm{N}}\right)_i \frac{\mathrm{N}}{^{15}\mathrm{N}}\epsilon_{Ti}}{\epsilon_N + \frac{^{14}\mathrm{N}}{^{15}\mathrm{N}}\epsilon_N + \left(\frac{\mathrm{Ti}}{\mathrm{N}}\right)_{ERD} \frac{\mathrm{N}}{^{15}\mathrm{N}}\epsilon_{Ti}} \tag{4.10}$$

where the subscript i refers to the different depth inside the target. The stoichiometry $\left(\frac{\mathrm{Ti}}{\mathrm{N}}\right)_i$ along the target thickness has been deduced from the eq. (4.10) and this allows the calculation of the nitrogen concentration in all samples. The target stoichiometry has been also used to calculate the stopping power along the target thickness in order to convert the energy loss into the target thickness, expressed in unit of 10^{15} atoms/cm^2. After the procedure described above the target profile expressed in nitrogen concentration versus depth can be deduced as reported in Fig. 4.25. In the case of the resonance scan for "beamspot" area we deduced the target profile with the same procedure described above utilizing eq. (4.10). The value used for Y_{Max} in this case is the same one deduced for the "virgin" area plot, because it is referred to the stoichiometry at the beginning of the target exposition to the beam. The two extrapolated target profiles for the "virgin" and "beamspot" cases are different both for the target thickness parameter and for the nitrogen concentration. These two plots have been used as input to the analysis in order to deduce the target profile at the time of each individual run. This is one of the input to the S-factor analysis program. During the experiment the integrated charge on the target was written as a parameter for each acquired run. The two target profiles were interpolated linearly using the total integrated charge as parameter in order to obtain the target profile at the time of the analyzed run. The target degradation is not really linear so this hypothesis introduces an error, but this effect is important only at the energy of the resonance, whereas at low energy the target deterioration affects much less the yield. The choice to analyze only the targets LNL 6 and LNL 7 at the energy above E_{beam} = 110 keV goes in this direction avoiding the problem of interpolation thank to the negligible deterioration observing in the resonance profiles of these targets.

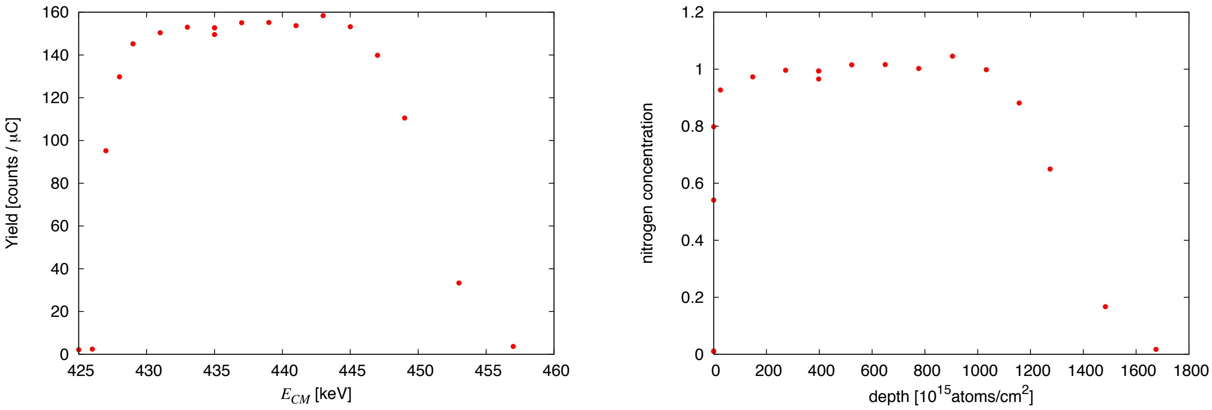

Figure 4.25: *The resonance scan on the "virgin" area on target LNL7 is reported on the left. On right there is the deduced profile plot from the plotted resonance scan. The plot on the right is calculated using eq. 4.10 and the technique described above.*

4.5 The 4π-BGO detector efficiency

Also in the case of the solid target experiment we used the same GEANT4 code already adopted for the gas target analysis. The electronic chain used to register the γ-ray spectra of the BGO detector is not the same used in the gas target experiment and it has already been described in section 2.4. The chamber has been entered properly in the simulation. The efficiency has been measured using both radioactive sources and high energy narrow resonances of known reactions. A comparison of the simulation with the measurements has been done in order to understand the precision of the code.

4.5.1 Radioactive sources measurements and efficiency stability

The first step of the efficiency measurements was the acquisition of spectra with different calibrated radioactive sources. Radioactive nuclides emit γ-ray at low energies ($E_\gamma < 3$ MeV), compared with the one emitted by the ^{15}N(p,γ)^{16}O. At this energies the effect of dead layers is more relevant so this calibration is a very good probe for testing the GEANT4 simulation.

Three different nuclides have been used in order to cover the largest possible energy range: a ^{22}Na, ^{60}Co and a ^{137}Ce. The cesium source is a good probe in order to study the absolute efficiency of the detector, because it produces a single γ-ray at an energy of 661 keV. In this case there is not any summing peak effect to take into account for the absolute efficiency calculation. Differently, the cobalt source produces two γ-rays very close in energy: 1173 keV and 1333 keV. The BGO detector has a resolution ten times worse than a germanium detector and the two peaks are not well separated but it is still possible to distinguish them. The 4π-BGO enhances the summing of the two γ-rays and it has been used to test the simulation in the sum spectrum reconstruction. In Fig. 4.26 and in Fig. 4.27 the sum spectrum and a spectrum relatively to a single crystal for the cobalt source are reported. The decay scheme of the sodium source is quite complicated. The spectrum is also affected by the trigger threshold on the 511 keV peak. On the other hand the ratios between the counts in the peaks at 1275 keV and 1786 keV or 2550 keV are good probes in order to verify the simulation. In Fig 4.28 the sum spectrum for sodium-22 source is shown and the three peaks are quite evident.

The sodium source had a rectangular plexiglass support, whereas the cobalt and cesium sources had circular supports. Unfortunately both these supports could not be placed in the target holder. It was necessary to implement them as new dead layers into the simulation. The list of the sources is written in table 4.3.

The efficiency depends on the target position in respect to the BGO detector and also on where the beam hits the target. The target changing procedure needed the movement of the detector so it was necessary to understand the effect of misplacement of the BGO during data acquisition. A visual marker fixed the detector position, but the movement by different shifters could increase the error due to the parallax.

The reproducibility of the efficiency has been checked by changing the detector position

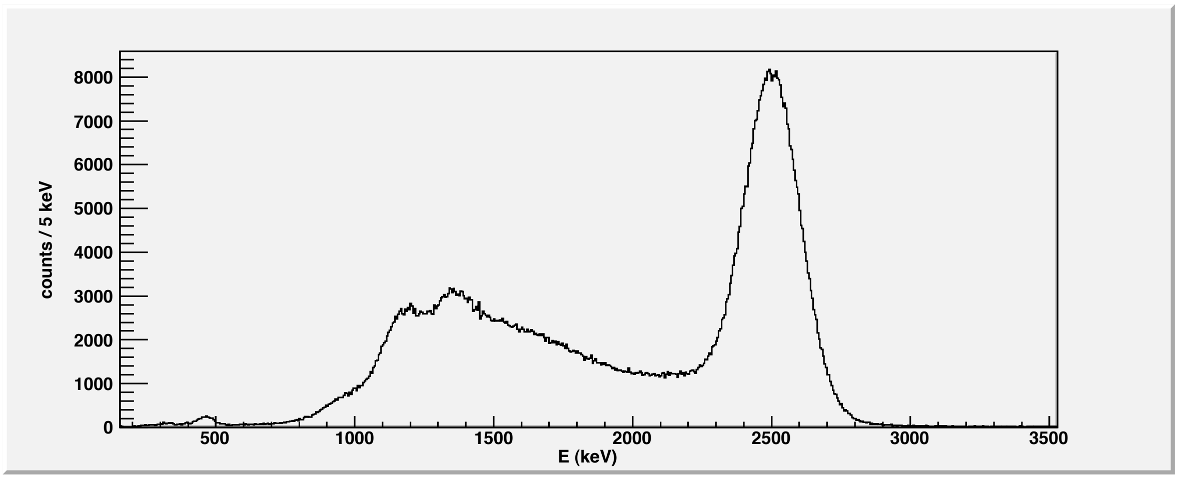

Figure 4.26: *The sum spectrum for the* ^{60}*Co source. The spectrum is obtained by the software sum. The scale of the x-axis has been chosen to underline the summing peak at 2.5 MeV.*

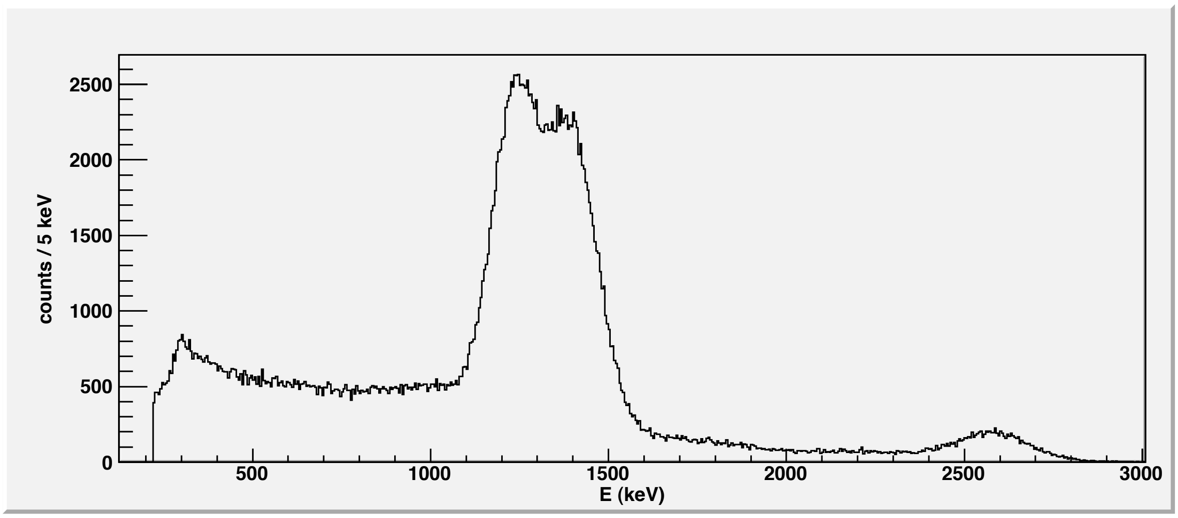

Figure 4.27: *The single spectrum for the* ^{60}*Co source. The two peaks are evident. The spectrum is the relative to the crystal 1 of the BGO detector.*

Nuclide	Initial Activity [kBq]	Production Date	uncertainty
^{137}Cs	4.58	17 Jul 1998	3.1%
^{60}Co	3.41	19 Jun 2000	3.0%
^{22}Na	419.9	1 Jul 1990	3.0%

Table 4.3: *The radioactive sources used in the efficiency measurements. The activity value is given at two sigma uncertainty.*

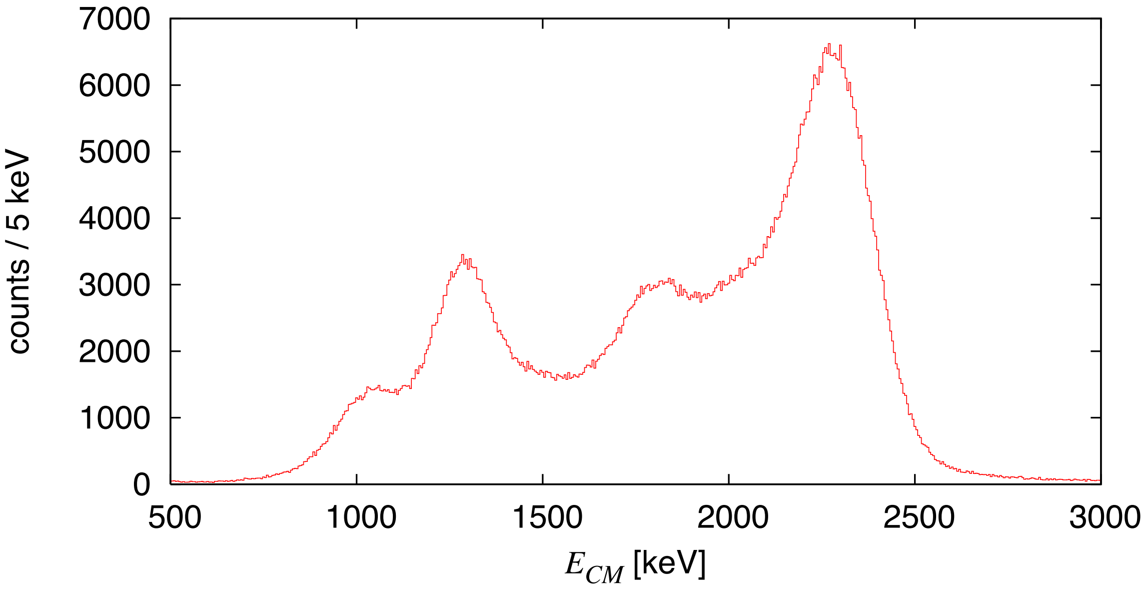

Figure 4.28: *The sum spectrum for the* ^{22}*Na source. The three peaks at 1275, 1786 and 2550 keV are evident.*

from the nominal position in three different configurations of the ^{60}Co source inside the target chamber. These configuration have been called Pos 1, Pos 2 and Pos 3 and they are summarized in the list below:

- Pos 1 is the best approximation of the target position during the data taking. The source is placed on the backing in the same position as the target (shown in the photo on right side of Fig. 4.29). Behind the backing there is a ring which fixes the backing itself to the chamber. In the case of this efficiency measurement the ring is fixed to a plastic cap and this plastic cap closes the chamber. During the nitrogen target measurements the chamber was closed by the backing, fixed with the ring. Cooling water

- in Pos 2 the source is in between the tantalum backing and the plastic cap. The ring was in between the cap and the source

- in Pos 3 the source is in the same position as in Pos 2, but it was shifted by 8 mm from the center.

The trigger threshold prevented to acquire spectra with the cesium source, because the γ-ray emitted by the source is below 700 keV. As consequence the trigger threshold was modified (reduced by a factor two) in order to have a spectrum also with this source. In this condition we measured an experimental efficiency value of 63.6% for ^{137}Cs and we

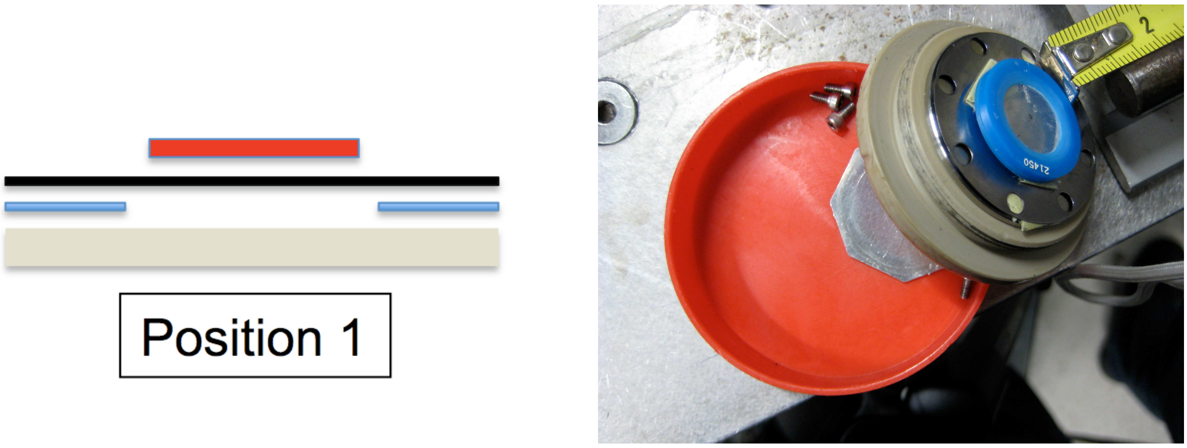

Figure 4.29: *Pos 1 for the source during the efficiency measurements. The position scheme is shown in the left panel. The backing is represented in black, the ring in blue the source in red and the plastic cap in light brown. The photo of the source is in the right part of the picture.*

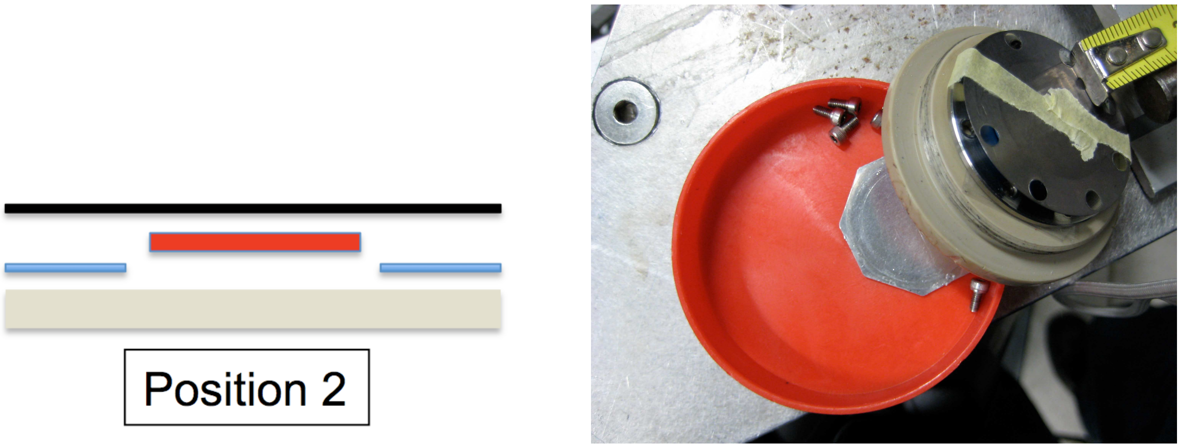

Figure 4.30: *Pos 2 for the source during the efficiency measurements. The position scheme is shown in the left panel. The backing is represented in black, the ring in blue the source in red and the plastic cap in light brown. The photo of the source is in the right part of the picture.*

obtained a 65.3% from the simulation. The discrepancy is 2.8%. Since the threshold value could change the efficiency, spectra with ^{60}Co in Pos 1 were acquired with both the two threshold conditions and the results are reported in Fig. 4.32 together with the other stability measurements.

A misplacement of the detector seems to affect more Pos 2 and Pos 3 than Pos 1. In both the three cases this effect is lower than 1% for a detector shift of 2 cm in both the two possible directions. Even if the BGO position was changed manually a misplacement of more than 2 cm was not possible. Pos 2 and Pos 3 are more affected by the detector shifting but not enough to increase this contribution to the uncertainty. The main difference from the three position was found between Pos 2 and Pos 3. This difference was always less than 2% so this value has been assumed. Lowering the threshold we increase also the efficiency of less than 2.5%. After these tests the trigger threshold was set at an high value in order to reduce the dead time in the in-beam measurements. The effect of the threshold is more relevant at low energies so it is expected to reduce at higher energies.

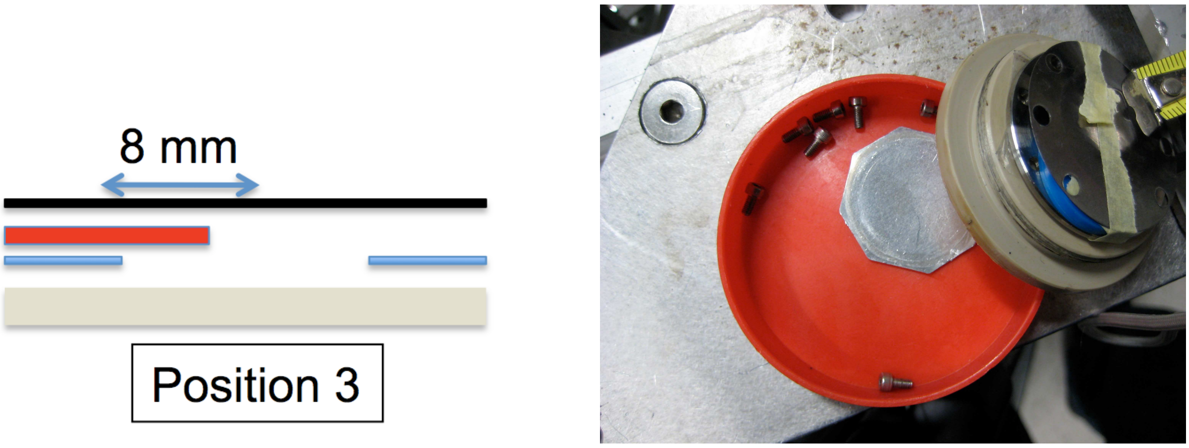

Figure 4.31: *Pos 3 for the source during the efficiency measurements. The position scheme is shown in the left panel. The backing is represented in black, the ring in blue the source in red and the plastic cap in light brown. The photo of the source is in the right part of the picture.The length of the shift of the source is underlined in the picture.*

4.5.2 High energy efficiency

The description of the dead layers in the simulation code has been fixed with the radioactive sources measurements. Since the γ-ray produced by the ^{15}N(p,γ)^{16}O has an energy of 12 MeV we decided to perform a check of the GEANT4 code making a comparison with the experimental spectra acquired with a borated target. A $LiBO_2$ target (40 keV nominal energetic thickness at the E_{beam} = 163 keV) has been irradiated with 11.5 μA proton beam intensity at the energy of the resonance of ^{11}B(p,γ)^{12}C at E_R = 149 keV. The target was implanted on a backing of the same type already used for the Ti^{15}N targets. In this way the boron reaction was investigated in the same conditions as the ^{15}N(p,γ)^{16}O reaction. Since natural boron contains 80.2% ^{11}B and since the resonance is quite strong with $\omega\gamma = 5.2 \pm 0.6$ eV [45], the γ-spectrum is expected to be dominated by the lines from this resonance.

Both the sum of the six single channel histograms and the sum spectrum (offline gain-matched sum of the list-mode data, event per event) are analyzed and compared with the simulation. The dead time amounted to 9% and pile-up effects caused only minor distortions in the observed spectra (Fg. 4.34).

The decay of the resonance is well-studied in literature. The ^{12}C level at 16106 keV mainly decays (92.2%) into the first excited state at 4439 keV, which subsequently decays to the ground state (Fig. 4.33).

There is a 4.2% branching directly from the resonance to the ground state. Further there are minor branching ratios for decay to the excited state at 12710 keV with 1.4% and to 9641 keV with 2.2%. It should be noted that all ^{12}C states except for the first excited state lie above the threshold for α-emission and therefore decay also in the α-channel. Trough the 12710 keV state, there is some feeding contribution to the 4439 keV state, however due to the limited branching ($1.4\% \cdot 0.29\% = 0.004\%$) this effect is negligible.

Therefore, the ratio between the counting rates for 11.7 MeV (16106→4439) and 4.4 MeV (4439→0) is exclusively given by the efficiency ratio for these two γ-energies and there is

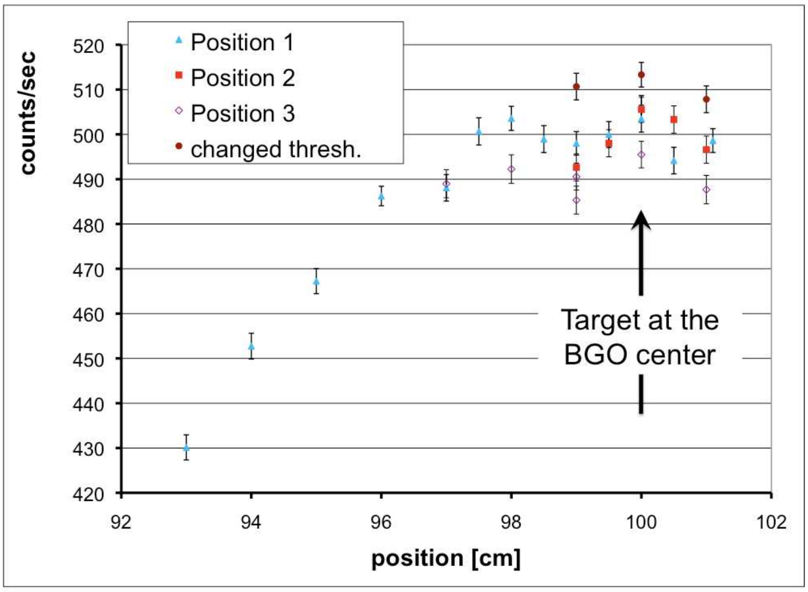

Figure 4.32: *The measured efficiency for the ^{60}Co source is reported for the three different positions reported in the legend (see text) and for two different values of the trigger threshold.*

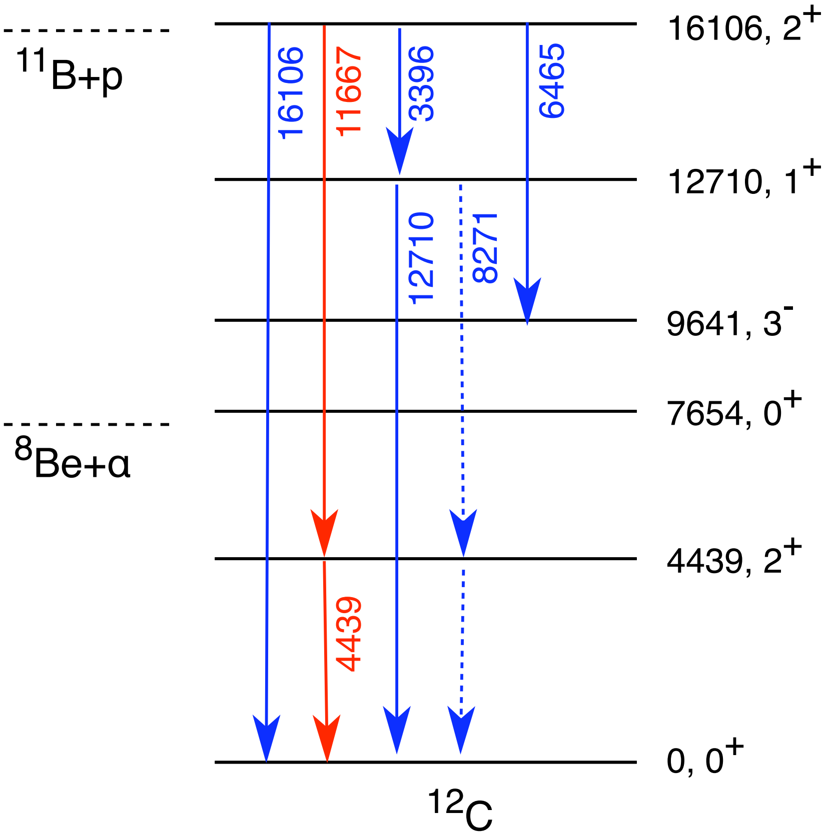

Figure 4.33: *Level scheme of ^{12}C from ENSDF [40], the levels and transitions important for the E_{beam} = 163 keV resonance in ^{11}B(p,γ)^{12}C (E_X = 16106 keV in ^{12}C) are highlighted. The main γ-rays found in the spectrum are shown as arrows. The couple of γ-rays used for the efficiency calibration validation is shown in red.*

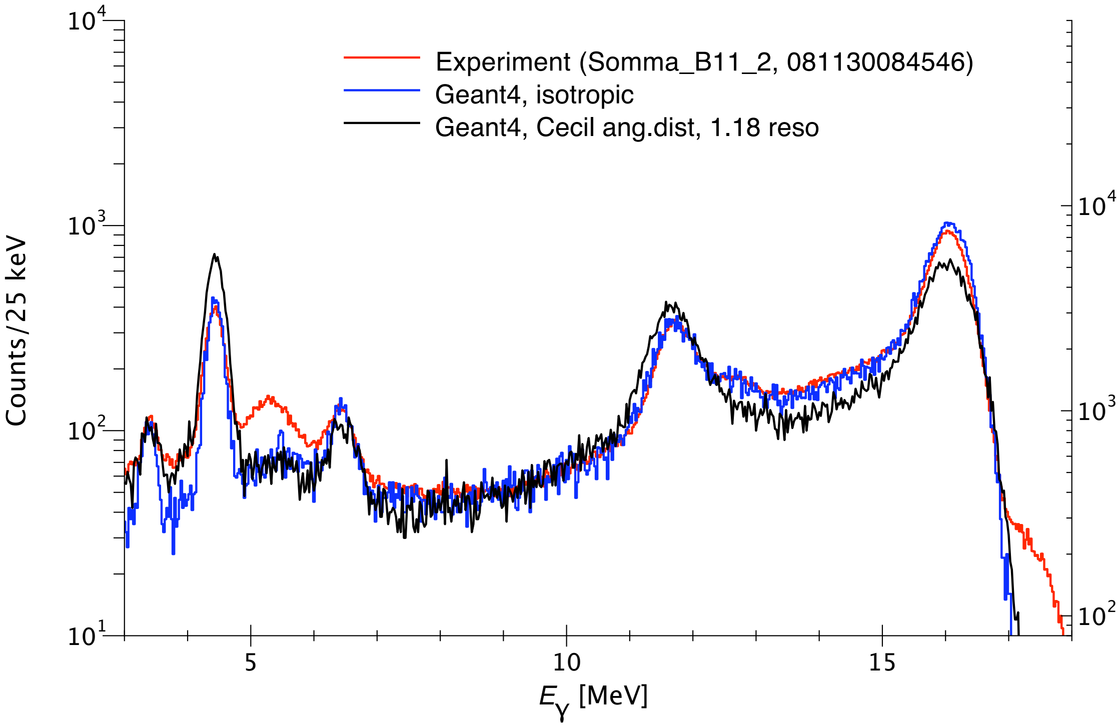

Figure 4.34: *Sum spectrum. Comparison of experimental data and two different GEANT4 simulations for the* E_{beam} *= 163 keV resonance in the* ^{11}*B(p,*γ*)*^{12}*C reaction.*

no uncertainty from branching ratios. This makes this couple a perfect case for a check of calculated γ-efficiency curves, if the angular distribution is well-known.

The angular distribution of those two γ-rays has recently been studied by Cecil *et al.* [35], giving experimental data and also a Legendre parameterization for the 4.4 and 11.7 MeV cascade γ-rays and also for the 16.1 MeV ground state transition. All of the angular distribution show a minimum at 90° and a maximum at 0°, meaning emission of the γ-ray back into the direction of the beam, where there is no active BGO detector material. For the simulation, the literature branching ratios [45] have been implemented using their recommended values. In addiction, several options have been implemented for the angular distribution. Here, both the case of isotropic angular distribution and angular distribution as given by Cecil *et al.* [35] are shown.

In Fig. 4.34 the comparison of the experimental spectrum and two simulated spectra are shown for the case of software sum of the list mode data. All the boron peaks are well reproduced by both the simulations, but the isotropic angular distribution seems to fit better the data. There is a peak at 5.1 MeV in the experimental spectrum produced by a contaminant not well understood. This peak is completely far away from the region of interest for the ^{15}N(p,γ)^{16}O reaction. The pile-up is not implemented in the GEANT4 code, but it plays a minor role in the spectrum.

The angular distribution plays a major role when one tries to derive an efficiency from the resonance strength and target profile. Since the angular correlation of the two γ-rays at 11.7 and 4.4 MeV has been not measured yet, the absolute efficiency in the summing

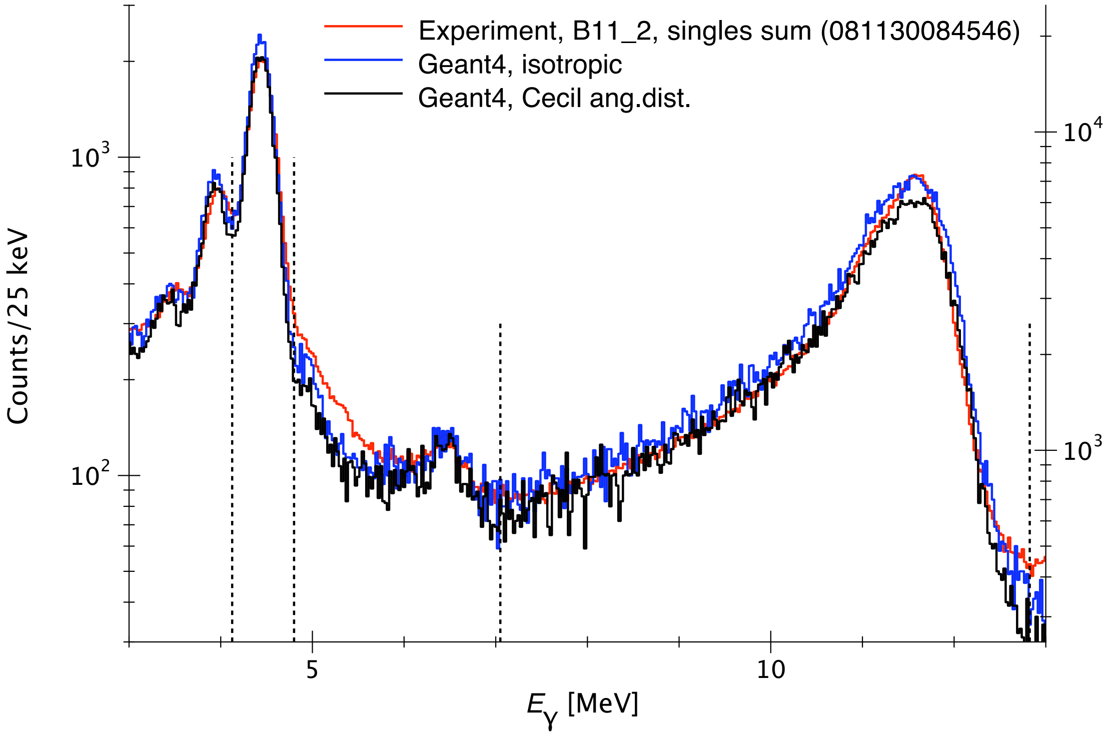

Figure 4.35: *Singles spectra. Comparison of experimental data and two different GEANT4 simulations for the* E_{beam} *= 163 keV resonance in the* $^{11}B(p,\gamma)^{12}C$ *reaction. The region of interest for the ratio determination in table 4.4 are shown as dashed lines.*

spectrum is hard to measure with a good precision. In addiction the complicated nature of the $LiBO_2$ target and the limited precision of the literature information on the resonance strength prevent the efficiency calculation too.

We focused our attention on the reproducibility of the branching ratio informations in the sum of all singles. In that case the simulation shows overall good agreement with the experimental spectrum (Fig. 4.35). To be more specific, the counting rate in the 4.4 MeV peak, which shows a characteristic Gaussian shape with nearby single-escape, and the 11.7 keV with its much broader response function are compared. When taking very simply the areas of the peaks without any background subtraction, the agreement with the simulation is within ±3% (table 4.4, columns 2-3). When a linear background is used for the 11.7 MeV γ-line and a Gaussian fit with linear background subtraction for the 4.4 MeV γ-line, the agreement is even better, within ±1%.

This agreement means that the simulation correctly reproduces the energy dependence of the γ-efficiency from 4.4 to 11.7 MeV within ±3%.

A second check is the comparison of the ratio between the Gaussian fitted (with linear background) single escape and full-energy peaks. This ratio shows whether the GEANT4 simulation correctly predicts the attenuation of the γ-line by the pair-production effect. Here the agreement is somewhat worse, only within ±6%. However, pair production only accounts for around 20% of the total γ-ray attenuation in BGO at 4.4 MeV [46] and the two peaks are difficult to fit because they are very close in energy (compared with the energy resolution of the detector): changing the region of fit the ratio could change.

	Ratio 11.7/4.4	Deviation	Ratio 3.9/4.4	Deviation
Experiment	1.792±0.004	–	0.268±0.003	–
GEANT4, isotropic	1.851±0.013	(3.3±0.7)%	0.279±0.009	(3.8±3.1)%
GEANT4, Cecil [35] ang. dist.	1.806±0.013	(0.8±0.8)%	0.284±0.008	(5.7±2.7)%

Table 4.4: *Comparison of experimental and simulated ratios of counting rates for the sum of the single histograms. The uncertainty is the statistical uncertainty of the GEANT4 simulation.*

4.6 Analysis and S-factor evaluation

In all the runs the region of interest ROI$_1$ was simply integrated. ROI$_1$ is defined as the region from $E_{CM} + Q$ - 2.5 MeV to $E_{CM} + Q$ + 1.3 MeV as shown in Fig. 4.36, while ROI$_2$ is defined as the area between 14 and 18 MeV. The problem of background subtraction has been investigated in sec. 4.1. We decided to use only the spectra where the ROI$_2$ counts were smaller than the 3% of the ROI$_1$ counts.

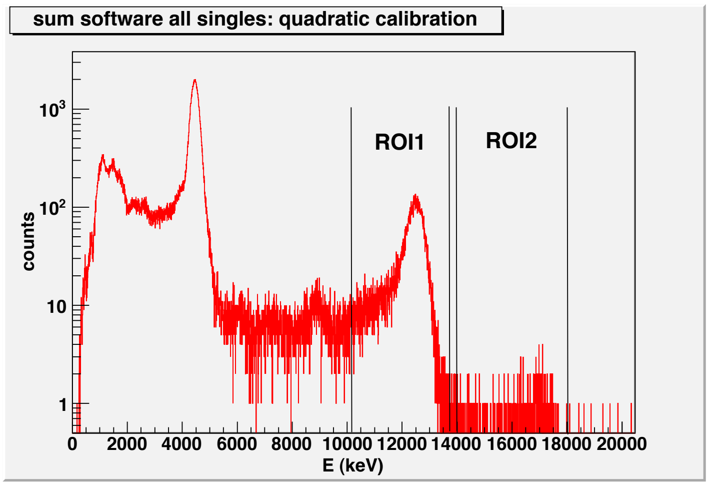

Figure 4.36: *Software sum spectrum acquired at E_{beam} = 380 keV. In the figure ROI$_1$ and ROI$_2$ are shown.*

ROI$_1$ includes an important part of the Compton tail on the left and the end of the peak on the right, but it excludes the boron summing peak counts on the right of the ^{15}N peak.

Dividing the counts in the ROI$_1$ by the charge, the measured yield (Y_{lab}) was determinated. It is proportional to the integral of the cross section along the target thickness multiplied by the efficiency of the detector as in equation (4.2). Knowing the target characteristics (see section 4.2) and the detector efficiency (η_{BGO}), the yield in the eq. (4.2) could be calculated analytically. The cross section, $\sigma(E)$, could be written in term of the S-factor:

$$\sigma(E_{beam}(x)) = S(E)\frac{1}{\frac{m_{15}}{m_p+m_{15}}E_{lab}(x)}\exp\left(-2\pi\cdot 7\cdot\alpha\cdot\sqrt{\frac{m_p c^2}{2E_{lab}(x)}}\right) \tag{4.11}$$

where m_p and m_{15} are the mass of proton and the mass of ^{15}N, respectively, c the vacuum speed of light, $E = \frac{m_{15}}{m_p+m_{15}} E_{lab}(x)$ the center of mass energy, $\alpha = \frac{2\pi q_e^2}{hc}$ the fine structure constant and the exponential function models the penetration through the Coulomb barrier for incident s-wave protons. We can compact the non nuclear part of the cross section introducing the abbreviation $\epsilon(E_{lab}(x))$:

$$\epsilon(E_{lab}(x)) \equiv \frac{1}{\frac{m_{15}}{m_p+m_{15}} E_{lab}(x)} \exp\left(-2\pi \cdot 7 \cdot \alpha \cdot \sqrt{\frac{m_p c^2}{2E_{lab}(x)}}\right) \tag{4.12}$$

Finally the yield is related to the cross section in this way:

$$Y = \frac{N_\gamma}{N_p} = \int_{x_0}^{x_{max}} S(E_{lab}(x)) \cdot \epsilon(E_{lab}(x)) \cdot \eta_{BGO} \cdot n_{target}(x) \cdot \frac{^{15}N}{N} \mathrm{d}x \tag{4.13}$$

where $n_{target}(x)\mathrm{d}x$ is the total nitrogen in the target in unit of atoms/cm^2 obtained by the resonance scans in sec. 4.2. In eq. (4.13) the energy E_{lab} has been calculated using the energy loss $\frac{dE}{d\tilde{x}}(E_{lab}(\hat{x}))$ in units of $\frac{\mathrm{eV}}{10^{15}\,\frac{\mathrm{atoms}}{\mathrm{cm}^2}}$ from [23]. The resulting integral is evaluated numerically in small steps x_i:

$$E_{lab}(x) = E_p - \int_{\hat{x}=0}^{\hat{x}=x} \frac{dE}{d\tilde{x}}(E_{lab}(\hat{x})) \cdot n_{target}(x)\mathrm{d}x \tag{4.14}$$

$$E_{lab}(x_i) = E_{lab}(x_{i-1}) - \frac{dE}{d\tilde{x}}(E_{lab}(x_{i-1}) \cdot (x_i - x_{i-1}) \tag{4.15}$$

Putting in eq. (4.13) an hypothetical S-factor we are able to calculate the integral in the (4.13) obtaining a simulated yield, Y_{sim}. Y_{sim} can be directly compared to the experimental yield, Y_{exp}, in order to obtain the final S-factor since:

$$S(E_{eff})_{exp} = \frac{Y_{exp}}{Y_{sim}} \cdot S(E_{eff})_{th} \tag{4.16}$$

where $S(E_{eff})_{th}$ is the hypothetic S-factor and E_{eff} is the effective energy calculated as:

$$E_{eff,lab} = \frac{\int_{x_0}^{x_{max}} S(E_{lab}(x)) \cdot \epsilon(E_{lab}(x)) \cdot n_{target}(x) \cdot \frac{^{15}N}{N} \cdot E_{lab}(x)\mathrm{d}x}{\int_{x_0}^{x_{max}} S(E_{lab}(x)) \cdot \epsilon(E_{lab}(x)) \cdot n_{target}(x) \cdot \frac{^{15}N}{N}\mathrm{d}x} \tag{4.17}$$

The procedure has been done selecting three types of hypothetical S-factors:

- the parametrization of the R-matrix fit from [15],
- a flat S-factor (in this case we tried many values)
- a recursive method where the output of the calculating program was used as input in the program itself until the final result converges

In both the three cases we obtained the same result for the final S-factor within 1%. When there are many runs at the same energy we weighted average the S-factor results.

The statistic uncertainty due to the peak integration is very low except at low energies where it reaches 10%. The charge was measured directly on the target and the uncertainty quoted on the measured device was 1%. The nitrogen profile has been deduced by the resonance scans in sec. 4.2. The target deterioratio is derived form eq. (4.10) which depends from the stopping power evaluation and from the Y_{Max} parameter. The stopping power uncertainty is 4.0% [23]. The uncertainty on Y_{Max} is 7%, obtained averaging the values on the plateau on each target. The uncertainty on the target deterioration effect is finally quoted as 8.1%. The target stoichiometry is measured by the ERD technique on each target and reported in table 4.2, while the isotopic ratio has been deduced by the ^{14}N(p,γ)^{15}O resonance scans. The errors on these parameters are reported in table 4.2 and they contribute for a 2% to the total systematic uncertainty. The detector efficiency has been determined by the GEANT4 code and calculated in all the integrated region of the γ-spectrum with 3% uncertainty. The simulation is also affected by the unknown angular correlation and cascade transition already discussed for the gas target experiment. Their contributions are reported in table 4.6. The last uncertainty we have to take in account is the energy calibration. It introduces errors $\Delta_{stat}E_p$ and $\Delta_{syst}E_p$ that are shown in table 4.6. The final S-factor I obtained are shown in Fig. 4.37 and reported in table 4.5.

In summary, we have measured the ^{15}N(p,γ)^{16}O reaction in the whole LUNA2 energy range from the resonance at E_R = 312 keV down to 70 keV center of mass energy. The solid target data are in good agreements with the gas target one in the overlapping region. This is significant since the two setups are affected by completely different systematic errors. Our data are lower by a factor two as compared to the previous direct measurement [14] at low energies and they are also lower at the energies of the resonance at E_R = 312 keV. We also disagree with the R-matrix fit at the region of the resonance since this fit is done starting from the previous measurements. In particular, we confirm the trend of the extrapolated S-factor to be lower by a factor two than the NACRE extrapolation.

The LUNA results cover completely the Gamow peak in novae. Classical novae are stellar explosions in cataclysmic binary systems, consisting of a white dwarf star and a low-mass, main sequence companion. The system is close enough to allow mass transfer episodes. The matter flow forms an accretion disk that surrounds the white dwarf and ultimately accumulates on its surface, building up a semi-degenerate envelope until a violent thermonuclear runaway takes place. As a consequence, a significant fraction of material, enriched in the products of hot hydrogen burning, is ejected.

The spectroscopic studies of novae reveal the composition of the underlying dwarf, thereby constraining the composition of the stellar evolution models. The observed elemental abundances also reflect the evolution of the thermonuclear runaway, such as peak temperatures and expansion timescales, and thus provide constraints to models of stellar explosions. The novae have been proposed as the major source of the isotopes ^{13}C, ^{15}N and ^{17}O (José and Hernanz [10]). The effect of variations in the ^{15}N(p,γ)^{16}O reaction rate has been recently investigated by Iliadis *et al.* [12] processing four different models for nova explosion. This nucleosynthesis calculations have shown that a factor 2 lower ^{15}N(p,γ)^{16}O rate results in up to 30% reduction in the final ^{16}O yield, depending on the nova temperature. This result is constrained by the initial presence of oxygen in the binary system.

E_{eff} (keV)	S(E_{eff}) (keV b)	$\Delta S/S_{stat}$(%)	E_{eff} (keV)	S(E_{eff}) (keV b)	$\Delta S/S_{stat}$(%)
72.6	52.5	5.9%	259.1	201.8	2.0%
80.6	49.8	3.8%	260	207.3	1.3%
88.4	57.3	9.5%	261.2	212.9	1.0%
105.2	57	5.8%	262.3	212.1	1.9%
114.6	51.8	5.7%	263.3	217.6	2.1%
123.4	56.9	3.0%	264.2	221.3	2.1%
132.7	62.3	4.2%	265.2	220.9	1.7%
143.5	66.7	2.0%	266.3	224.8	1.2%
151.3	54.4	2.5%	267.5	226	2.0%
162.1	77.5	1.0%	268.5	231.4	1.9%
170.4	78	1.5%	270.3	237.9	1.7%
179.8	85.2	1.6%	272.2	240.7	1.9%
189	90.8	1.8%	274.3	248.9	0.8%
198.3	99.8	0.8%	283.6	280	2.0%
207.9	112.3	2.1%	283.9	278.3	1.2%
217.3	120.4	1.3%	293.4	305.1	0.7%
227.1	132.4	1.3%	302.7	311.2	1.0%
236.6	149.4	1.2%	312	301	0.6%
246	167.7	1.7%	321.5	269.4	0.5%
251.5	180.5	1.5%	331	221.7	0.5%
252.5	185.1	1.6%	340.3	176.4	1.3%
253.4	185.4	1.6%	340.6	176.6	0.9%
254.4	194	1.8%	349.8	131.9	1.1%
255.3	192.2	1.7%	354.7	120.7	1.5%
256.2	197.4	1.8%	359.4	97.3	1.5%
257.2	205.8	1.9%	364.1	92.1	1.4%
258.1	200.5	1.7%	368.8	78.6	1.4%

Table 4.5: *Effective center of mass interaction energy E_{eff}, S-factor and relative statistical uncertainties. Systematic uncertainty is 11% for all points.*

José *et al.* [11] have developed in 2007 a new model for novae explosion in the most primitive, low metallicity binaries. They showed that these *primordial novae* eject more massive envelopes and display a larger nuclear activity than *classical novae*. Our measurements will be inserted in these models as soon as possible in order to understand the effect of the revised value of ^{15}N(p,γ)^{16}O in the element production in these new types of novae explosions.

Source of uncertainty	Details found in	Effect on S-factor
Target deterioration	Section 4.4	8.1%
^{15}N isotopic ratio	Section 4.2.2	2.0%
Ti/N stoichiometry	Section 4.3	2.0%
Beam intensity	[20]	1.0%
Effective energy	[20]	3.0%
γ-ray detection efficiency	Section 4.5	3.0 %
γ-ray capture to excited states	Section 2.4	1.9%
γ-ray angular distribution	Section 2.4	4.0%
^{11}B(p,γ)^{12}C background	Section 4.1	3%
Total systematic uncertainty		11.0%

Table 4.6: *Systematic uncertainties and their effect on the solid target S-factor value.*

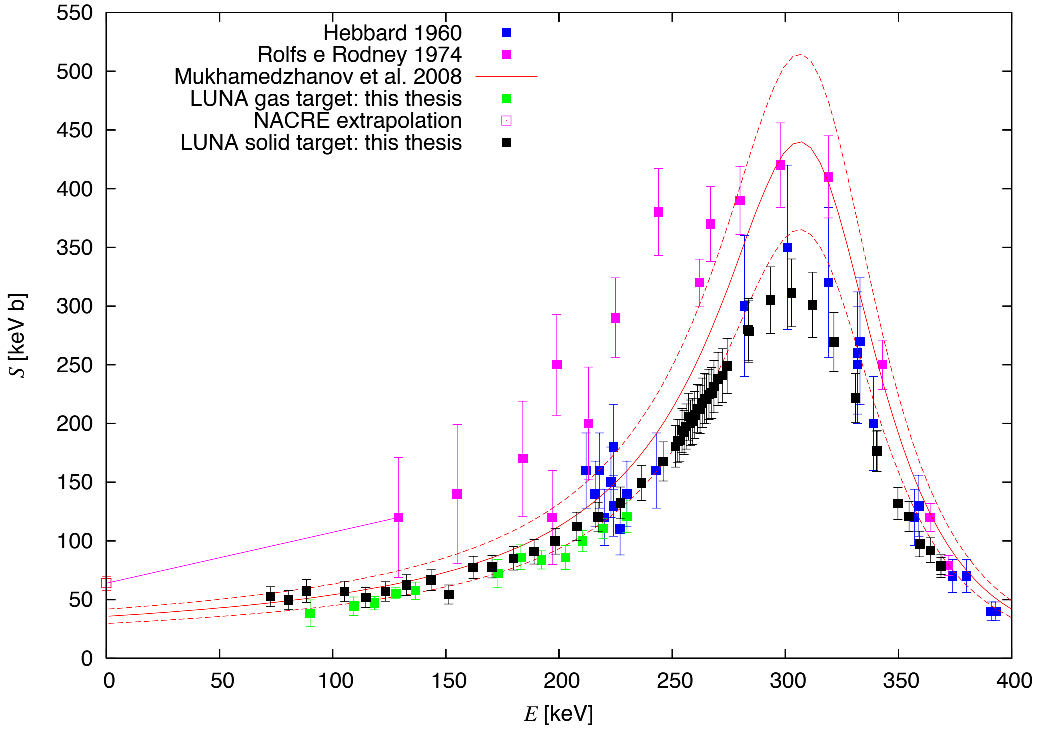

Figure 4.37: *Astrophysical S-factor for the ^{15}N(p,γ)^{16}O reaction as as function of the center of mass energy. The LUNA solid (black) and gas (green) target data are presented with data from Hebbard [13] (blue) and from Rolfs and Rodney [14] (purple). The curve represents the R-matrix fit from the ANC data [15] with the quoted errors (dashed curves). The NACRE extrapolation is also reported (pink).*

Chapter 5

Conclusions

In this thesis I have presented a new study of the ^{15}N(p,γ)^{16}O reaction in a range of center of mass energy from 380 keV down to 70 keV. This reaction is important in hot-CNO scenarios as nova explosions, but the cross section was never measured within the nova Gamow peak. In addition, there was a discrepancy between previous direct measurements that produced large differences on the extrapolated astrophysical S-factors.

I have studied this reaction with two completely different experimental setups characterized by a gas and a solid target, respectively. In particular, an extensive study of the in-beam induced background has been performed to analyze the gas target data, both with ancillary measurements and with GEANT4 simulations. This in-beam induced background has been strongly reduced in the solid target experiment with ^{15}N enriched targets. However, the solid target results are strongly dependent on the target characteristics (stoichiometry and isotopic ratio). As a consequence, I performed a much detailed study of the targets by using the most advanced techniques.

The two experiments are affected by completely different systematic errors and they provide results in excellent agreement with each other. The measured width of the E_R = 312 keV resonance is consistent to results recently published. On the contrary the measured strength of this resonance at its maximum (± 12 % error) is in good agreement with one of the published results but differs substantially, lower by 40%, with the value used by NACRE to evaluate the adopted S-factor. Our data reach much lower energies than in previous experiments covering the energy region where the direct capture contribution dominates the S-factor. The trend of our data shows a factor two lower extrapolation with respect to the NACRE one.

The present results directly affect the production of ^{16}O in nova explosion, reducing the amount of this nucleus by 30%. New nova scenarios have been recently studied for binary systems with low initial metallicity, where the influence of the revised value of ^{15}N(p,γ)^{16}O is now under investigation.

Appendix

Appendix A

Background characterization of the ultra-sensitive in-beam γ-ray spectroscopy facility at LUNA

The aim of the study described in this appendix is to investigate the possibility to measure radiative capture reactions for nuclear astrophysics producing γ-rays at energies below 3 MeV in an underground laboratory. A similar work has been already done for γ-rays above 4 MeV [34]. In this region it is not necessary to strongly shield the detector against laboratory γ-ray background, simply because this background is negligible at LUNA [34], due to the reduced cosmic ray flux. In the γ-spectrum region below 3 MeV the background is dominated by the Uranium-Thorium chains and ^{40}K radioactivity present at the LUNA site and a sophisticated shielding of setup and detector is required.

Recently, the technique of underground in-beam γ-spectrometry has been extended to radiative capture reactions with Q-values below 3 MeV:

- The ^{3}He(α,γ)^{7}Be reaction has been studied at LUNA both by activation [47, 48, 49] and by in-beam γ-spectrometry [49, 50]. This reaction has a Q-value of 1.586 MeV. It controls the flux of ^{7}Be and ^{8}B neutrinos from the Sun [51, 52] and the production of the ^{7}Li in big bang nucleosynthesis [53],

- the ^{12}C(p,γ)^{13}N reaction [54], Q-value 1.943 MeV, important for pre-equilibrium CNO burning [52],

but there are still other important reaction to be studied:

- the ^{12}C(^{12}C,α)^{20}Ne (Q-value 4.617 MeV, main γ-ray energy 1634 keV) and ^{12}C(^{12}C,p)^{23}Na (Q-value 2.241 MeV, main γ-ray energy 440 keV) reactions [55], important for carbon burning in massive stars [56],

- the ^{24}Mg(p,γ)^{25}Al reaction [57], Q-value 2.272 MeV, important for hydrogen burning in massive stars [56] .

Here we concentrate on a typical setup where this reactions could be measured. In particular we study its background: both the natural background, and the in-beam induced background with an intensive α-beam. The setup has been tested in 3 configurations (see next sections) and it has been compared with a low counting level facility present at the LNGS.

A.1 Experimental setup

The setup consist of a windowless, differentially pumped gas target and a shielded HPGe detector. A gas target presents many advantages in respect to a solid one in the measurements of cross sections that change rapidly with the energy and are so small to require many days of beam time to collect a good statistics. A gas target provides an adjustable thickness which is usually smaller than solid target thickness. This gives the possibility to reduce the energetic interval over which the cross section is averaged. A gas target also provides high purity (almost no contaminants) and high stability over long period of measurements. The differentially pumping system has been already described for the ^{15}N(p,γ)^{16}O reaction gas target experiment. The same pumping system has been used with this new setup shown in Fig. A.1. The ^{3}He(α,γ)^{7}Be was studied at unprecedented low energies with this setup [47, 48, 49, 50]. The HPGe detector is a Canberra ultra-low background p-type coaxial detector with 137% relative efficiency. The crystal is connected to the dewar by a 25 cm long cold finger and it is oriented at 90° with respect to the cold finger (golf club configuration). In this way the crystal can be shielded by lead avoiding the direct line of sight from the cryostat. The detector end-cap is made by oxygen-free high conductivity (OFHC) copper. The ion chamber is made by OFHC copper, a 60 cm long with a 12 cm by 11 cm area. The beam can enter in ion chamber through disk-shaped water-cooled collimator with 7 mm inner diameter. The end-cap of the calorimeter stops the beam and it works as the hot surface of the calorimeter itself. The way how a calorimeter measures the current has been explained in sec. 2.3.1. The shielding is made of several layers and it surrounds detector and target chamber, with the exception of the two holes for beam pipe and for the beam calorimeter. It is designed in such a way that germanium crystal of the detector is typically shielded by 4 cm copper and 25 cm lead (Fig. A.1). The innermost shielding layer surrounding the detector is made of OFHC copper bricks machined to the shape of the detector (only 1-2 mm of space left free). A 3 cm thick OFHC copper plate above the target chamber carries the weight of the upper half of the lead shield (Fig. A.2). The copper absorbs the low energy γ-rays due to ^{210}Pb. The remainder of the shield is made of lead bricks with low ^{210}Pb content (25 Bq/kg ^{210}Pb, supplied by JL-Goslar, Germany) and it is 25 cm thick. The lead bricks were cleaned with citric acid before being mounted, in order to remove any possible accumulated dust and surface oxidation. The presence of radon daughters in the shielding is avoided mounting an anti-radon box made in plexiglass. It is flushed by nitrogen evaporated from the HPGe detector's dewar and kept at slight over pressure. The gas volume inside the anti-radon box is about 4 liters.

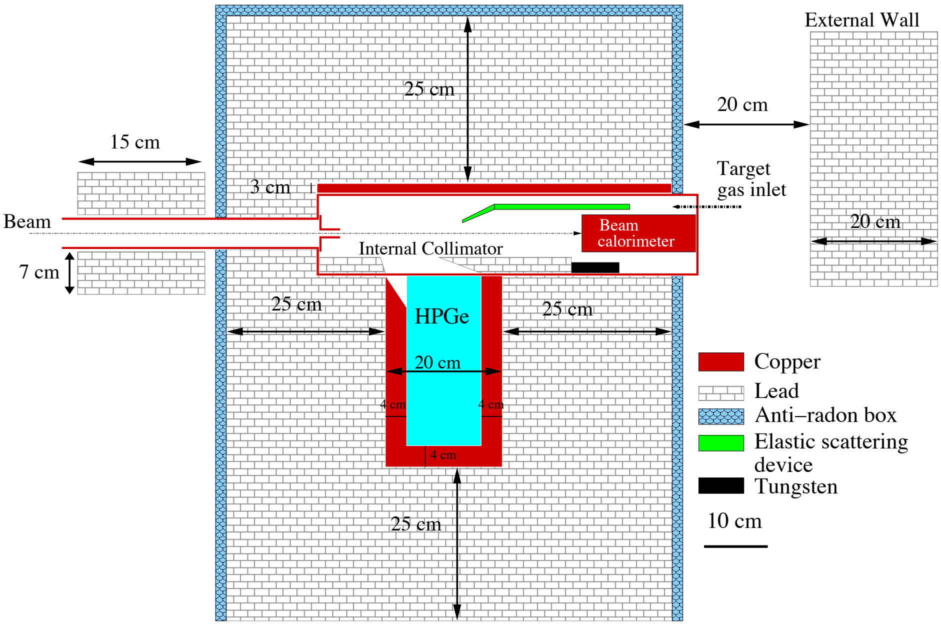

Figure A.1: *Schematic view of the experimental setup C (complete shielding).*

Outside the anti-radon box, a 15 cm thick wall of lead is placed upstream the target chamber. In addition a 20 cm thick wall of lead is placed behind the end of the calorimeter (see Fig. A.1). This wall is called ”external wall”

Inside the target chamber, the γ-rays emitted within the gas target are collimated by 3 cm thick trapezoidal-shaped lead bricks that also serves as additional shield. A tungsten shield is also placed to absorb the possible activities from the calorimeter. A device to detect the elastic scattered α particles with a silicon detector in order to study the effective target gas density and gas contaminations is mounted inside the chamber [58]. In order to limit possible γ-emissions, the elastic scattering device has been made of Delrin.

The intrinsic background of the setup was studied in three experimental configurations called setups A, B and C. All these configurations were placed in the same LUNA2 site at LNGS:

A: HPGe detector without any shield.

B: HPGe detector with complete shield except for

- inner trapezoidal lead collimator,
- 20 cm lead wall behind the calorimeter and
- anti-radon box.

C: HPGe detecor with complete shield (Fig. A.1).

For comparison also a fourth experimental configuration is considered, here called setup LLL: a HPGe detector of similar size (125% relative efficiency) and equal geometry to the present one. It is shielded with 25 cm low-background lead including an inner of quasi-^{210}Pb-free lead from a sunken Roman ship and it has a highly efficient anti-radon box [59]. Setup LLL is dedicated to low level counting measurements on samples and for this reason it does not have any entrance holes in the shielding as in the in-beam setups A-C.

Setup C was used for the in-beam γ-spectroscopic part of the LUNA ^{3}He(α,γ)^{7}Be study [49, 50]. Setup LLL has been used to measure the ^{7}Be activity counting in that same study [47, 48, 49, 50].

A.2 Laboratory γ-ray background studies for E_γ <3 MeV

The background spectrum was acquired for several days in each configuration and the results for the main peaks in the spectrum were compared. Also the spectrum taken with an inert sample (^{4}He + ^{4}He irradiated OFHC copper [47]) on detector LLL is shown. Comparing the unshielded setup A with the shielded setup B (Fig. A.3, a reduction of three

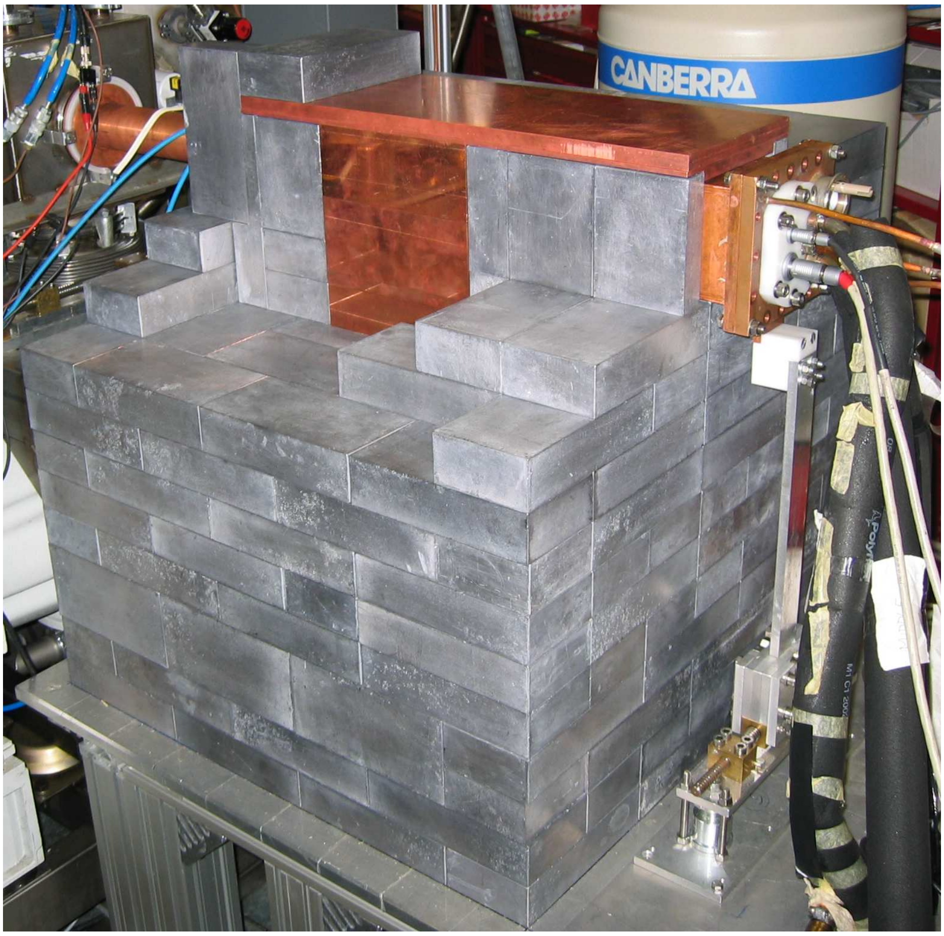

Figure A.2: *Photo taken during the construction of the shield. The lower half of the lead shield is already complete, as well as the copper shield for the detector and the copper plate above the target chamber. The back plate and connectors of the beam calorimeter are visible in the upper right corner. The copper tube for the beam inlet is seen in the upper left corner. The upper half of the lead shield was not yet installed when the photo was taken.*

E_γ [keV]	511	609	1460	1730	1764	2615
Exp A (no beam)	762±4	3729±6	4870±6	246±2	1346±3	1325±2
Exp B (no beam)	0.60±0.13	3.9±0.2	0.93±0.11	0.18±0.06	1.08±0.10	0.42±0.06
Exp B′ (α-beam)	1.74±0.32	4.6±0.4	0.51±0.17	0.32±0.11	1.06±0.19	0.55±0.11
Exp C (no beam)	0.09±0.04	0.27±0.03	0.42±0.03	0.038±0.010	0.098±0.014	0.12±0.02
Exp C′ (α-beam)	<0.33	0.20±0.09	0.40±0.09	<0.034	0.36±0.07	0.07±0.03
Setup LLL	<0.04	0.055±0.018	0.098±0.018	<0.011	0.026±0.008	0.016±0.005

Table A.1: *Counting rate in counts/hour for selected γ-lines, in setups A-C at LUNA. For comparison, the corresponding numbers are also given for setup LLL at the LNGS low level laboratory. Upper limits, where applicable, are given for 2σ confidence level.*

orders of magnitude in the γ-ray continuum below 2615 keV is observed and the summing lines above the 2615 keV ^{208}Tl line are no longer evident (the 2615 keV line is the highest in the γ-ray spectrum). In addition, the counting rate for the most important single γ-lines is reduced by three orders of magnitude or more (tab. A.1)

Improving the shielding from setup B to the final setup C yield up to another order of magnitude suppression in the γ-continuum below 2615 keV. The main lines we checked were the ones from the ^{40}K (1461 keV), the ^{208}Tl (2615 keV) and the lines from ^{214}Bi, the daughter of radon (609, 1120, 1730 and 1764 keV). The ^{40}K is present in the construction materials and the ^{208}Tl is a nuclide produced in the thorium chain present in the wall of the

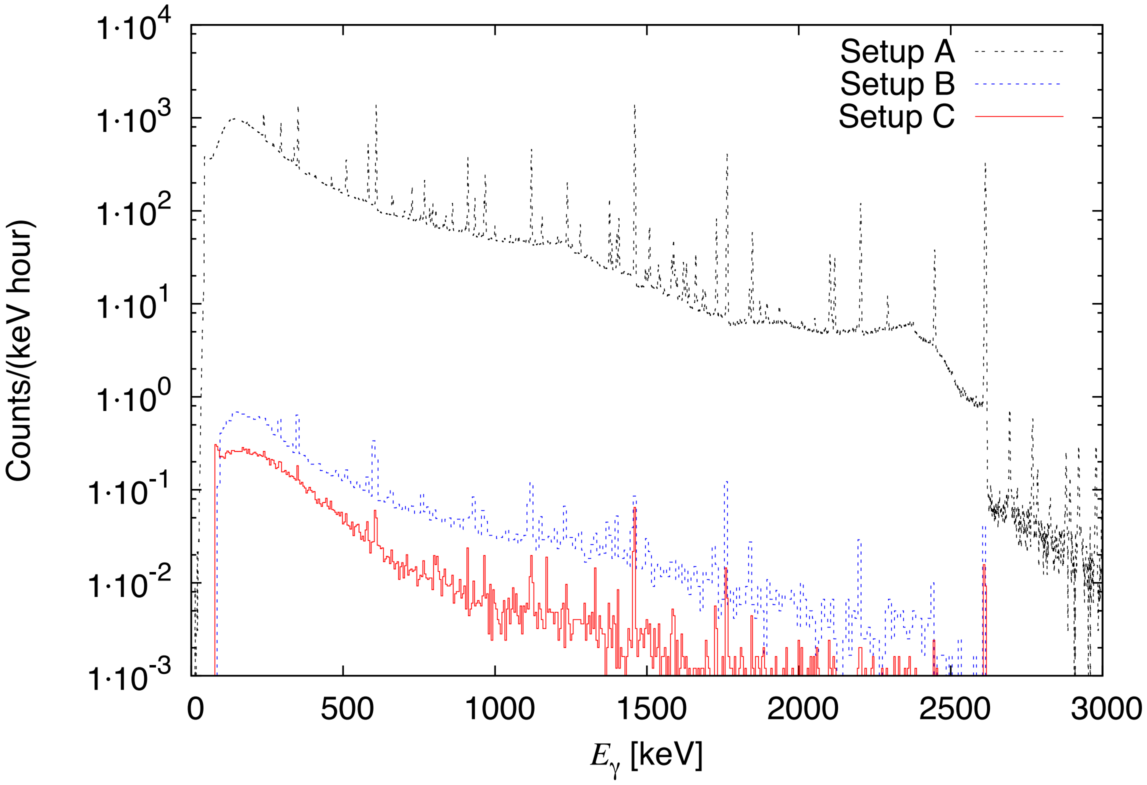

Figure A.3: *Laboratory γ-ray background spectra for setups A (black dashed line), B (blue dotted line) and C (red full line). See table A.1 for the counting rate of the selected lines and table A.2 for the assignment of the lines evident in spectrum C.*

LNGS tunnel. The γ-ray from this two nuclides are already reduced by the shield provided by the setup B. They are suppressed from setup B to setup C by a factor 2 for the 1461 keV line and by a factor 3 for the 2615 keV line. The 15 cm thick lead wall behind the calorimeter and the internal lead collimator improve the effective shielding thickness on a limited solid angle; hence the limited improvement of only a factor 2-3. The lines from the ^{214}Bi are reduced by a factor 10 from setup B to setup C. This is due to the operation of the anti-radon box that reduces the amount of ^{222}Rn ($t_{1/2}$ = 3.8 d, progenitor of ^{214}Bi) present in the remaining air pockets near the detector.

In the case of setup C the reduction for the 511 keV annihilation line is the same as the ^{214}Bi lines and it is just barely significant at 2σ level. The remaining γ-lines evident in spectrum C (Fig. A.3) can all be traced back to natural radionuclides present in the laboratory, detector and radon gas (tab. A.2). No neutron induced (n,γ), (n,n$'\gamma$) or activation lines [60] can be identified in spectrum C after 21 days counting time.

A comparison has been done between setup C and setup LLL in order to judge the quality of the background suppression in the in-beam facility (Fig. A.4). The spectra have not been corrected for the slight different size of the crystals: 137% in setup A-C and 125% in setup LLL. Since the modern lead has an higher amount of ^{210}Pb with respect to the Roman ship lead used for the inner shielding of setup LLL the γ-ray continuum particularly below

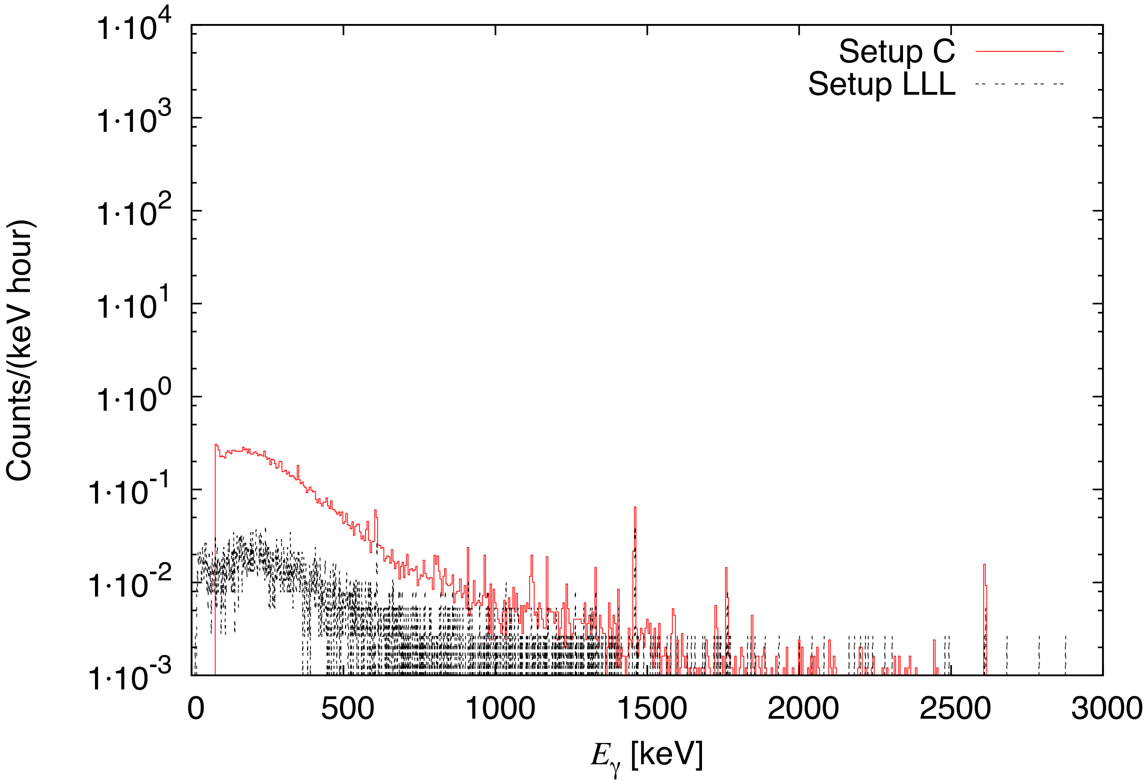

Figure A.4: *Laboratory γ-ray background spectra for setups C (red full line, same as in Fig. A.3) and inert sample counted in setup LLL (black dashed line). See table A.1 for the counting rate of the selected lines and table A.2 for the assignment of the lines evident in spectrum C.*

E_γ [keV]	Nuclide	Source
352	^{214}Pb	Radon gas
511	$e^+ e^-$	β^+ emitters
583	^{208}Tl	Thorium chain, tunnel walls
609	^{214}Bi	Radon gas
815	^{214}Bi	Radon gas
912	^{228}Ac	Thorium chain, tunnel walls
969	^{228}Ac	Thorium chain, tunnel walls
1120	^{214}Bi	Radon gas
1170	^{60}Co	Detector contamination
1238	^{214}Bi	Radon gas
1333	^{60}Co	Detector contamination
1377	^{214}Bi	Radon gas
1408	^{214}Bi	Radon gas
1460	^{40}K	Potassium in construction materials
1588	^{228}Ac	Thorium chain, tunnel walls
1701	^{228}Ac	Thorium chain, tunnel walls
1730	^{214}Bi	Radon gas
1764	^{214}Bi	Radon gas
1847	^{214}Bi	Radon gas
2448	^{214}Bi	Radon gas
2615	^{208}Tl	Thorium chain, tunnel walls

Table A.2: *List of γ-lines evident at 2σ level or better in the laboratory background of setup C (fig. A.3).*

0.5 MeV is up to one order of magnitude higher in setup C when compared to setup LLL. This continuum is mainly produced by the bremsstrahlung photons emitted by electrons created in ^{210}Bi β^--decay (Q-value = 1.16 MeV). The higher counting in the lines reported in tab. A.1 of setup C in respect to setup LLL are ascribed to the inevitable hole for the beam pipe, which leads to a small window of not optimally shielded solid angle.

A.3 γ-ray background induced by the α-beam

Two experiments have been performed using an α-beam. The first experiment was performed with setup B bombarded during 47 hours with a ^{4}He$^+$-beam of E_α = 350 keV and 110 μA intensity from the LUNA2 accelerator. The gas in the target chamber was evacuated to better than 10^{-3} mbar during the experiment. The resulted spectrum is reported in Fig. A.5. The main difference between the in-beam spectrum and the setup B spectrum is that the 511 keV lines is higher by a factor 3. This can be explained assuming some creation of β^+-emitters by the α-beam. Due to the absence of other new γ-lines in the spectrum, it is impossible to assign a particular nuclide as the supposed β^+-emitter. However, it should be noted that the in-beam 511 keV counting rate is still 400 times lower than in the unshielded case of setup A.

An other in-beam experiment was performed with the chamber filled with 0.7 mbar ^{4}He gas (chemical purity 99.9999%). The α-beam was set with an energy E_γ = 400 keV and 240

μA intensity for 62 hours long irradiation [49, 50]. As in the previous case the experimental spectrum does not show any additional γ-lines with respect to the corresponding laboratory background (Fig. A.5).

A.4 Feasibility of cross-section measurements at LUNA

In order to evaluate the feasibility of in-beam cross section measurements, we have decided to calculate the hypothetical cross-section $\sigma_{S=N}(E_\gamma)$ for which the expected "signal" S would be equal to the measured "noise" N in the acquired spectra. This cross section was calculated for the main reactions with Q-values lower than 3 MeV or with γ-rays in this region of the γ-spectrum. These γ-rays can be produced by direct capture reaction or by the decay of excited compound nuclei. The laboratory background, N, was evaluated for a 30 keV wide region of interest centered at the γ-ray energy produced by the selected reaction [E_γ - 15 keV; E_γ + 15 keV]. This choice is valid for primary γ-rays from capture into a particular level in the compound nucleus, with a target thickness equivalent to 30 keV energy loss by the primary beam. For light target nuclei like ^{3}He and ^{2}H, the Doppler shift for γ-rays emitted before or after the detector makes it necessary to maintain a 30 keV region even if the energy loss in the target is lower. For secondary γ-rays emitted by the excited nuclei at rest the detector resolution should be adopted instead of 30 keV, so we can consider our

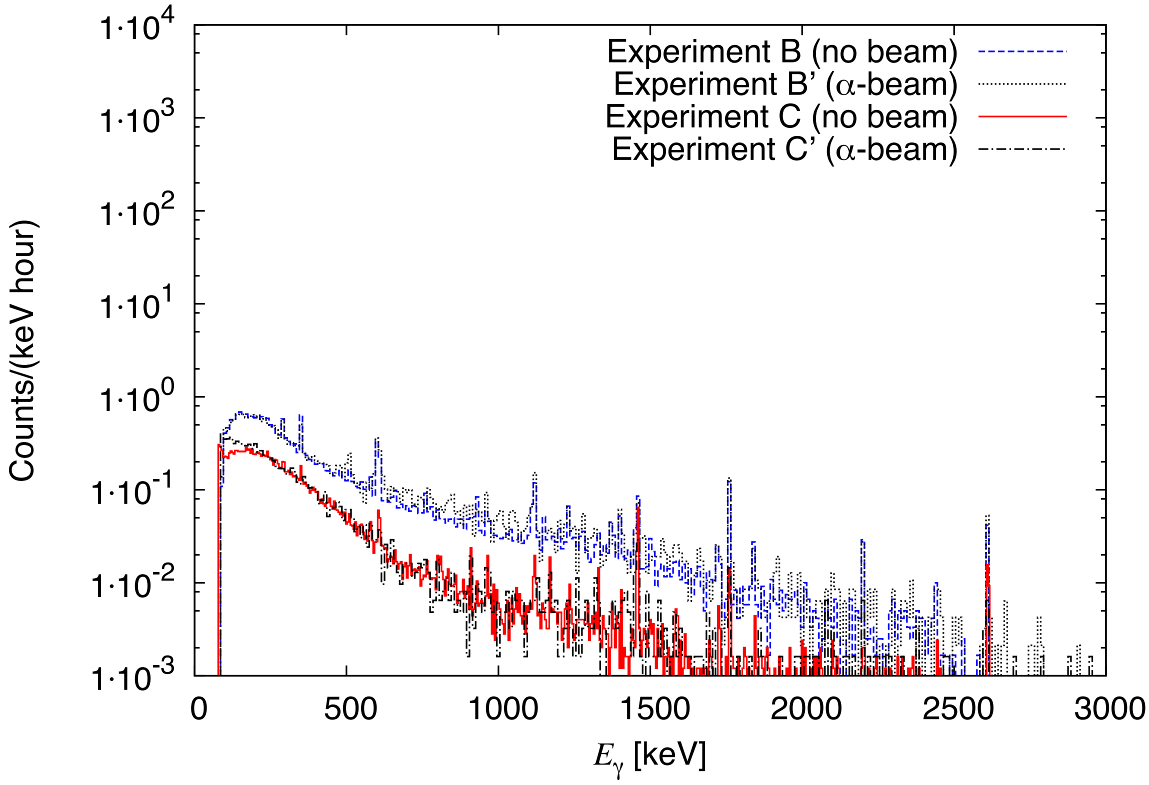

Figure A.5: *Comparison of offline and in-beam γ-spectra: setup B, offline (blue dashed line) and with α-beam (black dotted line). Setup C, offline (red full line) and with α-beam (black dot-dashed line).*

solution as an upper limit. The cross-section was evaluated as:

$$\sigma_{S=N}(E_\gamma) = \frac{\mathrm{LabBG}(E_\gamma)\cdot 30\mathrm{keV}}{\epsilon_\gamma(E_\gamma)\cdot 6\cdot 10^{17}\frac{\mathrm{atoms}}{\mathrm{cm}^2}\cdot 250\mu\mathrm{A}\cdot 3600\mathrm{s}} \tag{A.1}$$

Here, LabBG(E_γ) is the laboratory background counting rate per keV and hour plotted in Fig. A.3, for setup B or C, respectively. The γ-ray detection efficiency in the present geometry is $\epsilon_\gamma(E_\gamma)$ (0.4% at E_γ = 1.33 MeV). An effective target thickness of $6{\cdot}10^{17}$ atoms/cm^2 is assumed, corresponding, *e.g.*, in the ^{3}He(α,γ)^{7}Be case to 9 keV energy loss in the target [47, 48]. This is a typical value for this type of experiments. Increasing the target more than this does not increase the relative yield any further due to the steep decline of the Coulomb barrier penetrability. As ion beam intensity we used the typical LUNA2 value of 250 particle-μA and the branching ratio of 1 was assumed for each γ-ray of interest.

We studied the sensibility of our facility for some of the most interesting reactions for nuclear astrophysical purposes. The ^{2}He(α,γ)^{6}Li and the ^{3}He(α,γ)^{7}Be are important for the ^{6,7}Li in the Big Bang Nucleosynthesis ($T_9 \approx$ 0.3-0.9; T_9 stands for the temperature in 10^9 K). The present sensitivity is sufficient for an experimental study directly at the Gamow energy for these reactions (table A.3). The CNO cycle reaction ^{12}C(p,γ)^{13}N at temperature typical for hydrogen shell burning is an analogous case; also here a direct study is feasible.

Two important reactions for the carbon burning can be studied, but not a the Gamow peak. The ^{12}C(^{12}C,α)^{20}Ne and the ^{12}C(^{12}C,p)^{23}Na were already measured on the Earth surface for the resonant cross section contribution. The non-resonant cross-section was estimated about four orders of magnitude below the present $\sigma_{S=N}$ (table A.3).

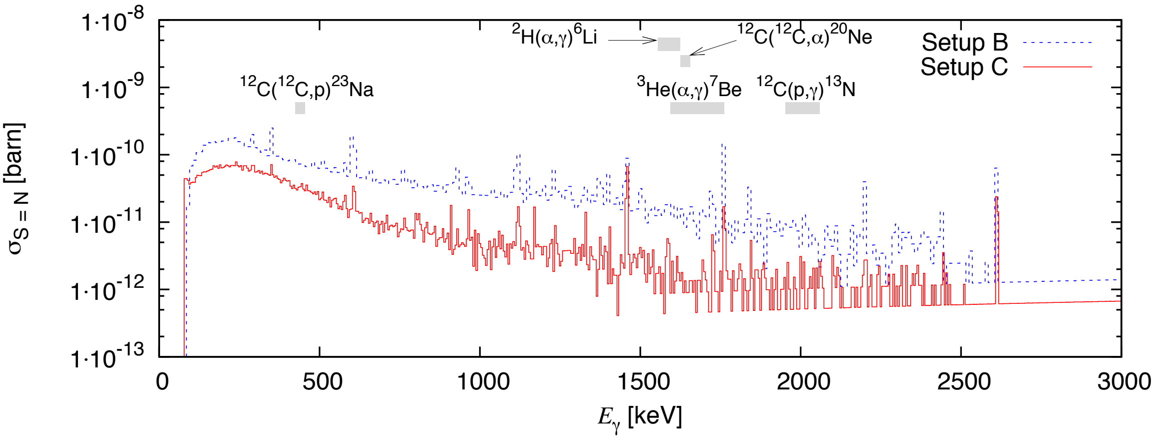

Figure A.6: *Cross-section $\sigma_{S/N=1}(E_\gamma)$ defined by eq. (A.1), for setups B (blue dashed line) and C (red full line). The γ-ray energies of interest for the nuclear reactions listed in tableA.3 are indicated by gray bars.*

Reaction	Scenario	T_9 [10^9 K]	E_G [keV] [keV]	$\sigma(E_{Gamow})$ [barn]	E_γ [keV]	$\sigma_{S=N}$ [barn]
$^2H(\alpha,\gamma)^6Li$	Big-bang nucleosynthesis	0.3	96	$2 \cdot 10^{-11}$	1570	$1.7 \cdot 10^{-12}$
$^3He(\alpha,\gamma)^7Be$	Big-bang nucleosynthesis	0.3	160	$1 \cdot 10^{-8}$	1746	$1.3 \cdot 10^{-12}$
	Proton-proton chain in the Sun	0.016	23	$4 \cdot 10^{-17}$	1609	$1.8 \cdot 10^{-12}$
$^{12}C(p,\gamma)^{13}N$	CNO cycle burning in the Sun	0.016	25	$2 \cdot 10^{-17}$	1968	$1.1 \cdot 10^{-12}$
	Hydrogen shell burning	0.085	76	$3 \cdot 10^{-11}$	2019	$1.2 \cdot 10^{-12}$
$^{12}C(^{12}C,\alpha)^{20}Ne$	Core carbon burning	0.5	1500	$2 \cdot 10^{-16}$	440	$3 \cdot 10^{-11}$
$^{12}C(^{12}C,p)^{23}Na$	Core carbon burning	0.5	1500	$2 \cdot 10^{-16}$	1634	$1.6 \cdot 10^{-12}$

Table A.3: *Reactions of astrophysical interest discussed in the text. The relevant astrophysical scenario, typical temperature T_9 and corresponding Gamow energy [56] E_{Gamow} are also given. The expected cross section at E_{Gamow} has been estimated. The relevant γ-ray energy is also shown. For the case od setup C, the cross section $\sigma_{S=N}(E_\gamma)$ has been calculated following eq. (A.1).*

For the present estimates (Fig. A.6, table A.3), the ion beam induced background is assumed to be negligible at the γ-ray energies of interest. Whether or not this assumption is valid depends on the precise experimental setup target, beam and beam energy to be used. This assumption was checked for α-beam in the previous section and for proton beam in previous experiment [34], but should be checked in each new experiment. In summary, for the present LUNA2 accelerator and the ultra-sensitive setup described above, including a single large HPGe detector, it has been shown that cross-sections of typically 1-10 pbarn can well be measured. As shown in table A.3 the precise value of the minimum measurable cross-section depends on the γ-ray energy. The present results can be extended to the proposed underground accelerator laboratories outside the LNGS facility [61, 62, 63] evaluating the precise background conditions at those sites.

Appendix B

Target measurements excluded from the target analysis

All the possibilities to investigate the target properties have been studied, since targets are one of the most important component of the experiment. In this appendix I will discuss two additional methods to investigate the element concentration in the target. The former is the study performed by using deuteron induced nuclear reaction on the atoms of the sample and the latter is the Secondary Mass Neutral Spectrometry (SNMS). Nuclear reactions were tested at the Tandetron accelerator in Seville during a shift dedicated to measurements of nitrogen in several samples (mainly for aerosol analysis). The difficulties to have enough time as user at this accelerator and the systematic uncertainties of this type of measurement make unfruitful this method for our analysis. The SNMS has been done in Debrecen at the ATOMKI institute, but the results of this technique disagree with the results from all the other experiments we have done on the targets. For this reason the data are still under analysis together with the Hungarian group in order to understand the discrepancies.

B.1 Nuclear reaction induced by deuteron on nitrogen

The nuclear reactions are not sensitive to the roughness of the targets and they can be a good candidate for the stoichiometry analysis and for evaluating the isotopic ratio in the nitrogen samples, since they measure an average of the concentration over the beam size. Nuclear reactions are not influenced by the atomic forces or by the target production technique. The reactions induced by deuteron have high cross section and high Q-value and they could be utilized to evaluate the nitrogen concentration in the sample.

The cross section for (d,α_0) or (d,α_1) reactions on nitrogen isotopes are measured in literature at the typical angle of 55° and are well known in literature although with a precision of few percent.

A test to use this type of nuclear reactions has been done at the Tandetron accelerator at the Seville University. The deuterium beam was provided by the Tandetron accelerator with a current small enough in order not to have a destructive effect on the target. The setup was made by a cylindrical target chamber with the possibility to install many different silicon detectors inside at different angles. The target holder can sustain many targets with the dimension of a circle or half of a circle. Thank to this support the target can be tilted and moved along the axis perpendicular to the direction of the beam in order to scan in different position of the target. A quartz, placed at the center of the target holder, was used to fix the beam position in respect to the target position. The low fluorescence signal of the beam on the target and the low resolution of the camera avoided the possibility to measure the precise position of the target in respect to the beam axis. Also the target holder was not made for the LUNA targets and we did not have an exact evaluation of the detector solid angle with high precision. A camera has been installed inside the target chamber to check online the correctness of the target position. A silicon detector with an active surface of 300 mm^2 placed at a distance from the target of 60 mm at the angle of 55° was used to detect the α-particles. This detector covered approximately a solid angle of 0.082 sr. The beam energy was 1.402 MeV. At this energy the cross section for the ^{14}N(d,α)^{12}C (Q = 13.57 MeV) is $\sigma_{d+^{14}N}$ = 0.86±0.03 mbarn while the cross section for the ^{15}N(d,α)^{13}C reaction (Q = 7.69 MeV) is $\sigma_{d+^{15}N}$ = 1.94±0.03 mbarn. The current was fixed at 7 nA and set by a chopper that integrate also the charge. This current was high enough to have a good statistic in most of the samples and the target does not suffer from degradation due to the beam intensity. The deuteron induced nuclear reactions were used on a target made in Karlsruhe. This target was sent after this measurements to Debrecen in order to perform the SNMS measurements. We did not use the data taken on this target for the analysis of the S-factor since the SNMS is a destructive technique and we did not perform the resonance scan before. As in the case of the resonance scan performed in Dresden (sec. 4.2.3) we analyzed both the "virgin" area

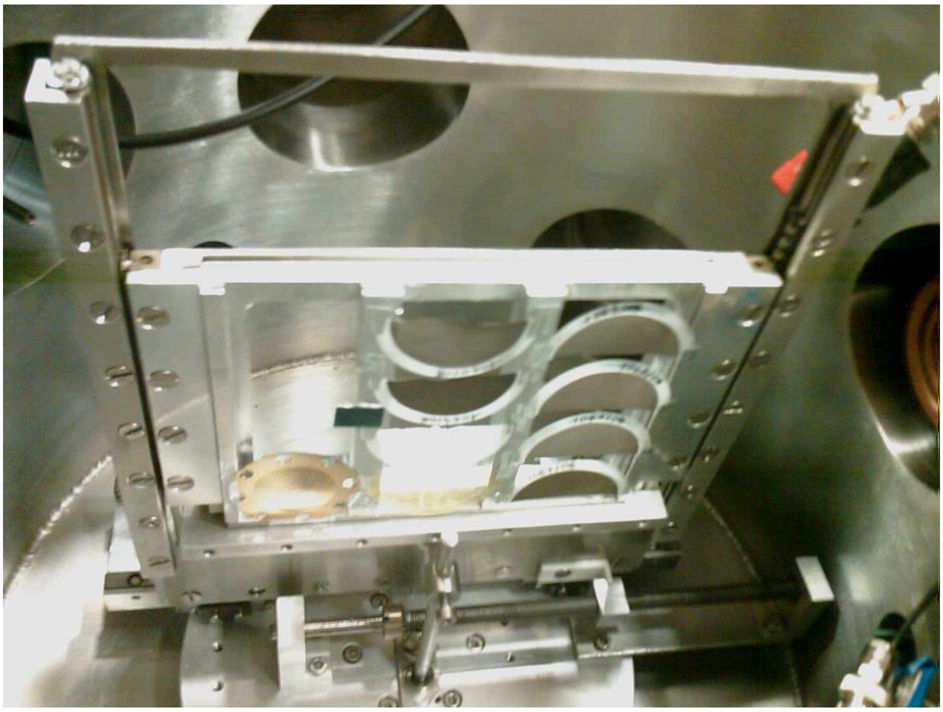

Figure B.1: *Detail of the target holder. On the left, the LUNA target is placed.*

and the "beamspot" area in order to check the sensitivity of the methods. Since the Q-values for ^{14}N and ^{15}N are different by about 6 MeV the peaks due to the two different reactions are well separated as shown in Fig. B.2. Due to the poor concentration of ^{14}N in the sample, the statistic in the peak at 10 MeV is not enough to have a clear evaluation of this isotope. In the two spectra in Fig. B.2 two peaks are evident: one produced by the ^{15}N(d,α_0)^{13}C reaction at 4.5 MeV and another by the ^{15}N(d,α_1)^{13}C reaction at 6 MeV. Only the second peak was analyzed, because it was well separated from the peak produced by the Ta(d,d)Ta elastic scattering reaction. The large peak from 2 MeV (the ADC threshold value) to 4 MeV is due to the elastic scattering of the deuterons on the tantalum backing. This is common in the case of Rutherford backscattering on backing made of high Z element. A mylar foil was placed in front of the detector in order to reduce the energy of the elastic scattered deuterons. Reducing also the power supply of the silicon detector we avoided to acquire all the scattered deuterons reducing the pile up effect in the spectrum and the dead time to 10% (before it was higher than 80%). The mylar foil and the power supply decreasing had an effect on the peak resolution. However, no other source of contamination has been seen in the spectra and the peaks from nitrogen are quite well separated. A difference in the amount of ^{15}N was measured between the "virgin" area and the "beamspot" area. The ^{15}N reduction in the "beamspot" area, in respect to the "virgin" one, was evaluated to amount to about 40% with an error of 7%. This is more than expected from the reference points but it could be due to the beamspot dimensions, which were different for the LUNA2 beamspot. The ratio ^{14}N/^{15}N was evaluated to be about the 5% (30% uncertainty), close to the same value obtained with the resonance scan technique on the resonance of the ^{14}N(p,γ)^{15}O reaction. We

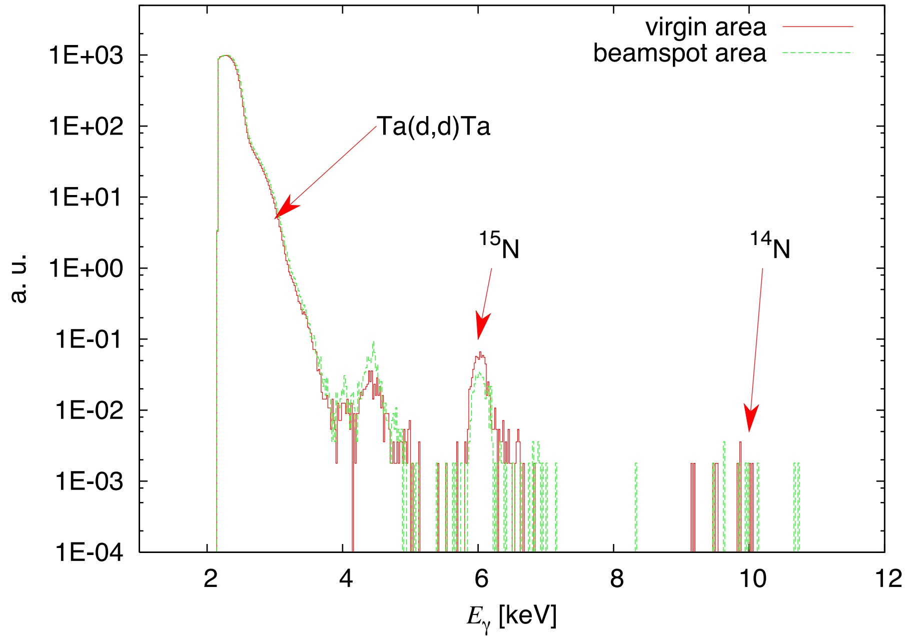

Figure B.2: *The silicon detector spectra are reported. In red the measurement for the "virgin" area spot and in green for the "beamspot" area. The analyzed peak for ^{14}N(d,α_0)^{12}C and ^{15}N(d,α_0)^{13}C are underlined in the peak together with the peak due to the elastic scattering of deuterium on the tantalum backing.*

did not calculated any absolute value, since the solid angle was not well measured. This test was done inside a shift dedicate to a measurements of samples related to the aerosol studies and we suffered for the problem of setup optimization and lack of beam time. The obtained values with the nuclear reaction technique are quite well in agreement with the result obtained with the ERD and resonance scan measurements. Unfortunately the deuterons induced nuclear reaction cannot give us an information on the stoichiometry of the LUNA target (i.e. the titanium abundances) and it is impossible to investigate the target profile. An absolute information about the nitrogen isotopic ratio could be calculated with this nuclear technique only after several hours of measurements. In addiction the used setup should be improved in order to reduce the systematic uncertainties also for an absolute measurements. The nuclear cross sections are measured with an uncertainty of few percent in each experiment. We took the measured cross section from the experiments of Gurbich [64] and Vickridge [65]. There are also some differences between the results of different experiments and this fact limits the final uncertainty also if we had enough time to increase the statistic. In this view we decided not to use this technique in our target analysis, but this method could be very useful in other experiments particularly if it were possible to use a standard as reference for the concentration.

B.2 Secondary Neutral Mass Spectrometry

The Secondary Neutral Mass Spectrometry (SNMS) has been done at the Department of Solid State Physics, University of Debrecen. The aim was to find a precise and independent value for the isotopic ratio and the stoichiometry ratio of our target.

This technique is particularly useful for:

- analysis of conducting and insulating materials
- depth profiling for scientific an industrial applications
- impurity and contamination analysis in quality control
- analysis of buried interfaces
- environmental analysis

and it is ideally suited to quantitative elemental and depth profiling analysis of any material. It is not affected by matrix effect and by the influence due to preferential sputtering. It is also possible to make a strict separation between the sputtering of particles and following ionizations.

In this technique the sample is bombarded with rare gas ions (i.e. Ar, Kr, Ne, etc) with an energy in a range of 0.5 keV to 5.0 keV. This leads to sputtering of atoms and molecules from the sample, which leave the surface as shown in Fig. B.3. The particles, sputtered from the sample, are ions and neutral atoms. The neutral atoms are ionized after the sputtering and then detected. The probability to sputter ionized atoms can vary between 10^{-5} to 10^{-1}

and depends strongly on the surface composition (matrix effect) so the detection of also the neutral atoms reduces the sensitivity to the surface composition and allow a much better quantitative estimate of stoichiometry. The concentration of the elements could be evaluated over the sample profile using a correlation between the sputtering time and the thickness of the sample.

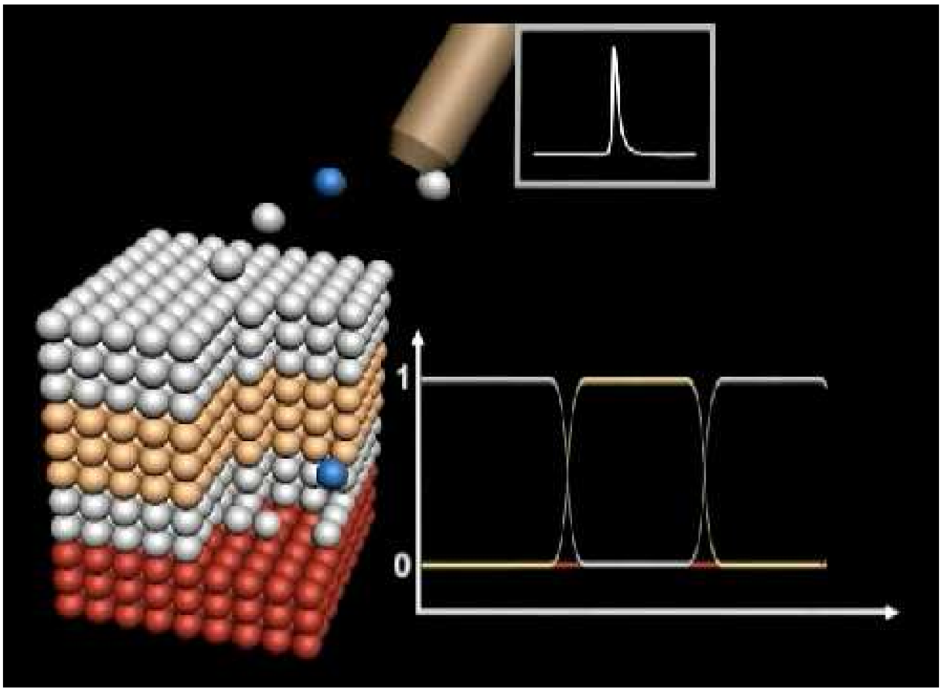

Figure B.3: *Schematic view of the SNMS process. The blue ions sputter the ion from the sample and the sample profile will be constructed.*

In Fig. B.4 there is the result of SNMS on one target of the Karlsruhe set. It is possible to determine the concentration for all the elements in the target: ^{14}N, ^{15}N, Ti and Ta. The rise of the tantalum edge represents the contact surface between the target deposition and the backing. On the left graph there is the profile scan for the "virgin" area and it is possible to distinguish the roughness of the target from the irregularities of the plateau. This is due to the roughness of the backing since the titanium nitride deposition should be quite homogeneous in reactive sputtering. From the right graph we can estimate the deterioration of each element and the changing of the isotopic ratio ^{14}N/^{15}N during the irradiation at LUNA. There is also an evident diffusion of nitrogen in the tantalum backing. This diffusion does not affect the result of the analysis since the cross section drops very steeply with the energy and so the deeper layers of the target do not contribute to the measured yield. However, it seems very difficult to be justified even by the porosity of the backing material. As a matter of fact the beam heating induced by the beam on the backing increases the porosity of the tantalum and allows the nitrogen movement into the tantalum layer. Looking the spectrum in Fig. B.4 the intrusion affects only the nitrogen and not the titanium and this is also another strange effect.

Summarizing, the results of the SNMS analysis report a stoichiometry ratio of Ti/N =

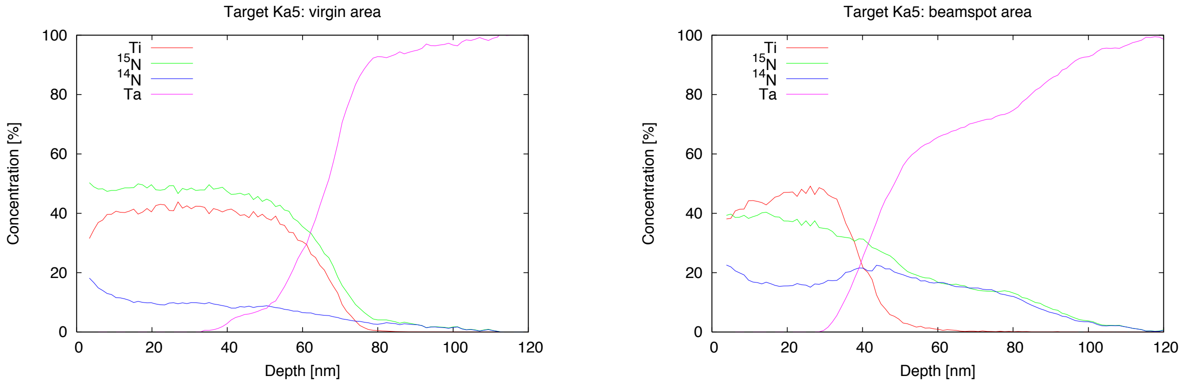

Figure B.4: *The obtained profiles for the target Ka5 with the SNMS technique. In the left side there is the profile for the "virgin" area and on the right picture there is the "beamspot" measurements. The long nitrogen tail in the tantalum backing is evident.*

0.67 and a isotopic ratio of $^{15}N/N_{tot} = 80\%$. These results are completely different from the reported results of the ERD technique and of the resonance scans performed at LUNA with the BGO. These results are also in disagreement with the nominal value quoted by the producer of the targets. For these reasons this technique has been excluded from the analysis. We are still instigating the SNMS analysis in order to understand the disagreement. One possible reason could be the extremely difficult nitrogen post ionization. If the post ionization factor has been overestimated or underestimated the real amount of nitrogen could be very different from SNMS results. In SNMS measurements the statistic was very poor and a correction on the ionization factor could change drastically the final absolute result. Unfortunately this technique has not been performed directly by the LUNA collaboration and so we only could try to stimulate a discussion with the specialists of this technique.

Appendix C

Laboratory background measurements at different sites

The background characterization of the underground sites is important in order to study the possibility to use these sites to install low level counting facilities. Each type of experiment needs specific level of background in order to effectively performe its research program.

A large sodium iodide detector (NaI) has been used to measure the natural background at three different sites characterized by different depths. In recent years the results obtained by LUNA on the p-p chain and CNO cycle have shown the advantages of running nuclear physics experiments in a low background environment. As a consequence, an underground few MV accelerator is now demanded to study the key reactions of the helium burning. In particular there is great interest in ^{12}C(α,γ)^{16}O, the Holy Grail of the nuclear astrophysics, ^{13}C(α,n)^{16}O and ^{22}Ne(α,n)^{25}Mg, the reactions which produce inside stars the neutrons responsible for the s-process.

LNGS would be the best solution for the installation of a new in-beam low counting facility thanks to its very low background and to the existing experties. In this appendix we have investigated two additional underground laboratories at shallow depths: the Monte Soratte bunker and the Felsenkeller laboratory. In particular, we have done a comparison of the background of this two sites with respect to LNGS.

The same detector was placed in the three laboratories. For the comparison mainly two different regions of the γ-spectrum has been investigated as explained below.

C.1 Detector

The digiBASE is a 14-pin photomultiplier tube base for gamma-ray spectroscopy applications with NaI(Tl) scintillators detector. It combines a miniaturized preamplifier and detector an high voltage supply (0 to +1200 V bias) with a digital signal processing and multichannel analyzer. Using the digiBASE the NaI detector can be connected directly to the PC used for the acquisition. The software to control the digiBASE is the MAESTRO-32 MCA emulation code. Using the MAESTRO-32 the HV of the detector could be provided and all parameter for the amplification of the signal can be set. The internal ADC of the digiBASE has 1024 channels and both the lower and upper threshold can be adjusted by the user. The amplification gain was set in order to have 16 MeV wide spectrum. The NaI detector is a 10x10x40 cm parallelepiped, with a volume of 4 liters.

C.2 The Monte Soratte Bunker

The Monte Soratte Bunker is located close to S. Oreste village near the A1 highway. It is at a distance of about 40 km from Rome. The bunker was built in 1937-1939 and conceived as a government war refuge. The project was abandoned after the second world war and the bunker was left empty until the sixties. In this years the NATO decided to restart the construction of the refuge for anti-nuclear purposes. Three main halls were constructed, but not finished. Recently the Italian Defense Department dismissed the bunker and now it is owned by S. Oreste village. Some ex-military barracks are under reconstruction for civil and touristic purposes.

The bunker is about 420 m above the sea level and covered by about 100 - 120 m of rock that corresponds to 250 - 300 m.w.e. The main halls are about 60 m long, 8 m wide and 8 m high. The background measurements were done in the second main hall, because it was the one with more rock shielding on top as shown in the map reported in Fig. C.1.

The natural background has been investigated for a total of three days with the DIGIBase NaI setup both outside and inside the bunker in order to compare the muon flux reduction of the rock (the altitude modifies the muon flux).

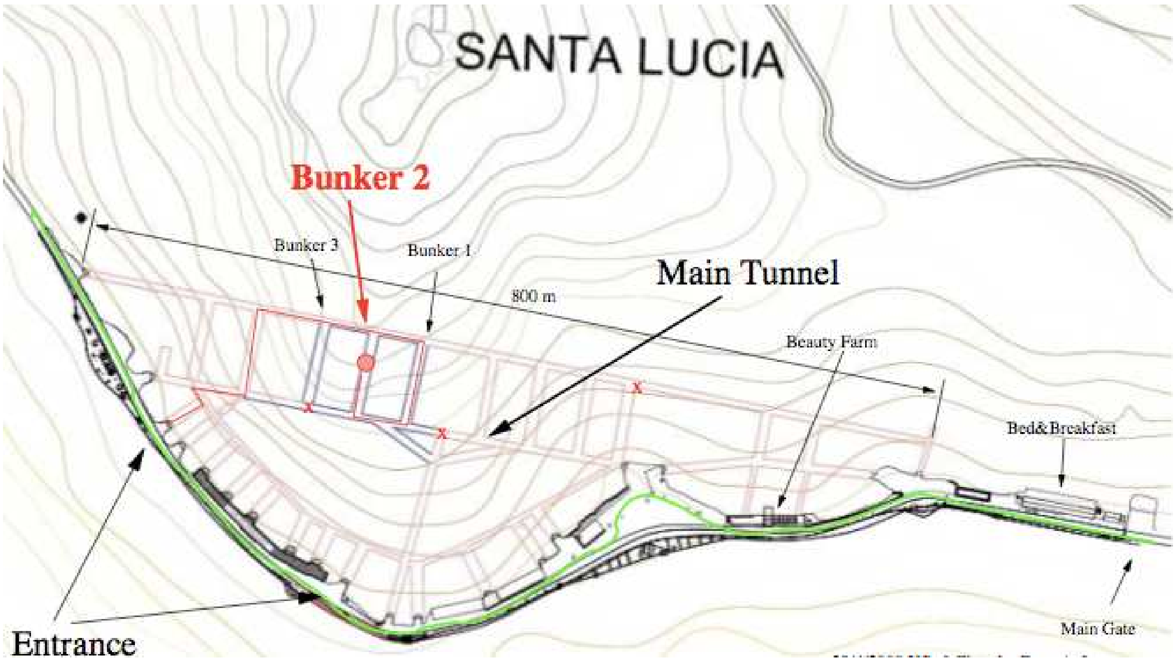

Figure C.1: *The map of the Monte Soratte bunker. The car lane is indicated in green while in red there is the passage into the bunker to reach the second main hall.*

C.3 The Felsenkeller Laboratory

The underground laboratory ”Felsenkeller” (FK) is located in the Weisseritz-valley in Dresden. The site was until 1980 an old brewery from which it takes the name. The tunnels in the rock were used to store the ice and the beer. The site is made by eight tunnels. Over each tunnel there are more or less 47 m of rock which corresponds to 110 m.w.e. At this depth the cosmic muon flux is reduced by a factor 50 compared to that at the surface. The rock consists of hornblende monzonite (Hb-Mz) [66] containing 5% K, 50 ppm Th and 10 ppm U. This corresponds to activities of ^{40}K, ^{232}Th, ^{208}Tl and ^{214}Bi of 1300, 200, 72 and 120 Bq/kg, respectively.

The total shielding of the area used as laboratory (called Room 2) consists from outside to inside of 10 mm new steel, 270 mm granulate of hard steel, 30 mm lead and 12 mm old steel. The activity of ^{222}Rn in the cave amounts to 200 Bq/m^3. Heated air from outside (40 Bq/m^3) is continuously introduced to reduce this level inside the laboratory. About 10 cm of concrete is located between the steel box chamber (Room 2) and the floor of the cave. The temperature is kept constant (about 20 C) due to a layer of about 10 cm of porous polystyrene is used around the whole chamber. The polystyrene layer also thermalizes fast neutrons produced in the rock. A new active shield made by plastic scintillators is under development (R&D phase) in order to increase the cosmic ray suppression. It is not clear yet its effect on the dead time.

The control room is placed in the same tunnel as Room 2.

C.4 Comparison

The background spectra acquired overground and underground at different places are compared. In addiction to the laboratories previously described we measured the natural background in Padua. The region below 3 MeV in the γ-spectrum is dominated by the γ-rays emitted by the air, the rocks, the setup materials around the detector and the contaminant in the detector itself. Between the line of the ^{208}Tl and 4 MeV there is the contribution due to the summing effect from the above mentioned radioactivity. Above 4 MeV the γ-ray spectrum overground is dominated by the cosmic ray radiation and particularly by the muons (sec. 2.1). In this region, from 4 MeV up to 8 MeV, there is also the contribution due to the (n,γ) reactions, but they represent a negligible contribution in overground measurements.

Fig. C.2 shows acquired spectra overground in three different places: Padua, outside the Monte Soratte tunnels and Dresden. The spectrum shape at γ-energies above 4 MeV is always the same. The small difference in the three spectra are due mainly from the difference in altitude. The entrance of the Monte Soratte tunnels is placed at 500 m above the sea level. The γ-ray background on the Monte Soratte is 30% more intense than in Padua. The shapes of the spectra in Dresden and in Padua are quite the same. The background reduction is clear visible underground and two bumps in the energy range from 4 MeV to 8 MeV appear in the γ-ray spectrum. These two broad peaks are produced by the (n,γ) reactions and by the α-particles produced inside the detector. In Fig. C.3 the spectra acquired underground are shown, normalized by the time. The two above mentioned peaks are not produced by the cosmic rays and, as a consequence, their contribution is quite the same in all of the sites examined. The region above 4 MeV has been divided in this analysis into two parts: between 4 and 8 MeV and from 8 MeV to 16 MeV in order separate the effect of neutrons and α particles from the contribution from the cosmic rays (i.e. ^{212}Po emits a 8.78 MeV α-particle. The 0.6 quenching factor reduces the α energy to the region from 4 to 5 MeV where the bump is placed). In the energy region between 4 and 8 MeV the underground reduction is about two orders of magnitude for all sites. The slight differences (see tab. C.1), more evident in the broad peak at 6.5 MeV, is probably due to a different muon and neutrons flux. The effect of the cosmic ray contribution suppression can be clearly seen in the region from 8 MeV up to 16 MeV. In LNGS this suppression amounts to five orders of magnitude, whereas in Monte Soratte to 2 orders of magnitude only because of the different depth. For the same reason from the 300 m.w.e. depth of Monte Soratte to the 110 m.w.e. depth of Felsenkeller there is an increase by a factor 4 in the γ-ray spectrum.

Summarizing the counts rate in the region from 8 to 16 MeV is reduced by 5 orders of magnitude in LNGS, by 2 orders of magnitude inside Monte Soratte and by a factor 50 in the Flsenkeller (FK) as compared to overground.

The γ-spectrum below 4 MeV is dominated by the γ-rays produced in the sorrounding

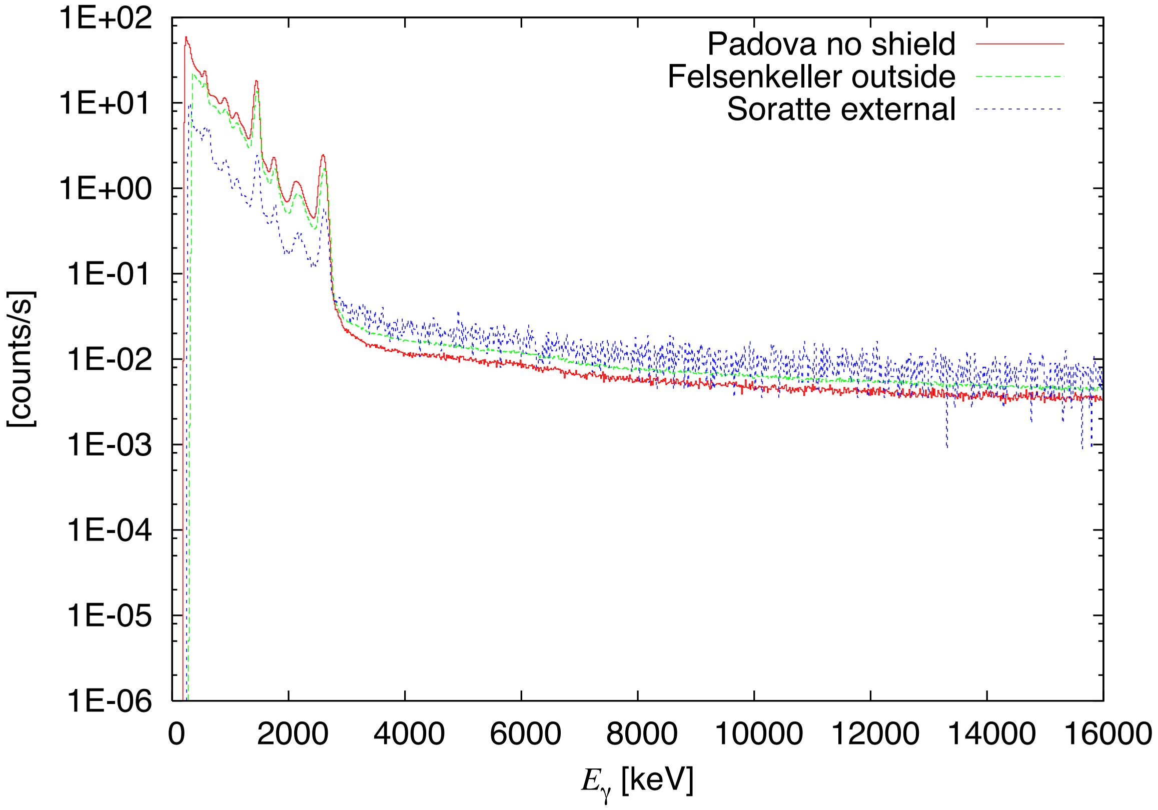

Figure C.2: *Three γ-ray spectra are shown in the picture. They have been acquired in Padua, on the Monte Soratte and in Dresden.*

Site	4-8 MeV	8-16 MeV
Padova	2.037±0.008	2.057±0.005
Soratte ext	4.03±0.13	3.97±0.06
Soratte int	0.045±0.009	$(1.52\pm0.05)\cdot10^{-2}$
Felsenkeller ext	2.631±0.004	2.550±0.004
FK controll room	0.072±0.001	0.053±0.001
FK steel room	0.089±0.001	0.059±0.001
LNGS	$(2.0\pm0.02)\cdot10^{-2}$	$(1.5\pm0.5)\cdot10^{-5}$

Table C.1: *Comparison of the background in different sites. The value are reported in counts per sec in the region of interest. The uncertainty reported in the table, are statistical.*

materials and inside the detector itself. To study this region of the γ-spectrum a quasi-background free detector has to be used together with a proper shielding (as shown in sec. A). We are actually using a germanium detector for this purposes and the data are still under analysis.

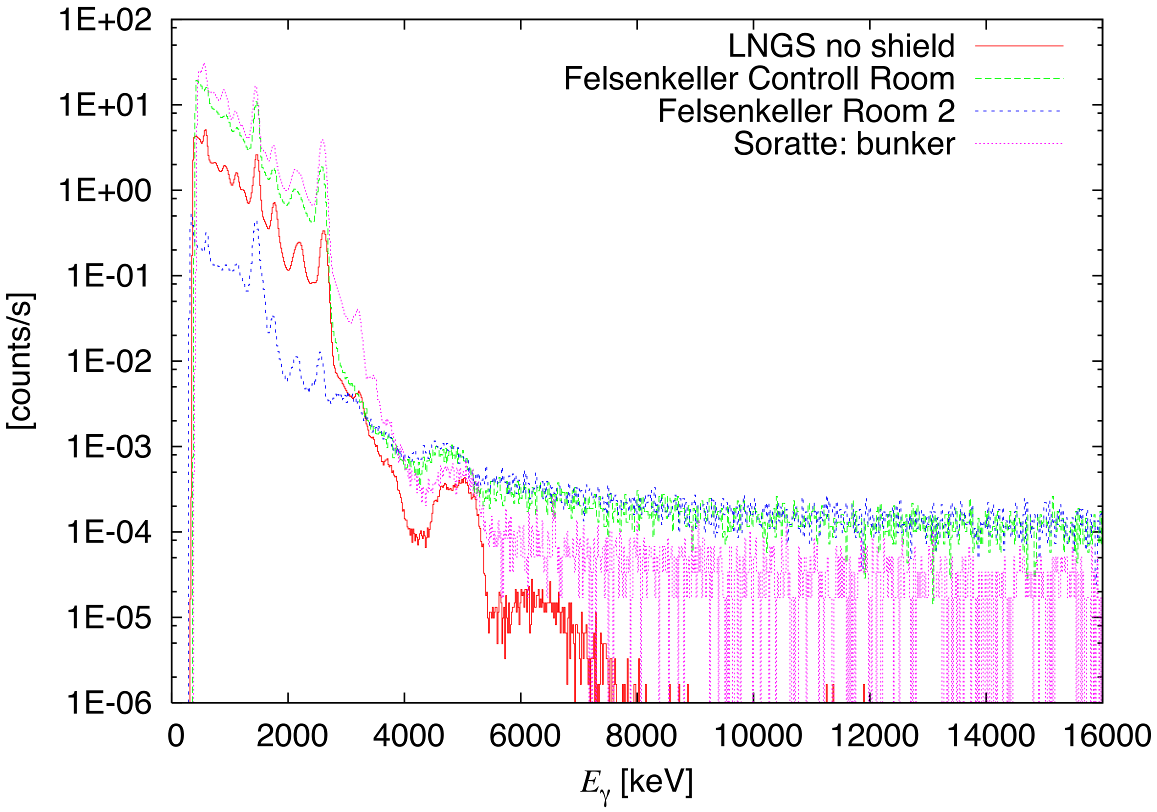

Figure C.3: *Four γ-ray spectra are shown in the picture. They are the underground spectra acquired at LNGS, in the tunnel of the Monte Soratte and in the Room 2 and the control room of the Felsenkeller laboratory in Dresden.*

Bibliography

[1] A. Formicola *et al.*, Physics Letters B **591**, 61 (2004).

[2] G. Imbriani *et al.*, Eur. Phys. J. A **25**, 455 (2005).

[3] D. Bemmerer *et al.*, Nuclear Physics A **779**, 297 (2006).

[4] A. Lemut *et al.*, Physics Letters B **634**, 483 (2006).

[5] M. Marta *et al.*, Physical Review C (Nuclear Physics) **78**, 022802 (2008).

[6] C. E. Rolfs and W. S. Rodney, *Cauldrons in the Cosmos* (The University of Chicago Press, 1988).

[7] C. Angulo *et al.*, Nuclear Physics A **656**, 3 (1999).

[8] R. F. Christy and I. Duck, Nuclear Physics **24**, 89 (1961).

[9] C. Rolfs, Nuclear Physics A **217**, 29 (1973).

[10] J. Jose and M. Hernanz, The Astrophysical Journal **494**, 680 (1998).

[11] J. Jose, E. Garcia-Berro, M. Hernanz, and P. Gil-Pons, The Astrophysical Journal Letters **662**, L103 (2007).

[12] C. Iliadis, A. Champagne, J. Jose, S. Starrfield, and P. Tupper, The Astrophysical Journal Supplement Series **142**, 105 (2002).

[13] D. Hebbard, Nuclear Physics **15**, 289 (1960).

[14] C. Rolfs and W. S. Rodney, Nuclear Physics A **235**, 450 (1974).

[15] A. M. Mukhamedzhanov *et al.*, Physical Review C (Nuclear Physics) **78**, 015804 (2008).

[16] F. C. Barker, Physical Review C (Nuclear Physics) **78**, 044612 (2008).

[17] T. K. Gaisser, *Cosmic Rays and Particle Physic* (Cambridge University Press, 1990).

[18] G. Fiorentini, R. W. Kavanagh, and C. Rolfs, Z. Phys A **350**, 289 (1994).

[19] A. Caciolli *et al.*, Eur. Phys. J. A **39**, 179 (2009).

[20] A. Formicola *et al.*, Nuclear Instruments and Methods in Physics Research Section A: Accelerators, Spectrometers, Detectors and Associated Equipment **507**, 609 (2003).

[21] T. Freye, H. Lorenz-Wirzba, B. Cleff, H. P. Trautvetter, and C. Rolfs, Z. Phys A **281**, 211 (1977).

[22] G. Audi and A. H. Wapstra, Nuclear Physics A **595**, 409 (1995).

[23] SRIM, www.srim.org 2008.

[24] C. Casella *et al.*, Nuclear Instruments and Methods in Physics Research Section A: Accelerators, Spectrometers, Detectors and Associated Equipment **489**, 160 (2002).

[25] T. B. Coplen *et al.*, Pure Appl. Chem. **74**, 1987 (2002).

[26] A. Mariotti, Nature **303**, 685 (1983).

[27] G. Junk and H. J. Svec, Geochimica et Cosmochimica Acta **14**, 234 (1958).

[28] S. Agostinelli *et al.*, Nuclear Instruments and Methods in Physics Research Section A: Accelerators, Spectrometers, Detectors and Associated Equipment **506**, 250 (2003).

[29] A. Best, Master's thesis, Ruhr-Universität Bochum (2007).

[30] J. Apostolakis *et al.*, Journal of Physics: Conference Series **119**, 032004 (9pp) (2008).

[31] C. Arpesella *et al.*, Nuclear Instruments and Methods in Physics Research Section A: Accelerators, Spectrometers, Detectors and Associated Equipment **360**, 607 (1995).

[32] D. R. Tilley, H. R. Weller, and C. M. Cheves, Nuclear Physics A **564**, 1 (1993).

[33] D. Bemmerer *et al.*, Journal of Physics G: Nuclear and Particle Physics **36**, 045202 (10pp) (2009).

[34] D. Bemmerer *et al.*, Eur. Phys. J. A **24**, 313 (2005).

[35] F. E. Cecil *et al.*, Nuclear Physics A **539**, 75 (1992).

[36] P. J. Grant, F. C. Flack, J. G. Rutherglen, and W. M. Deuchars, Proceedings of the Physical Society. Section A **67**, 751 (1954).

[37] F. Ajzenberg and T. Lauritsen, Rev. Mod. Phys. **24**, 321 (1952).

[38] G. Gilmore and J. Hemingway, *Practical Gamma-ray spectrometry* (John Wiley and Sons, New York, 1995).

[39] F. Confortola, *Tesi di Laurea in Fisica* (Università degli Studi di Genova, 2003).

[40] ENSDF, http://www.nndc.bnl.gov/ensdf/ 2008.

[41] V. Rigato *et al.*, Surface and Coating Technology **142-144**, 943 (2001).

[42] A. A. Kraus, A. P. French, W. A. Fowler, and C. C. Lauritsen, Phys. Rev. **89**, 299 (1953).

[43] A. Bergmaier, G. Dollinger, and C. M. Frey, Nuclear Instruments and Methods in Physics Research Section B: Beam Interactions with Materials and Atoms **136-138**, 638 (1998), Ion Beam Analysis.

[44] A. Bergmaier, G. Dollinger, and C. M. Frey, Nuclear Instruments and Methods in Physics Research Section B: Beam Interactions with Materials and Atoms **99**, 488 (1995), Application of Accelerators in Research and Industry '94.

[45] F. Ajzenberg-Selove, Nuclear Physics A **506**, 1 (1990).

[46] R. D. Evans, *The Atomic Nucleus* (McGraw-Hill: New York, 1955).

[47] D. Bemmerer *et al.*, Phys. Rev. Lett. **97**, 122502 (2006).

[48] G. Gyürky *et al.*, Phys. Rev. C **75**, 035805 (2007).

[49] F. Confortola *et al.*, Phys. Rev. C **75**, 065803 (2007).

[50] H. Costantini *et al.*, Nuclear Physics A **814**, 144 (2008).

[51] J. N. Bahcall, A. M. Serenelli, and S. Basu, The Astrophysical Journal Letters **621**, L85 (2005).

[52] W. C. Haxton and A. M. Serenelli, The Astrophysical Journal **687**, 678 (2008).

[53] P. D. Serpico *et al.*, Journal of Cosmology and Astroparticle Physics **2004**, 010 (2004).

[54] C. Rolfs and R. E. Azuma, Nuclear Physics A **227**, 291 (1974).

[55] T. Spillane *et al.*, Phys. Rev. Lett. **98**, 122501 (2007).

[56] C. Iliadis, *Nuclear Physics of Stars* (New York: Wiley-VCH, 2007).

[57] D. C. Powell *et al.*, Nuclear Physics A **660**, 349 (1999).

[58] M. Marta *et al.*, Nuclear Instruments and Methods in Physics Research Section A: Accelerators, Spectrometers, Detectors and Associated Equipment **569**, 727 (2006).

[59] C. Arpesella, Applied Radiation and Isotopes **47**, 991 (1996), Proceedings of the International Committee for Radionuclide Metrology Conference on Low-level Measurement Techniques.

[60] G. Hausser, Nuclear Instruments and Methods in Physics Research Section B: Beam Interactions with Materials and Atoms **83**, 223 (1993).

[61] W. Haxton, K. Philpott, R. Holtz, P. Long, and J. Wilkerson, Nuclear Instruments and Methods in Physics Research Section A: Accelerators, Spectrometers, Detectors and Associated Equipment **570**, 414 (2007).

[62] F. Strieder, Journal of Physics G: Nuclear and Particle Physics **35**, 014009 (7pp) (2008).

[63] C. Bordeanu, C. Rolfs, R. Margineanu, F. Negoita, and C. Simion, Journal of Physics G: Nuclear and Particle Physics **35**, 014011 (6pp) (2008).

[64] A. Gurbich and S. Molodtsov, Nuclear Instruments and Methods in Physics Research Section B: Beam Interactions with Materials and Atoms **266**, 1206 (2008), Ion Beam Analysis - Proceedings of the Eighteenth International Conference on Ion Beam Analysis, Eighteenth International Conference on Ion Beam Analysis.

[65] I. C. Vickridge, W. J. Trompetter, and G. E. Coote, Nuclear Instruments and Methods in Physics Research Section B: Beam Interactions with Materials and Atoms **108**, 367 (1996).

[66] S. Niese, M. Koehler, and B. Gleisberg, Journal of Radioanalytical and Nuclear Chemistry **233**, 167 (1998).

List of Figures

1.1 Hertzsprung-Russel diagram. Most of the stars, including the Sun, are aligned along the main sequence. $L_\odot$ is the luminosity of the Sun. 2
1.2 The proton-proton chain for hydrogen burning in the Sun. 3
1.3 The first and second CNO cycles. 3
1.4 Schematic representation of the combined nuclear and Coulomb potentials. . 6
1.5 The Gamow peak for the ^{15}N(p,γ)^{16}O reaction at three different temperatures. The Maxwell-Boltzmann distribution (1.8) is shown in red, the cross section (1.18) in green and their product in the three colors reported in figure. The y axis is linear, in arbitrary units. The curves are scaled to be clearly visible in the picture. 9
1.6 Scheme of a generic direct capture reaction A(x,γ)B. 10
1.7 The state of art of the measured S-factor in literature. 14

2.1 The LUNA2 400 kV accelerator with the tank open for maintenance. Inside the tank, the metallic rings, keeping the ion source free from electric fields, are visible. 18
2.2 The radio frequency ion source of the LUNA2 400 kV accelerator. The characteristic pink light of the hydrogen plasma is visible. 18
2.3 The windowless gas target pumping system. The details for the collimator are given in the text. 20
2.4 Calorimeter for the measurement of the beam intensity. The heating resistors are marked as thick red lines. The white circles represent thermoresistors for measuring the temperature. 21
2.5 The scheme of the solid target channel from the second dipole magnet. The cold trap and the BGO detector are also shown. 23
2.6 The solid channel during the alignment. On the left there is the connection with the second dipole magnet. In the picture it is possible to see also the BGO placed around the target. 23
2.7 BGO detector in the configuration used for the ^{15}N(p,γ)^{16}O experiment with gas target setup. The photomultipliers positions are indicated in two different lateral views. The BGO crystal is shown in green, the target area in blue and the photomultipliers in orange. All dimensions are given in mm. 24

2.8 BGO detector in the configuration used for the ^{15}N(p,γ)^{16}O experiment with solid target setup. 25
2.9 Schematic layout of the LUNA-FAIR DAQ chain. Shown are the relevant channels of the 16-fold amplifier, constant fraction discriminator (CFD), coincidence and logical OR units. 26
2.10 Schematic layout of the Ortec MAESTRO DAQ chain. The amplification for each channel is adjusted by fine-tuning the PMT high voltage with the procedure described in the text. 27

3.1 Isotopic abundances of ^{15}N, plotted are the permille deviations from the standard. The figure has been adapted from [25]. 30
3.2 The setup used to measure the beam heating effect. 32
3.3 Setup for the beam-induced background study. The two main sources of beam induced background, i.e. at the surfaces of the final collimator and of the calorimeter are marked in orange. 33
3.4 BGO detector, together with all the passive materials modeled for the present description. 34
3.5 Experimental and simulated spectra for a position near the center of the BGO crystal. The target chamber was not included in experimental spectrum. . . . 35
3.6 Experimental and simulated spectra for a position near the final collimator. The position of the ^{22}Na source was adjusted by 6 mm in the simulation to fit the peak height ratios. The laboratory background has been subtracted from the experimental spectrum. The relative difference between experimental and simulated spectrum is given next to each peak. 36
3.7 Detection efficiency for detecting ^{14}N(p,γ)^{15}O γ-rays in the 6.5-8.0 MeV region of interest, for the run at E_{beam} = 100 keV. Black thin (red line), GEANT3 simulation (present GEANT4 simulation, in total 30000 emitted γ-rays. 37
3.8 Level scheme of the ^{16}O nucleus. Many levels are in principle accessible for E1 and E2 capture. The proton separation energy is shown by a dotted red line. 38
3.9 Simulation of the effect of a possible cascade transition on the detection efficiency. 39
3.10 Event caused by a 12 MeV γ-ray inside the BGO detector. The passive materials shown in Fig. 3.4 have been considered in the simulation, but were omitted from this figure for clarity. The final collimator and the calorimeter are shown. 40
3.11 The γ-ray spectrum, E_{beam} = 220 keV. Solid red (dotted blu) line: the nitrogen gas in the target (helium gas, rescaled to match the nitrogen spectrum in the 14.4-18.0 MeV region). Dashed green line, laboratory background, rescaled for equal live-time. This figure has been taken from Bemmerer, Caciolli *et al.*[33]. 41
3.12 γ-ray spectrum, E_p = 250 keV. The peaks used for the calibration (black) and the peak at 16 MeV (red) are pointed by arrows. 42

3.13 γ-ray spectrum, E_p = 150 keV. 43
3.14 γ-ray spectrum, E_p = 250 keV (black line) and laboratory background normalized to the lifetime (red line). The two ROIs are indicated. 44
3.15 γ-ray spectrum, E_p = 100 keV.The sum of all spectra at this energy is shown in black and the contribution from only one spectrum is given in red. 45
3.16 γ-ray spectrum, E_p = 180 keV, the spectrum with helium gas has been scaled up to match the nitrogen spectrum in the 14.4 - 18 MeV region. 46
3.17 γ-ray spectrum, E_p = 200 keV, 1 mbar nitrogen in the gas target, germanium detector. 47
3.18 γ-ray spectrum, E_p = 200 keV, germanium detector, detail of the region near 7.1 MeV. 48
3.19 The γ-ray spectrum, E_{beam} = 220 keV. Red solid (dot dashed) line: experimental, nitrogen gas (simulated, assuming only the ^{15}(p,γ)^{16}O reaction). Blue dashed (dotted) line: experimental, helium gas, rescaled as in Fig. 3.11 (simulated with Sim 1B, assuming only the ^{11}B(p,γ)^{12}C reaction.This figure has been taken from Bemmerer, Caciolli *et al.*[33]. 49
3.20 $\beta(E_{beam})$: ratio of counts in the regions ROI$_1$ (9.7-13.5 MeV) and ROI$_2$ (14.4-18.0 MeV). Plotted are the experimental $\beta(E_{beam})$ data points that were also used for the final data analysis. The curves are from GEANT4 simulations. See text for details. 50
3.21 Astrophysical S-factor for the ^{15}N(p,γ)^{16}O reaction as as function of the center of mass energy. The LUNA gas target are presented (circles) with data from Hebbard [13] (triangle) and from Rolfs and Rodney [14] (black diamonds). The curve represents the R-matrix fit from the ANC data [15] with the quoted errors (dashed curves). The NACRE extrapolation is also reported. 54

4.1 The six raw spectra from all crystals are reported. The not perfect gain matching is evident in channel 3 and channel 5 spectra. The software sum procedure neglects totally this problem. The spectrum has been acquired on the target LNL2 at an energy of 385 keV in the laboratory system. 59
4.2 A not calibrated single crystal spectrum acquired at E_{beam} = 380 keV. 59
4.3 An example of the three fits to the peaks shown in Fig. 4.2 and used in the calibration. The red curve represent the fit. 60
4.4 Multiplicity spectrum. The multiplicity represents the numbers of crystals where the γ-ray energy has been lost. 61
4.5 Level scheme of ^{12}C from ENSDF database [40], the levels and transitions important for the E_{beam} = 163 keV resonance in ^{11}B(p,γ)^{12}C (E_X = 16106 keV in ^{12}C) are highlighted. The main γ-rays found in the spectrum are shown as arrows. The two γ-rays used for the efficiency calibration is shown in red. . . 62
4.6 Software sum spectrum acquired at E_{beam} = 120 keV. 63
4.7 Software sum spectrum acquired at E_{beam} = 380 keV. In the figure the main peaks are identified. 63

4.8 Region of a DC plasma. 65
4.9 Paschen curve that indicates the electrodes voltage necessary to start the plasma as a function of Pd (P = pressure in the sputtering chamber, d = distance between the electrodes). 66
4.10 The yield curve of eq. (4.2) plotted for the ^{15}N(p,$\alpha\gamma$)^{12}C resonance at E_p = 429.5 keV. The target thickness, ΔE, is 15 keV. The straggling effect is not considered. For the stopping power ϵ_r eq. (4.6) has been used. 67
4.11 The measured yield acquired on the LNL2 target with the BGO detector at LUNA. The scan is related to the resonance at E_p = 278 keV of the ^{14}N(p,γ)^{15}O reaction. The peak in the plateau at the E_{CM} = 292 keV is not well understood yet. It is probably due to the dynamic flux of the nitrogen gas in the sputtering chamber. Variations in this flux can affect highly the amount of ^{14}N in the targets. 68
4.12 The scans acquired over a week on the target Ka2. The y-axis scale is the same in all graphs in order to underline the increasing of the plateau. 69
4.13 Three scans acquired over a week on the target LNL1. 69
4.14 The tandetron accelerator. 70
4.15 The chamber with the target at 55° in respect to the beam direction. The 60% Germanium detector is placed in the position used in the measurements. . . . 71
4.16 The target chamber already used in the measurements at LUNA with the BGO detector. The 60% Germanium detector was placed at 0° in respect to the beam direction. 72
4.17 An example of the "virgin" area (left) and "beamspot" area (right) measured position for the target Ka2. The beam position is defined by the black circle. This cirlce has been superimposed on the target picture by a graphic software. 72
4.18 Resonance scans on "virgin" (red points) and "beamspot" (green points) areas on the target Ka4. The profiles have been fitted with a arctan function in order to show the profile behavior. This function has not been used in the analysis. 73
4.19 Resonance scans on "virgin" (red points) and "beamspot" (green points) areas on the target LNL2. The profiles have been fitted with a arctan function in order to show the profile behavior. This function has not been used in the analysis. 73
4.20 The stopping power curve for TiN from [23]. 74
4.21 The value of $\frac{\int\sigma(\Delta E=100\%)-\int\sigma(\Delta E=70\%)}{\int\sigma(\Delta E=100\%)}$ is reported in blue. For comparison the ^{15}N(p,γ)^{16}O S-factor from [15] is shown in the black curve. 75
4.22 Geometric scheme for the ERD experiment. 76
4.23 Schematic view of the detector layout [43]. 77
4.24 $\Delta E - E_{tot}$ spectrum of recoil scattered from the enriched target produced in Legnaro. Most of the counts in the spectrum are from the scattered ^{127}I beam. This noise is very well separated from the recoil counts. The two regions of titanium and nitrogen are visually selected by a circle. 78

4.25 The resonance scan on the "virgin" area on target LNL7 is reported on the left. On right there is the deduced profile plot from the plotted resonance scan. The plot on the right is calculated using eq. 4.10 and the technique described above. 79

4.26 The sum spectrum for the ^{60}Co source. The spectrum is obtained by the software sum. The scale of the x-axis has been chosen to underline the summing peak at 2.5 MeV. 81

4.27 The single spectrum for the ^{60}Co source. The two peaks are evident. The spectrum is the relative to the crystal 1 of the BGO detector. 81

4.28 The sum spectrum for the ^{22}Na source. The three peaks at 1275, 1786 and 2550 keV are evident. 82

4.29 Pos 1 for the source during the efficiency measurements. The position scheme is shown in the left panel. The backing is represented in black, the ring in blue the source in red and the plastic cap in light brown. The photo of the source is in the right part of the picture. 83

4.30 Pos 2 for the source during the efficiency measurements. The position scheme is shown in the left panel. The backing is represented in black, the ring in blue the source in red and the plastic cap in light brown. The photo of the source is in the right part of the picture. 83

4.31 Pos 3 for the source during the efficiency measurements. The position scheme is shown in the left panel. The backing is represented in black, the ring in blue the source in red and the plastic cap in light brown. The photo of the source is in the right part of the picture.The length of the shift of the source is underlined in the picture. 84

4.32 The measured efficiency for the ^{60}Co source is reported for the three different positions reported in the legend (see text) and for two different values of the trigger threshold. 85

4.33 Level scheme of ^{12}C from ENSDF [40], the levels and transitions important for the E_{beam} = 163 keV resonance in ^{11}B(p,γ)^{12}C (E_X = 16106 keV in ^{12}C) are highlighted. The main γ-rays found in the spectrum are shown as arrows. The couple of γ-rays used for the efficiency calibration validation is shown in red. 85

4.34 Sum spectrum. Comparison of experimental data and two different GEANT4 simulations for the E_{beam} = 163 keV resonance in the ^{11}B(p,γ)^{12}C reaction. . . 86

4.35 Singles spectra. Comparison of experimental data and two different GEANT4 simulations for the E_{beam} = 163 keV resonance in the ^{11}B(p,γ)^{12}C reaction. The region of interest for the ratio determination in table 4.4 are shown as dashed lines. 87

4.36 Software sum spectrum acquired at E_{beam} = 380 keV. In the figure ROI$_1$ and ROI$_2$ are shown. 88

4.37 Astrophysical S-factor for the ^{15}N(p,γ)^{16}O reaction as as function of the center of mass energy. The LUNA solid (black) and gas (green) target data are presented with data from Hebbard [13] (blue) and from Rolfs and Rodney [14] (purple). The curve represents the R-matrix fit from the ANC data [15] with the quoted errors (dashed curves). The NACRE extrapolation is also reported (pink). 92

A.1 Schematic view of the experimental setup C (complete shielding). 99

A.2 Photo taken during the construction of the shield. The lower half of the lead shield is already complete, as well as the copper shield for the detector and the copper plate above the target chamber. The back plate and connectors of the beam calorimeter are visible in the upper right corner. The copper tube for the beam inlet is seen in the upper left corner. The upper half of the lead shield was not yet installed when the photo was taken. 100

A.3 Laboratory γ-ray background spectra for setups A (black dashed line), B (blue dotted line) and C (red full line). See table A.1 for the counting rate of the selected lines and table A.2 for the assignment of the lines evident in spectrum C. 101

A.4 Laboratory γ-ray background spectra for setups C (red full line, same as in Fig. A.3) and inert sample counted in setup LLL (black dashed line). See table A.1 for the counting rate of the selected lines and table A.2 for the assignment of the lines evident in spectrum C. 102

A.5 Comparison of offline and in-beam γ-spectra: setup B, offline (blue dashed line) and with α-beam (black dotted line). Setup C, offline (red full line) and with α-beam (black dot-dashed line). 104

A.6 Cross-section $\sigma_{\mathrm{S/N}=1}(E_\gamma)$ defined by eq. (A.1), for setups B (blue dashed line) and C (red full line). The γ-ray energies of interest for the nuclear reactions listed in tableA.3 are indicated by gray bars. 105

B.1 Detail of the target holder. On the left, the LUNA target is placed. 110

B.2 The silicon detector spectra are reported. In red the measurement for the ″virgin″ area spot and in green for the ″beamspot″ area. The analyzed peak for ^{14}N(d,α_0)^{12}C and ^{15}N(d,α_0)^{13}C are underlined in the peak together with the peak due to the elastic scattering of deuterium on the tantalum backing. . 111

B.3 Schematic view of the SNMS process. The blue ions sputter the ion from the sample and the sample profile will be constructed. 113

B.4 The obtained profiles for the target Ka5 with the SNMS technique. In the left side there is the profile for the ″virgin″ area and on the right picture there is the ″beamspot″ measurements. The long nitrogen tail in the tantalum backing is evident. 114

C.1 The map of the Monte Soratte bunker. The car lane is indicated in green while in red there is the passage into the bunker to reach the second main hall. . . . 116
C.2 Three γ-ray spectra are shown in the picture. They have been acquired in Padua, on the Monte Soratte and in Dresden. 118
C.3 Four γ-ray spectra are shown in the picture. They are the underground spectra acquired at LNGS, in the tunnel of the Monte Soratte and in the Room 2 and the control room of the Felsenkeller laboratory in Dresden. 119

List of Tables

2.1 Cosmic rays suppression at LNGS. 17

2.2 Statistical and systematic error of the energy calibration. 19

2.3 Collimator dimension in millimeters. 21

2.4 Pump system characteristics. The value in the last three columns are related to a pressure p_{T0} = 1 mbar. 21

3.1 Isotopic ratio of the Gran Sasso nitrogen samples. 31

3.2 Spectrum integration and background subtraction. The raw counts in the ROI$_1$ and in the background monitoring region (ROI$_2$) are given. For the ratio β, the experimental data are from runs with helium gas in the target. The simulation 1 and 2 and the adopted uncertainty are explained in the text. The boron background in the ROI$_1$ (column 8) is obtained by multiplying columns 3 and 7. The net counts in the peak (column 9) are obtained by subtracting column 8 from column 2. 51

3.3 Systematic uncertainties and their effect on the S-factor value. 54

3.4 Effective center of mass interaction energy E_{eff}, S-factor and relative uncertainties. The systematic uncertainty due to the boron background subtraction has been derived in table 3.2 and is repeated here (column 5). The boron uncertainty is already included in the total systematic uncertainty given above (column 4). 55

4.1 The two sets of targets. For each target the integrated charge collected during the LUNA measurements is given. For target Ka3 the total integrated charge was 116 C, but we analyzed runs only until 20 C. Some targets from the LNL set have been used only for the target offline analysis. 64

4.2 The stoichiometry ratio obtained for each target with the ERD technique. . . . 77

4.3 The radioactive sources used in the efficiency measurements. The activity value is given at two sigma uncertainty. 81

4.4 Comparison of experimental and simulated ratios of counting rates for the sum of the single histograms. The uncertainty is the statistical uncertainty of the GEANT4 simulation. 88

4.5 Effective center of mass interaction energy E_{eff}, S-factor and relative statistical uncertainties. Systematic uncertainty is 11% for all points. 91

4.6 Systematic uncertainties and their effect on the solid target S-factor value. . . 92

A.1 Counting rate in counts/hour for selected γ-lines, in setups A-C at LUNA. For comparison, the corresponding numbers are also given for setup LLL at the LNGS low level laboratory. Upper limits, where applicable, are given for 2σ confidence level. 101
A.2 List of γ-lines evident at 2σ level or better in the laboratory background of setup C (fig. A.3). 103
A.3 Reactions of astrophysical interest discussed in the text. The relevant astrophysical scenario, typical temperature T_9 and corresponding Gamow energy [56] E_{Gamow} are also given. The expected cross section at E_{Gamow} has been estimated. The relevant γ-ray energy is also shown. For the case od setup C, the cross section $\sigma_{S=N}(E_\gamma)$ has been calculated following eq. (A.1). 106

C.1 Comparison of the background in different sites. The value are reported in counts per sec in the region of interest. The uncertainty reported in the table, are statistical. 119

Ringraziamenti

Voglio ringraziare primo fra tutti Carlo che mi ha fatto conoscere il progetto LUNA e ha seguito tutto il lavoro di questi tre anni insegnandomi cosa significa essere un ricercatore, prodigo di consigli, aneddoti storici e argute e sofisticate battute. Grazie anche al Prof. Masiero per aver sempre ricordato che la ricerca va vissuta con passione. Del gruppo di Padova non posso non ringraziare Roberto, per la sua pazienza ed i suoi preziosi consigli sia nella fisica che nell'informatica e per aver corretto fino all'ultimo questa tesi, e Carlos perché inizio a temere che sappia tutto.

Ringrazio tutti i membri della collaborazione LUNA che si sono sempre dimostrati disponibili nel rispondere alle mie domande o all'introdurmi ai segreti dell'esperimento. Un grazie particolare a Matthias, maestro dell'acceleratore e ad Alba unica ad accendere la sorgente schioccando le dita.

Non vedo l'ora di ringraziare di persona le *Angels* di Milano, Alessandra, Chiara e Valentina, che mi hanno sempre fatto sempre sentire come a casa nelle mie trasferte milanesi e con cui ho diviso gran parte delle misure riportate in questo lavoro di tesi.

Un grazie infinito a Daniel che mi ha accolto a Dresda e che ha seguito tutto questo lavoro di tesi che si poggia molto sui suoi consigli e suggerimenti.

Per ultimo ma non ultimo voglio salutare Michele mio compagno di dottorato in LUNA e famoso scacciatore di api, insieme abbiamo condiviso discussioni, battute e risate per questi stupendi tre anni.

Voglio ringraziare anche tutti i dottorandi di Padova, in particolare Lucia, Carlo, Marco, Angela e Luca per avermi aiutato a entrare nei meccanismi burocratici dell'Università (senza i vostri aiuti non penso sarei riuscito a finire) ed essere stati degli ottimi amici.

Infine un grazie alla mia famiglia, a Teresa e a tutti gli amici coinquilini e conoscenti di questi ultimi tre anni, saluterò al meglio e personalmente ognuno di voi.